JETP Letters, Vol. 72, No. 3, 2000, pp. 100–105. Translated from Pis'ma v Zhurnal Éksperimental'noĭ i Teoreticheskoĭ Fiziki, Vol. 72, No. 3, 2000, pp. 150–156.

Experimental Study of the Subthreshold Production of K^+-Mesons in Proton–Nucleus Collisions

A. V. Akindinov, Yu. T. Kiselev, A. N. Martem'yanov, V. I. Mikhaĭlichenko†, K. R. Mikhaĭlov, S. A. Pozdnyakov, Yu. V. Terekhov, M. M. Chumakov, and V. A. Sheĭnkman

Institute of Theoretical and Experimental Physics, Bol'shaya Cheremushkinskaya ul. 25, Moscow, 117218 Russia

Received June 23, 2000

Energy dependence of the differential cross sections for the production of K^+-mesons with a momentum of 1.28 GeV/c (c is the speed of light) by protons incident on Be, Al, Cu, and Ta nuclei was measured for energies both above and below the K^+-meson production threshold in pp collisions. Evidence is given for the dominance of the mechanism of direct production in the experiment. The characteristics of momentum distribution are determined for nucleons in the Be and Al nuclei up to 650 MeV/c. The data cannot be described in the model of nuclear spectral function. © *2000 MAIK "Nauka/Interperiodica".*

PACS numbers: 13.75.Cs; 21.30.-x

Subthreshold hadron production is among a few processes whose analysis provides information on the properties of nuclear matter at small internucleon distances, on the short-range part of nucleon–nucleon potential, and on the effect of a medium on the properties of produced particles. In contrast to the processes kinematically forbidden in the collisions of free nucleons, the interpretation of the subthreshold experiments is more unambiguous because the energy deficit in collisions leads to a considerable decrease in the number of possible hadron-production channels. On the assumption that the subthreshold K^+-mesons are produced on individual intranuclear nucleons, there are two such channels: the direct production mechanism (DPM) $pN \longrightarrow K^+YN$, and the two-step (cascade) production mechanism (TPM) $pN \longrightarrow NN\pi$, $\pi N \longrightarrow YK$ ($Y = \Lambda, \Sigma$). The high-momentum component can be studied only in the direct processes, because in the TPM the momenta of intranuclear nucleons are used twice and are on the order of the Fermi momentum. In the only work [1] on K^+-meson production in pA collisions, which was published by the beginning of our measurements, and in two more recent works [2, 3], the TPM dominated, as was shown by an analysis carried out in [4–7]. For this reason, our efforts were made to carry out experiments with a considerably smaller, than in [1–3], contribution from TPM relative to the DPM.

Choice of kinematic conditions of measurements. By the subthreshold particle production on nuclei is meant the processes forbidden under the same kinematic conditions as in the collisions with a free nucleon. This definition implies that the threshold energy depends both on the mass of the produced particle and on its momentum and exit angle. One usually studies either the dependence of the cross section for the formation of hadrons with fixed momentum and angle on the energy of an incident particle or the momentum dependence of the cross section for the hadron production at below-threshold energies. In the case of the $pA \longrightarrow K^+X$ reaction, the probability of the incident proton colliding with an intranuclear nucleon whose momentum $q_{\min}$ is sufficient for producing a kaon detectable in the DPM rapidly decreases with both decreasing proton energy and increasing K^+-meson momentum. The $q_{\min}$ value can be determined from the relationship

$$M_{YN}^2 = (E_0 + w - E_K)^2 - (\mathbf{p}_0 + \mathbf{q} - \mathbf{p}_K)^2 \geq (m_Y + m_N)^2, \quad (1)$$

where $(E_0, \mathbf{p}_0)$, $(E_K, \mathbf{p}_K)$, and $(w, \mathbf{q})$ are the 4-momentum components of the incident proton, the detected kaon, and the intranuclear nucleon, respectively; m_N and m_Y are the nucleon and hyperon masses, respectively; and M_{YN}^2 is the squared missing mass. At the reaction threshold, one has

$$M_{YN}^2 = M_{\Lambda N}^2 = (M_\Lambda + M_N)^2, \quad q_{\min} = |\mathbf{q}|. \quad (2)$$

The cross section for the subthreshold process rapidly decreases with increasing $q_{\min}$ but depends much more weakly on the momentum and the exit angle at a fixed $q_{\min}$ [8]. As a result, the DPM cross sections $E_{K^+}d\sigma/d\mathbf{p}$ measured in different experiments for the same $q_{\min}$ values are close to each other. This statement is likely also valid for the subthreshold pion-induced kaon production. With pions, the replacement of $(m_Y + m_N)^2$ by m_Λ^2 in Eq. (1) gives, at fixed $q_{\min}$, the momentum of an intermediate pion necessary for the subsequent production

† Deceased.

of a K^+-meson. It will be shown below that the probability of producing hard pions rapidly decreases with increasing scaling variable X_F^R:

$$E_\pi \frac{d\sigma}{d\mathbf{p}_\pi} \sim (1 - X_F^R)^n, \quad n > 3, \quad X_F^R = \frac{P^*}{P^*_{\max}}. \qquad (3)$$

Here, P^* and $P^*_{\max}$ are the momentum of the produced pion and its maximum value in the proton–nucleus system, respectively. Figure 1 shows the X_F^R variable against the minimum momentum of pions, which, when colliding with nucleons having a countermomentum of 250 MeV/c, can produce K^+-mesons that were detected in this study and in [1, 2]. On the abscissa, the $q_{\min}$ values determining the contribution of the DPM to the cross section are plotted. It is seen from the figure that, for close DPM cross sections and the same $q_{\min}$ values, intermediate pions with considerably larger X_F^R values are necessary for the production of K^+-mesons at the second stage of the cascade process under the chosen kinematic conditions. Considering Eq. (3), this means that our experiment will provide the minimum ratio of TPM to DPM cross sections.

Experiment. Invariant cross sections for the production of K^+-mesons with a momentum of (1.28 ± 0.014) GeV/c were measured at an angle of 10.5° to the internal proton beam from the ITEP accelerator. Thin Be, Al, Cu, and Ta foils were used as targets. The measurements were carried out over the proton energy range from 2.9 to 1.65 GeV. The proton beam energy was known with an accuracy of 5 MeV. The measurements were made on the same magnetic spectrometer as in [9] by the method described in [10]. K^+-mesons were reliably identified: the background contribution was less than 5% at energies above 1.7 GeV and increased up to 15% for the two lowest energies. The cross section values are given in Table 1, where errors are not indicated. The errors are less than 15% and do not include the errors of absolute data normalization, which are estimated at 20%. An example of the energy dependence of the cross sections for the production of K^+-mesons on the Be nucleus is shown in Fig. 2, where the right arrow indicates the threshold of the 1.28-GeV/c kaon production on a nucleon and the left arrow indicates the threshold of their production on the nucleus as whole. The last experimental point corresponds to the energy exceeding the absolute reaction threshold by 40 MeV.

Direct mechanism of kaon production. For the data analysis, we begin with their description on the assumption that the DPM dominates and the determination of the parameters of nucleon momentum distributions in the nuclei, after which the arguments in favor of this approach will be given. In what follows, the 4-momentum (w, $\mathbf{q}$) of the intranuclear nucleon is related to the 4-momentum (E_{A-1}, $\mathbf{p}_{A-1}$) of the residual

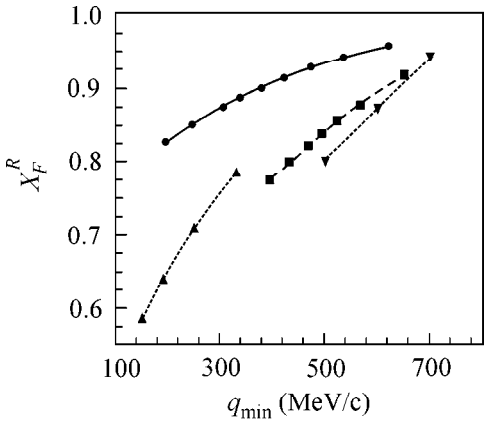

Fig. 1. Plots of X_F^R vs. $q_{\min}$ for the experiments on subthreshold K^+-meson production: ■ Be target, proton energies T_0 = 0.84–0.99 GeV, p_{K^+} = 0.25 GeV/c [1]; ▲ C target, T_0 = 1.5 GeV, p_{K^+} = 0.45–0.7 GeV/c [2]; ▼ C target, T_0 = 1.2 GeV, p_{K^+} = 0.5–0.7 GeV/c [2]; ● Be target, T_0 = 1.65–1.9 GeV, p_{K^+} = 1.28 GeV/c (this work).

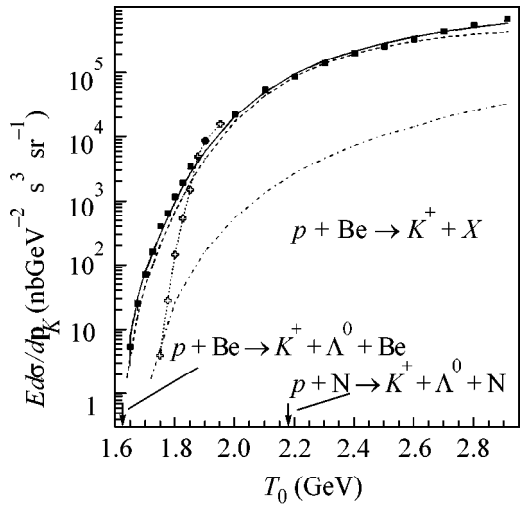

Fig. 2. Differential cross sections for K^+ production against the proton energy: ■ experimental data; the solid line is the description by Eq. (8); the dashed line is the phase-volume description; ◇ description by the spectral function; and the dash–dotted line is for the two-step mechanism.

nucleus, its mass M_{A-1}, and the mass M_A of the target nucleus by the relationships

$$w = M_A - E_{A-1}, \quad \mathbf{p}_{A-1} = -\mathbf{q}, \qquad (4)$$

and it is assumed that the residual nucleus is in the ground state

$$E_{A-1} = M_{A-1} + q^2/2M_{A-1}. \qquad (5)$$

Table 1. Invariant cross sections for K^+-meson production $E_{K^+}\frac{d\sigma}{dp_K}$ (nb GeV^{-2} sr^{-1} s^3) as functions of proton energy (GeV)

T_0	Be	Al	Cu	Ta	T_0	Be	Al	Cu	Ta
2.910	6.87×10^5	1.54×10^6	1.99×10^6		1.850	3.43×10^3	1.09×10^4	1.41×10^4	1.81×10^4
2.800	5.57×10^5	1.11×10^6	1.43×10^6		1.825	1.95×10^3	6.46×10^3	1.07×10^4	1.15×10^4
2.700	4.44×10^5		1.21×10^6		1.800	1.18×10^3	4.55×10^3	7.37×10^3	5.52×10^3
2.600	3.42×10^5	7.30×10^5	1.02×10^6	1.78×10^6	1.775	6.67×10^2	2.29×10^3	3.42×10^3	
2.500	2.61×10^5	6.50×10^5	8.12×10^5	1.31×10^6	1.750	4.17×10^2	1.37×10^3	1.98×10^3	1.85×10^3
2.400	2.07×10^5	4.45×10^5	6.71×10^5	1.02×10^6	1.725	1.67×10^2	5.92×10^2	9.04×10^2	$\pm3.7\times10^2$
2.300	1.44×10^5	3.43×10^5	4.78×10^5	6.50×10^5	1.700	71.7	2.47×10^2	3.40×10^2	
2.200	8.80×10^4	2.04×10^5	2.66×10^5	4.35×10^5	1.675	15.7	1.14×10^2	87.1	
2.100	5.50×10^4	1.15×10^5	1.49×10^5	2.50×10^5		±3.7	±28.5	±37	
2.000	2.23×10^4	5.57×10^4	7.66×10^4	1.15×10^5	1.650	5.50	42.0		
1.900	8.79×10^3	2.45×10^4	3.49×10^4	3.62×10^4		±2.5	±14.7		

It follows from Eqs. (4) and (5) that the energy of the off-mass nucleon is

$$\begin{aligned} w &= M_N - (M_{A-1} + M_N - M_A) - \frac{q^2}{2M_{A-1}} \\ &= M_N - \left(\epsilon + \frac{q^2}{2M_{A-1}}\right) = M_N - E_R, \end{aligned} \tag{6}$$

where E_R is the energy of nucleon separation from the nucleus and the minimum nucleon binding energy ϵ in the nuclei under study was taken to be 2 MeV. This choice of ϵ and the assumption that the residual nucleus is in the ground state are dictated by our wish to obtain the lower bound for the contribution of high momenta to the nucleon distribution $n(q)$. This distribution was chosen in the standard form of a superposition of two Gaussians with parameters σ_1, σ_2, and h:

$$\begin{aligned} n(q) &= \frac{1}{(2\pi)^{3/2}(1+h)}\left[\frac{1}{\sigma_1^3}\exp\left(\frac{-q^2}{2\sigma_1^2}\right) + \frac{h}{\sigma_2^3}\exp\left(\frac{-q^2}{2\sigma_2^2}\right)\right], \\ 4\pi\int n(q)q^2dq &= 1. \end{aligned} \tag{7}$$

Under the assumption that the cross sections for the kaon production on protons and neutrons are identical, the convolution model relates the cross section for the K^+-meson production on nuclei to that on a free nucleon as

$$\begin{aligned} &E_{K^+}\frac{d\sigma^{pA\to K^+X}(\mathbf{p}_0, \mathbf{p}_K)}{d\mathbf{p}_K} \\ &= N_1\int d\mathbf{q}\, n(\mathbf{q})\left[E_K\frac{d\sigma^{pp\to K^+X}(M_{YN}, \mathbf{p}_K)}{d\mathbf{p}_K}\right]. \end{aligned} \tag{8}$$

In Eq. (8), the expression in the square brackets is the cross section for the K^+-meson production in the proton collisions as a function of the missing mass M_{YN} (1). This cross section can be represented in the form

$$\begin{aligned} E_{K^+}\frac{d\sigma^{pp\to K^+X}(M_{YM}, \mathbf{p}_K)}{d\mathbf{p}_K} &= \frac{d^2\sigma^{pp\to K^+X}(M_{YN})}{dM_{YN}d\Omega_K} \\ &\times \frac{(E_0+m_N)p_K - p_0E_K\cos\theta_K}{p_K^2M_{YN}}, \end{aligned} \tag{9}$$

where θ_K is the kaon exit angle. The available data on K^+-meson production in the pp collisions [11, 12] demonstrate that the cross sections $d^2\sigma^{pp\to K^+X}/dM_{YN}d\Omega_K$ at different energies and in wide ranges of angles and momenta, including those used in our experiment, depend only on the mass M_{YN} of the undetectable system. It is worth noting that, due to the interaction between the nucleon and Λ-hyperon at small relative momenta in the final state, this cross section deviates from the phase-volume behavior at $M_{\Lambda N} < 2.11$ GeV and is virtually constant up to the threshold [11].

The factor N_1 in Eq. (8) specifies the absorption of the proton beam and the kaons produced in the target. It was determined from the relationship

$$N_1 = \frac{E_{K^+}d\sigma^{pA\to K+X}/d\mathbf{p}_K}{E_{K^+}d\sigma^{pp\to K+X}/d\mathbf{p}_K}, \tag{10}$$

where the numerator is the experimentally measured cross section and the denominator is the cross section for the pp collisions recalculated to the kinematics of our experiment with allowance made for the isotropic production of K^+-mesons in the C.M.S. [12]. The N_1 values were determined for proton energies of 2.54 and

2.88 GeV and proved to be the same for each nucleus. Table 2 presents the N_1 values used in the calculations.

The parameters of the momentum distributions for nucleons in the nuclei studied were determined by fitting Eq. (8) to the energy dependences measured for the K^+-production cross sections. It was found that the data obtained for the Al, Cu, and Ta nuclei can be described by a single-parameter $\sigma_1 = 155 \pm 8$ MeV/c distribution with $\chi^2 \sim 1$ per degree of freedom. The description for the Be nucleus is worse: $\chi^2 \approx 2$ and $\sigma_1 = 150 \pm 7$ MeV/c. The three-parameter description holds over a wide range of parameters upon their correlated changes. In particular, the σ_1 and h values at a fixed value $\sigma_2 = 220$ MeV/c are presented in Table 2. As one of the parameters changes by a value equal to the error indicated in the table, the χ^2 value per degree of freedom is doubled. Thus, the $n(q)$ form is universal for the nuclei studied, in agreement with the fact that at $q > 200$ MeV/c this distribution is independent of A for nuclei heavier than ^{4}He [13]. Recall that the calculations with the minimum E_R value were aimed at determining the lower bound for the contribution of high momenta to $n(q)$. The inclusion of the nucleon binding energy given by the shell model and the possible excitation or disintegration of the nuclei results in an increase in the σ_2 and h values specifying $n(q)$.

Figure 2 shows the results of corresponding calculations carried out for the Be nucleus and the computational results obtained under the assumption that the elementary $pp \longrightarrow K + X$ cross sections are proportional to the reaction phase volume. The latter results noticeably underestimate the experimental data at energies below 1.75 GeV.

Argumentation in favor of the direct mechanism of K^+ production. 1. An important argument in the determination of the reaction mechanism is provided by the comparison of the results of TPM calculation with the experimental data. To do this, the probability of pion production by protons on a nucleus with mass number A should be convolved with the cross section for K^+-meson production by pions:

$$E_{K^+}\frac{d\sigma_{\text{sec}}^{pA\to K^+X}(\mathbf{p}_0,\mathbf{p}_K)}{d\mathbf{p}_K} = 2N_2\int d\mathbf{p}_\pi f(\mathbf{p}_0,\mathbf{p}_\pi) \times\int d\mathbf{q}\,n(\mathbf{q})\left[E_{K^+}\frac{d\sigma^{\pi p\to K^+Y}(\sqrt{S_\pi},\mathbf{p}_K)}{d\mathbf{p}_K}\right]. \quad (11)$$

The calculations were carried out for the Be nucleus with the momentum distribution $n(q)$ obtained above. The factor N_2 in Eq. (11) is a product of the effective number of nucleons in the Be nucleus $\sigma_{in}^{p\text{Be}}/\sigma_{in}^{pp} = 5.9$ by the probability V of an intermediate pion interacting in the nucleus. For the forward-produced pions, the V value was taken in the form

$$V = (R^2 - l^2/4)/R^2, \quad (12)$$

Table 2

A	Be	Al	Cu	Ta
N_1	4.9	11.0	13.0	25.2
σ_1	132 ± 13	146 ± 15	146 ± 15	142 ± 20
h	0.12 ± 0.06	0.13 ± 0.06	0.12 ± 0.06	0.12 ± 0.08

where R is the radius of the target nucleus and $l = 3.5$ fm is the sum of the mean free paths of a proton and a pion [5]. The contribution of neutral pions to the cross section is accounted for by the factor 2. To increase the reliability of the calculation, we measured the momentum-dependent differential cross sections for the production of π^+- and π^--mesons in the pBe collisions at an angle of 10.5° and energies 1.7 and 2.25 GeV. The data corresponded to a change of the Feynman variable X_F^R from 0.5 to 0.95. In the indicated energy range, the pions of both signs showed, to a factor of 2, scaling in the X_F^R variable, as was observed in [14] for the production of π^--mesons at zero angle. This made it possible to approximate the cross sections for π^+-meson production in the range 0°–15° by the expression

$$f(\mathbf{p}_0,\mathbf{p}_\pi) = \frac{1}{\sigma_{\text{tot}}^{p\text{Be}}E_{\pi^+}}\left[E_{\pi^+}\frac{d\sigma^{p\text{Be}\to\pi^+X}(\mathbf{p}_0,\mathbf{p}_\pi)}{d\mathbf{p}_\pi}\right] = \frac{1}{\sigma_{\text{tot}}^{p\text{Be}}E_{\pi^+}}1300(X_F^R)^3(1-X_F^R)^{2+1.65X_F^R+4P_t^2}, \quad (13)$$

where P_t (GeV/c) is the transverse component of pion momentum; the experimentally measured invariant π^+-production cross sections are in mb GeV^{-2} sr^{-1} s^3; and $\sigma_{\text{tot}}^{p\text{Be}} = 170$ mb. The second integral in Eq. (11) relates the cross sections for kaon production in the pion–nucleus and pion–proton collisions to each other at the S_π value determined by the expression

$$S_\pi = (E_\pi + w)^2 - (\mathbf{p}_\pi + \mathbf{q})^2. \quad (14)$$

In describing the production of the $K^+\Sigma$ and $K^+\Lambda$ systems, the parametrizations of the angular distributions of K^+-mesons and the total cross sections at $\sqrt{S_\pi} > 1.9$ GeV were taken from [15, 16]. The method of calculation was described in [17]. The calculated TPM cross sections for K^+-meson production are shown in Fig. 2. The contribution of the cascade process does not exceed 5% of the cross sections measured for the Be nucleus.

2.This result can be used to estimate the TPM contribution for nuclei heavier than Be. In the above-threshold range $2.2 < T < 2.6$ GeV, the DPM dominates. This is confirmed by the fact that the experimental ratios $R(A/\text{Be})$ of the K^+-production cross sections on

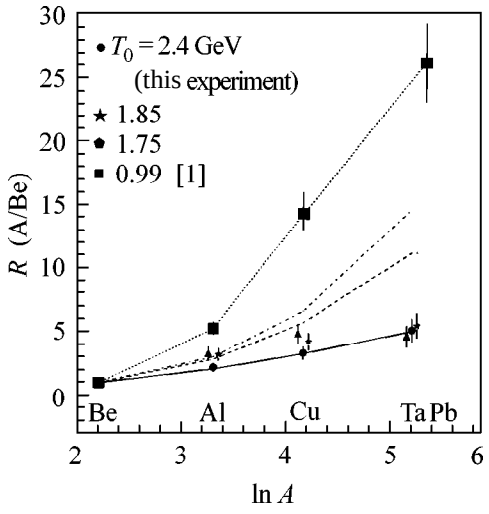

Fig. 3. Cross sections for the K^+ production as functions of mass number *A*. Calculated *A* dependences: solid line is for the direct production; dashed line is for the cascade production. The dash–dotted line is for the cascade production from [1].

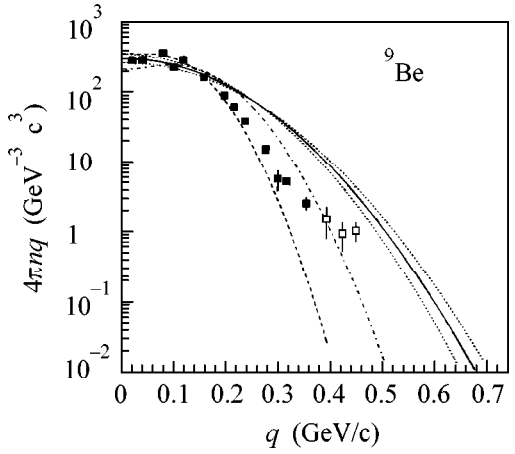

Fig. 4. Momentum distribution $n(q)$ for nucleons in the Be nucleus: (solid line) obtained in this work; (dotted lines) obtained for the doubled χ^2 value; (dashed line) calculated in the mean-field model; (dash–dotted line) obtained from Eq. (15) with $E_{\max}$ = 40 MeV; (■) measured in the ^{12}C(*e*, *e*'*p*)X reaction; and (□) given by the *Y*-scaling model for the ^{12}C(*e*, *e*'*p*)X reaction.

the *A* nucleus to those on the Be nucleus coincide with the corresponding values calculated with allowance made only for the absorption of proton and kaon. The results of these calculations and the experimental ratios are shown in Fig. 3 together with the TPM cross sections which depend on *A* appreciably stronger than for the direct process. In the subthreshold range $T < 1.9$ GeV, the *R* values for the Al and Cu nuclei increase by a factor of 1.5. In addition to the small TPM contribution for the Be nucleus, this gives an upper estimate of 1/3 for the contribution of the cascade processes on these nuclei. Note that the data in [1], where the TPM contribution dominates for the medium and heavy nuclei, show a considerably stronger *A* dependence. This dependence is also presented in Fig. 3, together with the cascade calculation allowing for the fact that the absorption of slow kaons detected in [1] is weaker. The calculation with inclusion of only the absorption yields a weaker *A* dependence.

Discussion. The dominance of DPM allows $n(q)$ to be treated as a nucleon momentum density determined for the Be and Al nuclei up to q = 0.65 GeV/*c* and for Cu up to q = 0.6 GeV/*c*. The distribution for the Be nucleus is shown in Fig. 4 by the solid line, and the function $n(q)$ corresponding to the doubled χ^2 value is shown by the dotted line. The Hartree–Fock mean-field $n(q)$ function is presented in the same figure. At $q >$ 0.35 GeV/*c*, the experimental distribution differs from the model calculations by several orders of magnitude. The $n(q)$ distribution extracted from the data on the ^{12}C(*e, e*'*p*)*X* reaction is also shown in the figure, together with the results of *Y*-scaling analysis of the ^{12}C(*e, e*')*X* reaction [13]. It is seen that the information on $n(q)$ obtained from the subthreshold production extends to considerably higher momenta than that from the electromagnetic interactions. With the assumptions accepted in this study, the distribution $n(q)$ is found to be the same for all nuclei studied.

Progress in the investigation of short-range nuclear structure allowed the quantitative characteristics to be obtained for the spectral functions $S(q, E_R)$ characterizing the probability of detecting the nucleon with momentum q and separation energy E_R. The spectral function is related to $n(q)$ through the expression

$$n(q) = \int_{E_{thr}}^{E_{\max}} S(q, E_R) dE_R, \qquad (15)$$

where E_{thr} is the threshold energy of nucleon separation. One can see from Fig. 2 that, after the substitution of Eq. (15) with $E_{\max}$ = 0.5 GeV into Eq. (8), the calculation strongly underestimates the experimental data in the deep-subthreshold region. This is due to the fact that the model implies a rapid increase in the average energy E_R with increasing nucleon momentum. In the experiment, the $E_R = E_{\max}$value does not exceed 30–40 MeV in the deep-subthreshold region, because a rapid decrease in the energy (6) of intranuclear nucleon hinders the production of K^+-mesons. For this reason, it is worthwhile to compare the distribution $n(q)$ obtained in this study with the calculations at indicated $E_{\max}$ values. The calculation with $E_{\max}$ = 40 MeV is presented in Fig. 4.

The observed contradiction with the experiment is to a great extent removed by taking into account the influence of effective potentials that reduce the masses of the baryons produced, together with a kaon, in the

nucleus [18]. Another possibility consists in the inclusion of the nonnucleonic degrees of freedom, which are disregarded in this study.

This work was supported by the Russian Foundation for Basic Research (project no. 96-02-18607) and by the International Science Foundation (grant nos. MBK000 and MBK300).

REFERENCES

1. V. Koptev, S. Mikirtych'yants, M. Nesterov, *et al.*, Zh. Éksp. Teor. Fiz. **94** (11), 1 (1988) [Sov. Phys. JETP **67**, 2177 (1988)].
2. M. Debovski, R. Barth, M. Boivin, *et al.*, Z. Phys. A **356**, 313 (1996).
3. A. Badala, R. Barbera, *et al.*, Phys. Rev. Lett. **80**, 4863 (1998).
4. N. Tarasov, M. Nesterov, and V. Koptev, Pis'ma Zh. Éksp. Teor. Fiz. **43**, 217 (1986) [JETP Lett. **43**, 274 (1986)].
5. W. Cassing, G. Batko, U. Mozel, *et al.*, Phys. Lett. B **238**, 25 (1990).
6. A. Sibirtsev and M. Buscher, Z. Phys. A **347**, 191 (1994).
7. S. Efremov and E. Paryev, Eur. Phys. J. A **1**, 99 (1998).
8. S. Frankel and W. Frati, Phys. Rev. C **16**, 1499 (1977).
9. Yu. B. Lepikhin, V. A. Smirnitskiĭ, and V. A. Sheĭnkman, Pis'ma Zh. Éksp. Teor. Fiz. **46**, 219 (1987) [JETP Lett. **46**, 275 (1987)].
10. A. Akindinov, M. Chumakov, *et al.*, Heavy Ion Phys. **4**, 325 (1996).
11. R. Siebert, J. Dideler, R. Frascaria, *et al.*, Nucl. Phys. A **567**, 819 (1994).
12. W. Hogan, P. Puroue, *et al.*, Phys. Rev. **166**, 1472 (1968).
13. C. Ciofi degli Atti and S. Simula, Phys. Rev. C **53**, 1689 (1996).
14. A. Moeller, L. Anderson, W. Brunkner, *et al.*, Phys. Rev. C **28**, 1246 (1983).
15. J. Cugnon and R. Lombard, Nucl. Phys. A **422**, 635 (1984).
16. K. Tsushima, S. Huang, and A. Faessler, Phys. Lett. B **337**, 245 (1994).
17. S. Efremov and É. Par'ev, Yad. Fiz. **59**, 2143 (1996) [Phys. At. Nucl. **59**, 2063 (1996)].
18. E. Paryev, Eur. Phys. J. A **5**, 307 (1999).

Translated by R. Tyapaev

JETP Letters, Vol. 72, No. 3, 2000, pp. 106–110. From Pis'ma v Zhurnal Éksperimental'noĭ i Teoreticheskoĭ Fiziki, Vol. 72, No. 3, 2000, pp. 157–162.

Tilted Rotation and Wobbling Motion in Nuclei[1]

W. D. Heiss* and R. G. Nazmitdinov,*****

** Center for Nonlinear Studies and Department of Physics, University of the Witwatersrand, 2050, Johannesburg, South Africa*

*** Bogoliubov Laboratory of Theoretical Physics, Joint Institute for Nuclear Research, Dubna, Moscow Region, 141980 Russia*

**** e-mail: rashid@thsun1.jinr.ru*

Received June 30, 2000

The self-consistent harmonic oscillator model including the three-dimensional cranking term is extended to describe collective excitations in the random phase approximation. It is found that quadrupole collective excitations associated with wobbling motion in rotating nuclei lead to the appearance of two- or three-dimensional rotation. © *2000 MAIK "Nauka/Interperiodica".*

PACS numbers: 21.60.Ev

Nuclear states grouped into $\Delta I = 2$ sequences are remarkably well described in terms of the principal axis rotation, which is the basis of the cranking model [1]. The principal axis cranking rotation was intuitively justified by a classical rigid body rotation which is favorable for a uniform rotation around the long or the short principal axis. However, if the classical body is not rigid, it may also uniformly rotate about an axis which does not coincide with the principal axes of the density distribution. In fact, more than a century ago, Riemann [2] pointed out that such a situation could occur in an ellipsoidal self-gravitating fluid. The physical mechanism behind it is the vortex motion in a macroscopic system.

Numerous experimental observations implying $\Delta I = 1$ sequences in near-spherical nuclei [3] raised the question about a new type of rotation and its physical nature in a finite quantum many-body system. For particular nuclei, the proton and neutron spin vectors may be oriented along different axes. Consequently, the total angular momentum could lie at an angle different from one of the principal axes, i.e., at a tilted angle. It seems that shell effects are the driving forces in this case, which can be described within the Tilted Axis Cranking Model [4], which assumes a two-dimensional rotation. Other intriguing examples are the rotational bands observed in *Hf*, *W* and *Os* (Z = 72–76) nuclei with $A \sim 180$ [5–7]. These bands are characterized by high K-values, where K is the angular momentum projection on the body-fixed symmetry axis [8]. At finite rotational frequency, competition could occur between states with large collective angular momentum oriented perpendicular to the symmetry axis and high-K states. Such competition gives rise to the new backbending phenomenon, which is expected to be caused by the crossing of the ground and tilted rotational bands [4]. The one-dimensional cranking model based on the signature concept (the invariance of the wave function under rotation by π around the rotational axis) fails in this situation, since signature is not conserved for tilted rotations. Furthermore, according to the standard Alaga rules [1, 8], the quadrupole $B(E2)$ transitions to the ground band are forbidden due to the K selection rules ($K > 2$). However, it is observed that some K-isomer states do decay via quadrupole transitions to the ground state. It was suggested that either fluctuations in the orientation of the angular momentum, or shape fluctuations [6], or tilting degrees of freedom in the rotation axis [5] are responsible for this phenomenon. It was also observed that the $\Delta I = 2$ sequence of the rotational states was superseded by $\Delta I = 1$ transitions in the yrast rotational band at high rotational frequency. In the present paper, we extend a previous study [9] and demonstrate that tilted rotations naturally occur beyond a critical rotational frequency as an instability of collective vibrations caused by the wobbling motion.

At high spin, the dynamical fluctuations of the shape and angular momentum vector can be described by the cranking random phase approximation (CRPA) as formulated in [10, 11] for a one-dimensional rotation. This approach is the main theoretical tool used for the analysis of collective excitations in rotating nuclei (see [12–14] and references therein). To understand the main features of the formation of tilted bands, we assume the angular momentum and shape fluctuations to be dominant. For comparison with experimental data, pairing vibrations [13, 15] should be taken into account; but this degree of freedom does not change our main conclusions: it involves tedious calculations to be postponed for future publication. The CRPA and RPA calculations for nonrotating nuclei suffer from the inconsistency between the basis generated by the mean field

[1] This article was submitted by the authors in English.

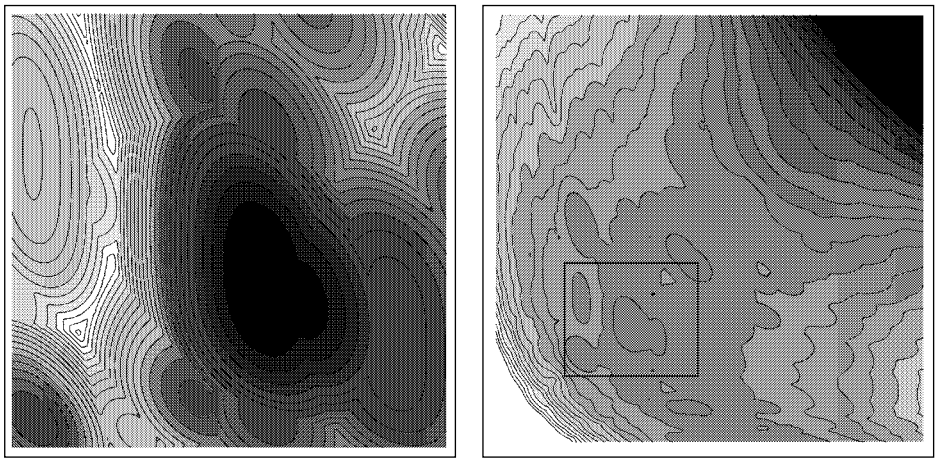

Fig. 1. Energy contours in the ω_x–ω_y plane for the rotational speed where the onset of an oblate shape has just taken place and corresponds to the local minimum shown in the left figure. However, for the nucleus considered ($N = 44$, triaxial near-prolate), a much deeper minimum has developed as an instability, as seen in the top right corner of the right figure. The section of the left illustration is indicated in the right part.

and the residual two-body interaction. To facilitate analytical and numerical results and to avoid spurious solutions due to such inconsistencies, we base our analysis upon the three-dimensional harmonic oscillator model. We start with the single-particle Routhian

$$H_\Omega = H_0 - \mathbf{\Omega}\cdot\mathbf{L}$$
$$\equiv \sum_{j=1}^{N}\left(\frac{1}{2m}\mathbf{p}_j^2 + \frac{m}{2}(\omega_x^2 x_j^2 + \omega_y^2 y_j^2 + \omega_z^2 z_j^2) - \mathbf{\Omega}\cdot\mathbf{l}_j\right), \quad (1)$$

where the rotational vector $\mathbf{\Omega}$ of the cranking term has the components $(\Omega_x, \Omega_y, \Omega_z) \equiv \Omega(\sin\theta\cos\phi, \sin\theta\sin\phi, \cos\theta)$. The Hamiltonian (1) represents the simplest mean-field Hamiltonian, which reproduces quite well the main properties of rotating nuclei [8, 16]. The spectrum of this Hamiltonian, i.e., the eigenmodes, is obtained by solving a third-order polynomial in E^2. The normal mode operators $a_k^\dagger$ and a_k, $k = 1, 2, 3$ ($[a_k, a_l^\dagger] = \delta_{k,l}$) are linear transformations in the coordinates q_i and momenta p_i ($i = x, y, z$) with complex coefficients. In this way, we obtain

$$H_\Omega = \sum_{j=1}^{N}\sum_{i=1,2,3} E_i(n_i + 1/2)_j$$

with $n_i = a_i^\dagger a$. The normal modes are filled from the bottom, which gives the ground state energy in the rotating frame $E_{\rm tot} = E_1\sum_1 + E_2\sum_2 + E_3\sum_3$, where $\sum_k = \left\langle \sum_j^N (n_k + 1/2)_j \right\rangle$, and the configuration is determined by $\sum_1 \le \sum_2 \le \sum_3$.

The minimization of the Hamiltonian (1) with respect to the three frequencies ω_i, subject to the volume conservation condition $\omega_x\omega_y\omega_z = \omega_0^3$, yields the self-consistency relation

$$\omega_x^2\langle x^2\rangle = \omega_y^2\langle y^2\rangle = \omega_z^2\langle z^2\rangle. \quad (2)$$

These energy minima and their corresponding values for ω_i depend on the rotational vector $\mathbf{\Omega}$. For a given Ω, we search for tilted solutions by seeking the minimum in the θ–ϕ plane [9]. Three major results are reported here:

(1) Starting from oblate, prolate, or triaxial shapes, for sufficiently high values of Ω, a local minimum, which is characterized by an oblate shape with the symmetry axis coinciding with the rotational axis ($\theta = 90°$, $\phi = 0°$), is *always* obtained.

(2) Increasing further the value of Ω, this local minimum shifts away from $\theta = 90°$ to $\theta < 90°$ and possibly $\phi > 0°$, thus giving rise to a two- or three-dimensional rotation.

(3) Only when starting from triaxial near-oblate nuclei is this specific local minimum a global and stable minimum. For prolate nuclei, this local minimum is attained only for values of Ω so large that other (possibly unphysical) minima *with different configurations* occur at a considerably lower energy; see Fig. 1. When starting from the outset with an oblate nucleus, the global minimum is obtained for the rotational axis perpendicular to the symmetry axis; the specific local minimum referred to above is then the second lowest minimum with the *same* configuration.

We first focus our attention on triaxial near-oblate nuclei. Here we encounter two critical values. At $\Omega_{cr}^{(1)}$, there is a shape transition from triaxial to axial (oblate) symmetry. This axial shape remains unchanged for a range $\Omega_{cr}^{(1)} \le \Omega \le \Omega_{cr}^{(2)}$, where $\Omega_{cr}^{(2)}$ signifies the onset of a tilted rotation where the rotational axis no longer

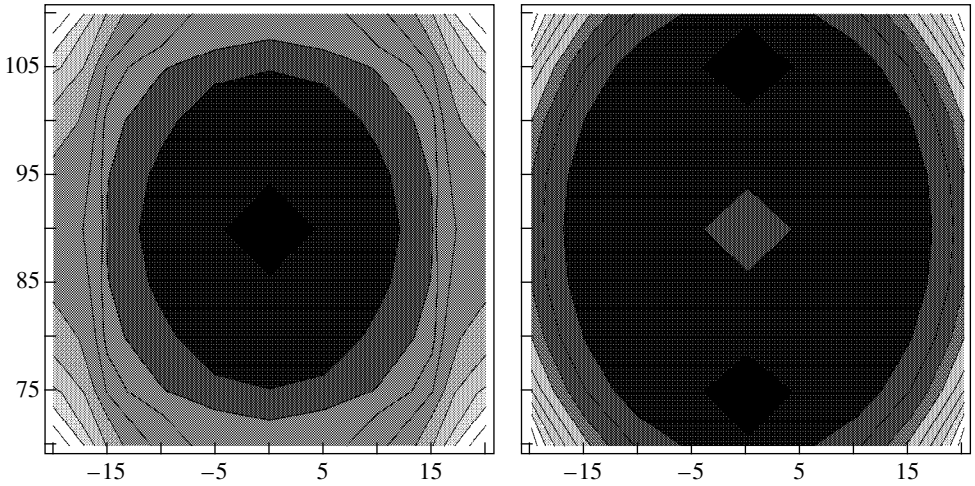

Fig. 2. Energy minimum in the ϕ–θ plane just before (left) and after (right) the onset of tilted rotation. Note the local maximum developed at the center. The example chosen is $N = 36$, a triaxial near-oblate nucleus.

coincides with a principal axis. Note that for $0 \le \Omega \le \Omega_{cr}^{(2)}$ the rotational axis is aligned to a principal axis which becomes the symmetry axis for $\Omega \ge \Omega_{cr}^{(1)}$. At this point, there is a confluence in the energy contours $E(\omega_y, \omega_z)$ of two minima into one at $\omega_\perp = \omega_y = \omega_z$. In contrast, at the larger value $\Omega = \Omega_{cr}^{(2)}$, the minimum at $\theta = 90°$, $\phi = 0°$ bifurcates into two minima, as illustrated in Fig. 2. The two minima occurring at $\theta = 75°$ and $\theta = 105°$ ($\phi = 0°$) appear at first glance to be physically equivalent. However, they are not, as can be seen when Ω is increased further, in which case they move into positions with different values of ϕ (and θ) and only one is the global minimum. In fact, the directions of $\mathbf{\Omega}$ play a different role in the different octants [17]. We interpret the rotation for $\Omega_{cr}^{(1)} \le \Omega \le \Omega_{cr}^{(2)}$ as a *K*-isomer. For the tilted rotation, the symmetric shape no longer prevails.

While these findings are obtained from the numerical minimization procedure, we now further substantiate our analysis by an analytical procedure. Using the fact that the first critical rotational frequency is associated with a one-dimensional rotation, we exploit in Eq. (2) the fact that at the transition point $\omega_y = \omega_z = \omega_\perp$ and obtain a third-order equation

$$u^3 - \frac{u}{2} + \frac{1}{2}\frac{r-1}{r+1} = 0, \tag{3}$$

where $u = \Omega/\omega_\perp$ and $r = \sum_3 / \sum_2$. From the discriminant of Eq. (3), we obtain the critical value $r_{cr} = (\sqrt{27} + \sqrt{2})(\sqrt{27} - \sqrt{2})$. It was shown in [18] that a prolate system eventually becomes oblate, with the rotational axis coinciding with the symmetry axis, if the initial deformation obeys $r < r_{cr}$. However, according to our results, this case is not a global energy minimum; in fact, the global minimum is unphysical. In general, for $r < r_{cr}$ we obtain three solutions:

$$u = \sqrt{\frac{2}{3}}\cos\left(\frac{\chi + 2\pi n}{3}\right), \quad n = 0, 1, 2, \tag{4}$$

$$\cos\chi = 3\sqrt{\frac{3}{2}}\frac{1-r}{1+r}. \tag{5}$$

These values of the rotational frequency correspond to three bifurcation points. Below we demonstrate that one of these solutions is the critical point $\Omega_{cr}^{(1)}$ where the lowest vibrational frequency tends to zero.

The variations in the one-body potential around the equilibrium deformation determine the effective quadrupole–quadrupole interaction [19]. The total Hamiltonian can be presented as

$$H = H_\Omega - \frac{\kappa}{2}\sum_{\mu=-2}^{2} Q_\mu^\dagger Q_\mu \equiv \tilde{H} - \mathbf{\Omega}\cdot\mathbf{L}. \tag{6}$$

While the mean-field Hamiltonian (1) breaks the rotational symmetry, the Hamiltonian (6) fulfills the commutation rules $[H, L_i] = 0$, $i = x, y, z$. Note that the self-consistent condition (2) fixes the quadrupole strength constant κ in the RPA calculations. We solve the RPA equation of motion for the general coordinates $\mathscr{X}_\lambda$ and momenta $\mathscr{P}_\lambda$ (see for details [12]):

$$\begin{aligned} [H, \mathscr{X}_\lambda] &= -i\omega_\lambda \mathscr{P}_\lambda, \\ [H, \mathscr{P}_\lambda] &= i\omega_\lambda \mathscr{X}_\lambda, \quad [\mathscr{X}_\lambda, \mathscr{P}_{\lambda'}] = i\delta_{\lambda,\lambda'}. \end{aligned} \tag{7}$$

Here, ω_λ is the RPA eigenfrequency in the rotating frame and the associated phonon $O_\lambda^\dagger = (\mathscr{X}_\lambda - i\mathscr{P}_\lambda)/\sqrt{2}$. In contrast to the CRPA approach, the phonon in the present model is a superposition of different signature

phonons. The degree of the mixture depends on the tilted angle: the signature and $|K|$ are good quantum numbers, respectively, for rotations perpendicular and parallel to the symmetry axis. The nonzero solutions appear in pairs $\pm\hbar\omega_\lambda$; we choose solutions with positive norm.

Let us first focus on the RPA solution which leads to the transition from the nonaxial to the oblate regime of rotation. Since at this transition point the minimal solution corresponds to a one-dimensional rotation $[\mathbf{\Omega} \equiv (\Omega, 0, 0)]$ about the symmetry axis, the angular momentum becomes a good quantum number. The RPA states can be characterized by the projection of the angular momentum, because $[L_x, O^\dagger_\lambda] = \lambda O^\dagger_\lambda$. Consequently, we obtain

$$\begin{aligned}[H, O^\dagger_\lambda] &= [\tilde{H} - \Omega L_x, O^\dagger_\lambda] \\ &= (\tilde{\omega}_\lambda - \lambda\Omega) O^\dagger_\lambda \equiv \omega_\lambda O^\dagger_\lambda.\end{aligned} \tag{8}$$

From Eq. (8) it follows that at the rotational frequency $\Omega_{cr} = \tilde{\omega}_\lambda/\lambda$ one of the RPA frequencies should be equal to zero. The solution of the RPA equation for the positive signature quadrupole phonons with the largest projection $\lambda = -2$ gives

$$\omega_{\lambda=-2} = -\omega_\perp\sqrt{\frac{2}{3}}\left(\cos\frac{\chi+\pi}{3} - \sqrt{3}\sin\frac{\chi+\pi}{3}\right) + 2\Omega. \tag{9}$$

This mode corresponds to the quadrupole de-excitation which leads to the state with two units of angular momentum less than the vacuum state (K-isomer state). From Eq. (9), we obtain the first critical value of the rotational frequency at which the transition from noncollective rotation to nonaxial collective rotation takes place:

$$\Omega^{(1)}_{cr} = \omega_\perp\frac{1}{2}\sqrt{\frac{2}{3}}\left(\cos\frac{\chi+\pi}{3} - \sqrt{3}\sin\frac{\chi+\pi}{3}\right). \tag{10}$$

Therefore, the positive signature quadrupole de-excitation leads from the K-isomer state to the yrast state with the nonaxial quadrupole shape.

Quantum excitations describing the wobbling motion correspond to the negative signature quadrupole phonons [10, 11, 20]. These excitations are connected to the yrast line by means of the quadrupole transitions which carry one unit of the angular momentum. Similar to the positive signature phonons, the negative signature phonons can have zero excitation energy at a particular rotational frequency. Solution of the RPA equation for the negative signature phonons with $\lambda = -1$ for the oblate rotation regime leads to the result

$$\omega_{\lambda=-1} = -\sqrt{\frac{\omega_x^2 + \omega_\perp^2}{3}}\left(\cos\frac{\psi}{3} - \sqrt{3}\sin\frac{\psi}{3}\right) + \Omega, \tag{11}$$

$$\cos\psi = 3\sqrt{3}\frac{\omega_x^2\omega_\perp}{(\omega_x^2 + \omega_\perp^2)^{3/2}}\frac{r-1}{1+r}. \tag{12}$$

The condition $\omega_{\lambda=-1} = 0$ yields the second critical frequency

$$\Omega^{(2)}_{cr} = \sqrt{\frac{\omega_x^2 + \omega_\perp^2}{3}}\left(\cos\frac{\psi}{3} - \sqrt{3}\sin\frac{\psi}{3}\right). \tag{13}$$

Beyond this rotational frequency, the mean-field solution corresponds to the stable tilted rotation. We recall that the expressions given by Eqs. (10) and (13) coincide exactly with the transitional points found in the numerical minimization procedure. Note that, in contrast to the familiar phase transition from spherical to deformed shape owing to the variation of a strength parameter [1], here it is the rotation that leads to a phase transition from triaxial to oblate shape and then to the tilted rotation associated again with a nonaxial shape for the same strength parameter of the residual quadrupole–quadrupole interaction.

According to our analysis, only nuclei near to oblate shape when nonrotational exhibit tilted rotation at a certain rotational frequency, which, for lesser rotational speeds, leads to the high K-isomer states. These states decay through nonaxial shapes to the ground states. Nuclei which are oblate when nonrotational can also have this behavior, which corresponds to the second (local) minimum discussed above. However, they also have states of good signature with an even lower energy for the same rotational speed and the same configuration. In contrast, for prolate nuclei, the local minimum with these characteristics occurs only at a value $\mathbf{\Omega}$ so large that the global minimum occurs for an absurdly unphysical configuration.

R.G.N. acknowledges financial support from the Foundation for Research Development of South Africa. He is also thankful for the warm hospitality which he received from the Department of Physics during his visit to South Africa. W.D.H. is grateful for the congenial hospitality at the JINR. This work was supported in part by the Russian Foundation for Basic Research, project no. 00-02-17194.

REFERENCES

1. P. Ring and P. Schuck, *The Nuclear Many-Body Problem* (Springer-Verlag, Berlin, 1980).
2. B. Riemann, Abh. K. Ges. Wiss. Goettingen **9**, 1 (1860).
3. R. M. Clark, S. J. Asztalos, B. Busse, *et al.*, Phys. Rev. Lett. **82**, 3220 (1999); H. Schnare, R. Schwengner, S. Frauendorf, *et al.*, Phys. Rev. Lett. **82**, 4408 (1999); D. G. Jenkins, R. Wadsworth, J. A. Cameron, *et al.*, Phys. Rev. Lett. **83**, 500 (1999); D. G. Jenkins, R. Wadsworth, J. Cameron, *et al.*, Phys. Rev. C **58**, 2703 (1998); O. Vogel, A. Dewald, P. von Brentano, *et al.*, Phys. Rev. C **56**, 1338 (1997); R. M. Clark, J. Phys. G **25**, 695 (1999).
4. S. Frauendorf, Nucl. Phys. A **557**, 259 (1993); Rev. Mod. Phys. (in press).
5. P. M. Walker, K. C. Yeung, G. D. Dracoulis, *et al.*, Phys. Lett. B **309**, 17 (1993).

6. B. Crowell, P. Chowdhury, S. J. Freeman, *et al.*, Phys. Rev. Lett. **72**, 1164 (1994).
7. T. Kutsarova, R. M. Lieder, H. Schnare, *et al.*, Nucl. Phys. A **587**, 111 (1995); N. L. Gjrup, P. M. Walker, G. Sletten, *et al.*, Nucl. Phys. A **582**, 369 (1995); C. J. Pearson, P. M. Walker, C. S. Purry, *et al.*, Phys. Rev. Lett. **79**, 605 (1997); C. S. Purry, P. M. Walker, G. D. Dracoulis, *et al.*, Nucl. Phys. A **632**, 229 (1998).
8. A. Bohr and B. R. Mottelson, in *Nuclear Structure* (Benjamin, New York, 1975), Vol. II.
9. W. D. Heiss and R. G. Nazmitdinov, Phys. Lett. B **397**, 1 (1997).
10. E. R. Marshalek, Nucl. Phys. A **266**, 317 (1976).
11. D. Janssen and I. N. Mikhailov, Nucl. Phys. A **318**, 390 (1979).
12. J. Kvasil and R. G. Nazmitdinov, Fiz. Élem. Chastits At. Yadra **17**, 613 (1986) [Sov. J. Part. Nucl. **17**, 265 (1986)].
13. Y. R. Shimizu, J. D. Garrett, R. A. Broglia, *et al.*, Rev. Mod. Phys. **61**, 131 (1989).
14. T. Nakatsukasa, K. Matsuyanagi, S. Mizutori, and Y. R. Shimizu, Phys. Rev. C **53**, 2213 (1996).
15. F. Dönau, D. Almehed, and R. G. Nazmitdinov, Phys. Rev. Lett. **83**, 280 (1999).
16. S. G. Nilsson and I. Ragnarsson, *Shapes and Shells in Nuclear Structure* (Cambridge Univ. Press, Cambridge, 1995).
17. V. I. Dimitrov, S. Frauendorf, and F. Dönau, Phys. Rev. Lett. **84**, 5732 (2000).
18. T. Troudet and R. Arvieu, Ann. Phys. (N.Y.) **134**, 1 (1981).
19. T. Kishimoto, J. M. Moss, D. H. Youngblood, *et al.*, Phys. Rev. Lett. **35**, 552 (1975); H. Sakamoto and T. Kishimoto, Nucl. Phys. A **501**, 205 (1989) and references therein.
20. D. Janssen, I. N. Mikhailov, R. G. Nazmitdinov, *et al.*, Phys. Lett. B **79**, 347 (1978).

JETP Letters, Vol. 72, No. 3, 2000, pp. 111–114. From Pis'ma v Zhurnal Éksperimental'noĭ i Teoreticheskoĭ Fiziki, Vol. 72, No. 3, 2000, pp. 163–167.

On the Boundary of the Dispersion-Managed Soliton Existence[1]

P. M. Lushnikov

Landau Institute for Theoretical Physics, Russian Academy of Sciences, ul. Kosygina 2, Moscow, 117990 Russia
Theoretical Division, Los Alamos National Laboratory, Los Alamos, New Mexico, 87545
e-mail: lushnikov@lanl.gov

Received June 19, 2000; in final form, July 12, 2000

A breathing soliton-like structure in a dispersion-managed optical fiber system is studied. It is proved that, for negative average dispersion, the breathing soliton is forbidden, provided that the modulus of average dispersion exceeds a threshold which depends on the soliton amplitude. © *2000 MAIK "Nauka/Interperiodica".*

PACS numbers: 42.65.Tg; 05.45.Yv; 42.79.Sz; 42.81.Dp

Propagation of an optical pulse in nonlinear media with varying dispersion is both a fundamental [1] and an important applied problem [2–8], because the dispersion-managed (DM) system, which is a system with periodic dispersion variation along an optical fiber, is one of the most prospective candidates for ultrafast high-bit-rate optical communication lines. Lossless propagation of an optical pulse in a DM fiber is described by a nonlinear Schrödinger equation (NLS) with periodically varying dispersion $d(z)$:

$$iu_z + d(z)u_{tt} + |u|^2 u = 0, \qquad (1)$$

where u is the envelope of the optical pulse, z is the propagation distance, and all quantities are dimensionless. Consider a two-step periodic dispersion map $d(z) = d_0 + \tilde{d}(z)$, where $\tilde{d}(z) = d_1$ for $0 < z + nL < L_1$ and $\tilde{d}(z) = d_2$ for $L_1 < z + nL < L_1 + L_2$; d_0 is the path-averaged dispersion; d_1 and d_2 are the amplitudes of dispersion variation subject to the condition $d_1L_1 + d_2L_2 = 0$; $L \equiv L_1 + L_2$ is the dispersion compensation period; and n is an arbitrary integer number. Equation (1) also describes the pulse propagation in a fiber with losses compensated by periodically placed amplifiers, if the distance between amplifiers is much less than L.

In a linear regime, in which the nonlinear term in Eq. (1) is negligible, the periodical variation of dispersion is a way to overcome pulse broadening due to chromatic dispersion, provided that the residual dispersion d_0 is small enough. However, in a real optical fiber, the nonlinear term in Eq. (1) is important, because the optical pulse amplitude should be large enough to get a high signal/noise ratio. One of the fascinating features of the DM system is the numerical observation of a space-breathing soliton-like structure, which is called the DM soliton, for both positive and negative residual dispersion d_0 [9]. This observation is in sharp contrast with the system described by the NLS with constant dispersion, where stable soliton propagation is possible only for positive dispersion [10], because the nonlinearity can continuously compensate the positive dispersion only. In the DM soliton, the balance between the nonlinearity and dispersion is achieved, on average, over the dispersion period L, which lifts the requirement for the positive dispersion sign. Nevertheless, it was never proved that the DM soliton really exists, because there is a possibility that this is a rather long-lived quasi-stable breathing pulse which decays in a long distance z. It is shown here that for negative d_0 a DM soliton can exist only if $|d_0|$ is small enough to allow nonlinear compensation of pulse broadening due to the dispersion over distance L.

Equation (1) can be written in the Hamiltonian form $iu_z = \delta H/\delta u^*$, where the Hamiltonian

$$H = \int \left[d(z)|u_t|^2 - \frac{|u|^4}{2} \right] dt \qquad (2)$$

is an integral of motion on each interval of a constant dispersion $d(z) = \text{const}$. Equation (1) is reduced to the usual NLS on such intervals. At points $z = nL$ and $z = nL + L_1$, where n is an arbitrary integer number, the Hamiltonian experiences jumps due to jumps of the dispersion, although the value of u is a continuous function of z at these points. In contrast to the Hamiltonian, the time-averaged optical power $N = \int |u|^2 dt$, or number of particles in the quantum mechanical interpretation of NLS (in this interpretation, the coordinate z means some "time" and actual time t has the meaning of "coordinate") is an integral of motion for all z. Consider the z dependence of the quantity $A = \int t^2 |u|^2 dt$. A/N is the average width of a time distribution of u, or simply $\langle t^2 \rangle$ in the quantum mechanical interpretation of NLS.

[1] This article was submitted by the authors in English.

Using (1) and integrating by parts, one gets for the first z derivative

$$A_z = d(z)\int 2it(uu_t^* - u^*u_t)dt. \quad (3)$$

In a similar way after the second differentiation with respect to z, one gets

$$A_{zz} = 4dH + 4d^2X + \frac{d_z}{d}A_z, \quad (4)$$

where $X \equiv \int |u_t|^2 dt$. It follows from Eq. (3), which is often called the virial theorem (see, e.g., [11, 12]), that A_z experiences finite jumps corresponding to jumps of a step-wise function $d(z)$:

$$\begin{aligned} A_z|_{z = L_1 + 0} &= \frac{d_0 + d_2}{d_0 + d_1}A_z\Big|_{z = L_1 - 0}, \\ A_z|_{z = L + 0} &= \frac{d_0 + d_1}{d_0 + d_2}A_z\Big|_{z = L - 0}. \end{aligned} \quad (5)$$

Set $X(z) = X_0 + \delta X(z)$, $X(0) \equiv X_0$; then one can integrate Eq. (4) over the intervals $(0, L_1)$, (L_1, L):

$$\begin{aligned} A_z|_{z = L_1 - 0} &= A_z|_{z = 0 + 0} \\ &+ 4\int_0^{L_1} [(d_0 + d_1)H_1 + (d_0 + d_1)^2 X]dz, \\ A_z|_{z = L - 0} &= A_z|_{z = L_1 + 0} \\ &+ 4\int_{L_1}^{L} [(d_0 + d_2)H_2 + (d_0 + d_2)^2 X]dz, \end{aligned} \quad (6)$$

where

$$\begin{aligned} H_1 &= (d_0 + d_1)X_0 - Y_0, \\ H_2 &= (d_0 + d_2)X_0 - Y_0 - (d_1 - d_2)\delta X|_{z = L_1} \end{aligned} \quad (7)$$

are the Hamiltonian values on the intervals $(0, L_1)$, (L_1, L) respectively:

$$Y(z) \equiv \int \frac{|u|^4}{2}dt, \quad Y_0 \equiv Y(0).$$

Here, the conservation of H_1 on interval $(0, L_1)$ is used in deriving the expression for H_2.

The DM soliton solution of Eq. (1) (see [13]) is given by $u = \tilde{u}(z, t)\exp(ikz)$, where k is an arbitrary real constant and $\tilde{u}(z + L, t) = \tilde{u}(z, t)$ is a periodic function of z, $\tilde{u}(z, t)|_{|t| \to \infty} \longrightarrow 0$. Thus, for a DM soliton $A_z|_{z = L + 0} = A_z|_{z = 0 + 0}$. This condition can be recast, via Eqs. (5)–(7), into the form

$$\begin{aligned} &L(d_1 + d_0)\left[2d_0X_0 - Y_0 + (d_1 - d_2)\frac{L_2}{L}\delta X\Big|_{z = L_1}\right] \\ &+ \int_0^{L_1} (d_0 + d_1)^2 \delta X dz + \int_{L_1}^{L} (d_0 + d_2)^2 \delta X dz = 0. \end{aligned} \quad (8)$$

The next step is to consider the $\delta X(z)$ dependence. Using Eq. (1) and integrating by parts, one can get

$$X_z = 4\int \phi_t R_t R^3 dt, \quad (9)$$

where $u \equiv Re^{i\phi}$, ϕ and R are real, and $R \geq 0$. Consider an upper bound of X_z, which is given by a chain of inequalities

$$4\int \phi_t R_t R^3 dt \leq 4\max(R^2)\int |\phi_t R_t R| dt \leq 4X^{3/2}N^{1/2}, \quad (10)$$

where the following inequalities are used:

$$\begin{aligned} 2\phi_t R_t R &\leq (\phi_t R)^2 + R_t^2, \\ \max(R^2) &\leq \int_{-\infty}^{t} |(R^2)_{t'}| dt' \\ &\leq \int |(R^2)_t| dt \leq 2\int R|R_t| dt \leq 2N^{1/2}X^{1/2} \end{aligned} \quad (11)$$

(in the last expression, the Cauchy–Schwarz inequality is also used). Equations (9) and (10) can be integrated over z to give (it is assumed below that $2X_0^{1/2}N^{1/2}\max(L_1, L_2) < 1$)

$$X \leq X_0/(1 - 2X_0^{1/2}N^{1/2}z)^2. \quad (12)$$

In a similar way, using inequality $X_z \geq -4\int |\phi_t R_t| R^3 dt$ following from Eq. (9), one can get the lower bound for $X(z)$:

$$X \geq X_0/(1 + 2X_0^{1/2}N^{1/2}z)^2. \quad (13)$$

For the DM soliton $X(L) = X_0$, and, thus, it is more convenient to use similar inequalities for $L_1 < z < L$:

$$\begin{aligned} &\frac{X_0}{(1 + 2X_0^{1/2}N^{1/2}(L - z))^2} \\ &\leq X \leq \frac{X_0}{(1 - 2X_0^{1/2}N^{1/2}(L - z))^2}. \end{aligned} \quad (14)$$

Equations (8), (12)–(14) result in the inequality

$$|2d_0X_0 - Y_0| \le \frac{|d_1 - d_2|L_2X_0}{L}\left[\frac{1}{(1 - 2X_0^{1/2}N^{1/2}L_1)^2} - 1\right] + \frac{2X_0^{3/2}N^{1/2}}{|d_0 + d_1|L}\left[\frac{(d_0 + d_1)^2L_1^2}{1 - 2X_0^{1/2}N^{1/2}L_1} + \frac{(d_0 + d_2)^2L_2^2}{1 - 2X_0^{1/2}N^{1/2}L_2}\right]. \quad (15)$$

Equation (15) is the main result of this paper. Equation (15) is a consequence of the initial assumption that the DM soliton exists for given parameters L_1, L_2, d_0, d_1, d_2 and integral values X_0, Y_0, N, which depend on $u|_{z=0}$ only. Thus, the DM soliton can exist only if this inequality is fulfilled.

Note that if one assumes uniqueness of the DM soliton solution for a given k and soliton width, then, as shown in [13], $|u|_{z=0} = |u|_{z=L_1}$. In such a case, the term $\delta X|_{z=L_1}$ in Eq. (8) vanishes and instead of (15), one can get a more strict inequality. However, this possibility is disregarded here for the sake of generality.

To clarify the physical consequences of Eq. (15), consider an optical pulse with a typical amplitude p and a typical time width t_0. Then, $N \sim |p|^2t_0$, $X_0 \sim |p|^2/t_0$ and, thus, $X_0^{1/2}N^{1/2}L \sim L/Z_{nl}$, where $Z_{nl} = 1/|p|^2$ is the characteristic nonlinear length. In typical experimental conditions, the nonlinearity is small: $L/Z_{nl} \ll 1$, and the denominators in (15) can be expanded in series to give

$$|2d_0X_0 - Y_0| \le \frac{2X_0^{3/2}N^{1/2}}{L} \times \left[2|d_1 - d_2|L_1L_2 + |d_0 + d_1|L_1^2 + \frac{(d_0 + d_2)^2L_2^2}{|d_0 + d_1|}\right] + O\left(\frac{d_1L^3}{t_0Z_{nl}^3}\right). \quad (16)$$

Provided that d_0 is negative, both terms on the left-hand side of Eq. (16) have the same sign and, thus, the right-hand side should be greater than, or equal to, $2|d_0|X_0 + Y_0$. Assuming $d_1 \gg |d_0|$, one can get from Eq. (16) the following estimate ($Y_0 \sim t_0/Z_{nl}^2$):

$$\frac{2|d_0|}{t_0Z_{nl}} + \frac{t_0}{Z_{nl}^2} \lesssim \frac{4L_1d_1}{Z_{nl}^2t_0}\left(1 + \frac{L_1}{L}\right). \quad (17)$$

Consider the strong dispersion management limit $Z_{disp}/L \ll 1$, where $Z_{disp} \equiv t_0^2/d_1$ is the typical dispersion length. This limit implies that the optical pulse experiences strong oscillation at each period L due to the dispersion. Then Eq. (17) reduces to

$$-\frac{d_0}{d_1} \lesssim \frac{6L_1}{Z_{nl}}\left(1 + \frac{L_1}{L}\right), \quad (18)$$

i.e., a nonlinearity (amplitude of the optical pulse) should be strong enough to allow the DM soliton solution to exist for a given negative d_0.

Equation (15) gives the necessary, but not sufficient, condition for the existence of the DM soliton. In other words, the violation of inequality (15) means that the DM soliton is forbidden. Of course, it would be interesting to find to what extent this necessary condition for existence is close to the sufficient one. In general, this could be done only if one found the DM soliton analytically.

Here, one can only mention that there is a qualitative correspondence between the threshold of DM soliton existence, following from the analytical condition (15) and from the numerical investigation of the DM soliton. Namely, the maximum value of $|d_0|$ ($d_0 < 0$) for which the DM soliton exists grows with an increase in the dispersion map strength L/Z_{disp}, according to both numerics (see, e.g., [14, 15]) and analytical condition (16). It also follows from Eq. (18) that for an asymmetric dispersion map $L_1 \neq L_2$ the maximum possible value of $|d_0|$ grows as L_1 increases (for fixed L, Z_{nl}, d_1), in correspondence with Fig. 3 in [15].

Equation (15) also has a clear physical meaning in another limit $d_0/d_1 \gg L/Z_{nl}$, $Z_{disp} \gg L$, and $Z_{nl} \gg L$, in which Eq. (15) reduces to

$$(2d_0X_0 - Y_0)/Y_0 = O(L/Z_{disp}) \ll 1. \quad (19)$$

Equality $2d_0X_0 = Y_0$ exactly corresponds to the one-soliton solution of the NLS with dispersion d_0 (see [10]), where the dispersion d_0 and the nonlinearity continuously balance each other. Thus, in the limit $Z_{disp} \gg L$, which is called a weak dispersion limit, we recover the usual NLS describing the path-averaged (over the space period L) DM soliton dynamics, provided d_0 is large enough. A weak dispersion management limit was studied earlier [1, 16–18]. Note that an additional condition $d_0/d_1 \gg L/Z_{nl}$ allows the amplitude d_1 of the dispersion variation to be much higher still than d_0, because one assumes $L \ll Z_{nl}$.

To summarize, the necessary analytical condition (15) for the existence of the DM soliton is established. From the physical point of view, this condition means that the DM soliton solution can exist only if the nonlinearity is strong enough to compensate the pulse broadening due to the negative value of the average dispersion d_0. Note that estimates in Eqs. (16)–(19) are only given here for a physical interpretation of the analytical condition (15). So far, the DM soliton solution has been obtained numerically [3, 4, 14] and by the variational [5] and other perturbative approaches [19–21]. These results are in agreement with condition (15). But analytical proof of the existence of the DM soliton in the parameter region satisfying condition (15), i.e. the sufficient condition for existence, is still an open question.

The author thanks I.R. Gabitov for helpful discussions.

Support was provided by the US Department of Energy, under contract W-7405-ENG-36, RFBR and the program of the Russian Government Support for Leading Scientific Schools.

REFERENCES

1. V. E. Zakharov, in *Optical Solitons: Theoretical Challenges and Industrial Perspectives*, Ed. by V. E. Zakharov and S. Wabnitz (Springer-Verlag, Berlin, 1999), p. 73; V. E. Zakharov and S. V. Manakov, Pis'ma Zh. Éksp. Teor. Fiz. **70**, 573 (1999) [JETP Lett. **70**, 578 (1999)].
2. C. Lin, H. Kogelnik, and L. G. Cohen, Opt. Lett. **5**, 476 (1980).
3. M. Nakazawa and H. Kubota, Electron. Lett. **31**, 216 (1995).
4. N. J. Smith, F. M. Knox, N. J. Doran, *et al.*, Electron. Lett. **32**, 54 (1996).
5. I. Gabitov and S. K. Turitsyn, Opt. Lett. **21**, 327 (1996); Pis'ma Zh. Éksp. Teor. Fiz. **63**, 814 (1996) [JETP Lett. **63**, 861 (1996)].
6. S. Kumar and A. Hasegawa, Opt. Lett. **22**, 372 (1997).
7. P. V. Mamyshev and N. A. Mamysheva, Opt. Lett. **24**, 1454 (1999).
8. L. F. Mollenauer, P. V. Mamyshev, J. Gripp, *et al.*, Opt. Lett. **25**, 704 (2000).
9. J. H. B. Nijhof, N. J. Doran, W. Forysiak, and F. M. Knox, Electron. Lett. **33**, 1726 (1997).
10. V. E. Zakharov and A. B. Shabat, Zh. Éksp. Teor. Fiz. **61**, 118 (1971) [Sov. Phys. JETP **34**, 62 (1972)].
11. V. E. Zakharov, Zh. Éksp. Teor. Fiz. **62**, 1745 (1972) [Sov. Phys. JETP **35**, 908 (1972)].
12. P. M. Lushnikov, Pis'ma Zh. Éksp. Teor. Fiz. **62**, 447 (1995) [JETP Lett. **62**, 461 (1995)].
13. S. K. Turitsyn, J. H. B. Nijhof, V. K. Mezentsev, and N. J. Doran, Opt. Lett. **24**, 1871 (1999).
14. A. Berntson, N. J. Doran, W. Forysiak, and J. H. B. Nijhof, Opt. Lett. **23**, 900 (1998).
15. A. Berntson, D. Anderson, N. J. Doran, *et al.*, Electron. Lett. **34**, 2054 (1998).
16. A. Hasegawa and Y. Kodama, *Solitons in Optical Communications* (Oxford Univ. Press, New York, 1995).
17. Yu. L. Lvov and I. R. Gabitov, chao-dyn/9907007 (1999).
18. S. B. Medvedev and S. K. Turitsyn, Pis'ma Zh. Éksp. Teor. Fiz. **69**, 465 (1999) [JETP Lett. **69**, 499 (1999)].
19. S. K. Turitsyn and V. K. Mezentsev, Pis'ma Zh. Éksp. Teor. Fiz. **67**, 616 (1998) [JETP Lett. **67**, 640 (1998)]; S. K. Turitsyn, Phys. Rev. E **58**, 1256 (1998).
20. T. Lakoba and D. J. Kaup, Electron. Lett. **34**, 1124 (1998).
21. P. M. Lushnikov, Opt. Lett. **25**, 1144 (2000) (in press).

JETP Letters, Vol. 72, No. 3, 2000, pp. 115–118. Translated from Pis'ma v Zhurnal Éksperimental'noĭ i Teoreticheskoĭ Fiziki, Vol. 72, No. 3, 2000, pp. 168–172.

Subwavelength Focusing of Laser Radiation

V. S. Zuev* and A. V. Frantsesson**

** Lebedev Physical Institute, Russian Academy of Sciences, Leninskiĭ pr. 53, Moscow, 117924 Russia*

** e-mail: zuev@sci.lebedev.ru*

*** Institute of Radio Engineering and Electronics, Russian Academy of Sciences (Fryazino Branch), pl. Vvedenskogo 1, Fryazino, Moscow region, 141120 Russia*

Received December 23, 1999; in final form, June 23, 2000

Coaxial optical cone (bicone) is proposed to be used for additional subwavelength focusing of laser radiation. The transmission loss and the efficiency of bicone excitation are estimated. The bicone modes with a singularity in the vertex are experimentally excited by visible light. © *2000 MAIK "Nauka/Interperiodica".*

PACS numbers: 42.60.-v

It is beyond question, from both theoretical and practical points of view, that the lossless transmission of a microwave through a long line with cross section less or much less than the wavelength λ is feasible. This can be implemented with the use of a metallic coaxial line, double-wire line, etc. [1]. Moreover, it is known that the microwave radiation can be concentrated in a capacitor or induction coil in a volume with linear dimensions much less than λ. Devices with tapered cross section (conical coaxial lines), which, in fact, focus electromagnetic radiation onto a vanishingly small area, are also known. These are the so-called biconical horns, or bicones [2]. The bicones of various types are illustrated in the figure. They form two conical conducting surfaces with apex angles $2\theta_1$ and $2\theta_2$, respectively.

The bicone shape depends on the apex angles $2\theta_1$ and $2\theta_2$. In panel a of the figure, both θ_1 and $\theta_2 < \pi/2$. In panel b, $\theta_1 < \pi/2$ and $\theta_2 = \pi/2$. The device has the form of a conical tip normal to the plane. In panel c, $\theta_1 < \pi/2$ and $\theta_2 > \pi/2$, with $\theta_2 = \pi - \theta_1$. A bicone of this configuration serves as a standard model in studying linear antenna. In panels a–c, all cones are coaxial and their vertices coincide with each other. Two misaligned cones with coinciding vertices are shown in panel d. The apex angles of cones $2\theta_1$ and $2\theta_2$ (reckoned from the axes as shown in panel d) are identical, with $(\theta_1, \theta_2) < \pi/4$ and the angle between the respective symmetry axes being less than π. A bicone placed in the equatorial cut of a sphere is depicted in panel e. Such a bicone is discussed below when calculating the efficiency of bicone excitation by a plane wave.

The results of the microwave theory and the corresponding experiments cannot be directly extended to the optical range, because metal properties at optical frequencies differ appreciably from those in the microwave region. The dielectric constant ϵ of metals well reflecting at optical frequencies is $\epsilon = -|\epsilon'| + i\epsilon''$, with $|\epsilon'| \gg 1$ and $\epsilon'' \ll \epsilon'$, whereas, for microwaves, $\epsilon = i4\pi\sigma/\omega$, with $4\pi\sigma/\omega \gg 1$. However, it is shown below that the boundary optical problems can be solved by the method of successive approximations with the microwave solution taken as zero approximation. This becomes clear when considering the approximate Leontovich boundary condition [3, 4] for the tangential field components at the interface S between two media with $|\epsilon_1| \cong 1$ and $|\epsilon_2| \gg 1$:

$$\mathbf{E}_t = \sqrt{\mu/\epsilon}[\mathbf{H}_t, \mathbf{n}], \tag{1}$$

where n is the normal to the surface. For $\mu = 1$, $|\epsilon| \longrightarrow \infty$, and limited $\mathbf{H}_t$, one has $\mathbf{E}_t = 0$. Since $(i\omega/c)\mathbf{H} = \mathrm{curl}\,\mathbf{E}$ and $\mathbf{E}_t = 0$ at the interface S, it also follows that $\mathbf{H}_n = 0$ at S [4]. The conditions $\mathbf{E}_t = 0$ and $\mathbf{H}_n = 0$ coincide with the conditions in the problem for ideal conductors. Because of this, the known solutions for $\epsilon = i\epsilon'' = i4\pi\sigma/\omega \gg 1$ can be used as zero approximation in the case of a large complex ϵ.

We are interested in the bicone zero mode [2], which has a singularity at $r = 0$:

$$E_\theta = H_\varphi = \frac{A}{r\sin\theta}e^{-i\omega r/c}, \qquad E_r = E_\varphi = H_r = H_\varphi = 0. \tag{2}$$

For the wave converging to the bicone vertex, the field intensity grows in proportion to r^2 as the bicone vertex is approached. This means that the bicone provides additional focusing of the laser radiation directed at the bicone's large section. The question now arises as to the transmission loss and the efficiency of bicone excitation. These quantities are estimated below with the use of Leontovich boundary condition (1).

In the case of silver, one has for $\lambda = 550$ nm $\epsilon = -|\epsilon'| + i\epsilon'' = -12.7 + i0.46$ [5]; i.e., $|\epsilon| \cong 12.7 \gg 1$. Hence, the condition (1) for applicability is fulfilled, so that Eq. (2) can be used as zero approximation. In the second

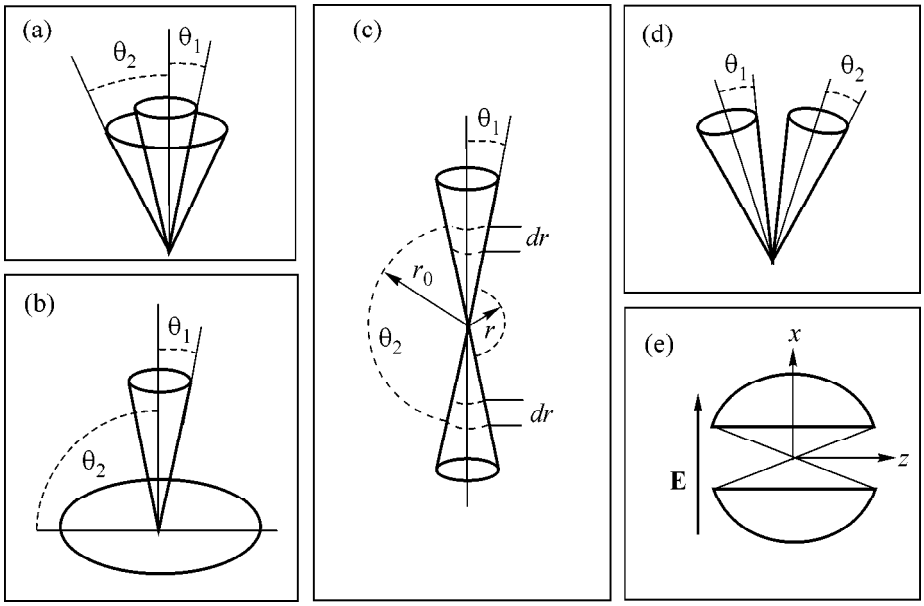

Various bicone types. In panel e, the gap in the equatorial cut is greatly exaggerated.

approximation, let us use Eq. (1) (now with the true ϵ value) to determine $\mathbf{E}_t$ and, next, the energy flux into the metal. The real part of this flux represents the loss for a converging TEM wave (2) propagating toward the bicone vertex.

The tangential (radial) field component near the surface of a nonideal cone in the bicone can be found from Eqs. (1) and (2):

$$E_r = \sqrt{1/\epsilon}H_\varphi = \left(\frac{\epsilon''}{2|\epsilon'|^{3/2}} - i|\epsilon'|^{-1/2}\right)H_\varphi. \quad (3)$$

It is sufficient to know the zero approximation for H_φ. As a result, one obtains that the real part of the Poynting's vector $\mathbf{P}$ in the direction of the normal to $\mathbf{S}$ is

$$\mathrm{Re}\mathbf{P} = \frac{c}{4\pi}\frac{\epsilon''}{2|\epsilon'|^{3/2}}H_\varphi^2(\theta = \theta_1, \theta_2). \quad (4)$$

The energy loss dN along the cone segments dr (figure, panel c) at a distance of r from the vertex is

$$dN = \frac{c}{2}\frac{\epsilon''}{2|\epsilon'|^{3/2}}[H_\varphi^2(\theta_1)\sin\theta_1 + H_\varphi^2(\theta_2)\sin\theta_2]rdr. \quad (5)$$

To obtain the absorption coefficient α, this loss should be divided by the energy flux N in the bicone:

$$N = \frac{c}{4\pi}\int[\mathbf{E}_\theta \cdot \mathbf{H}_\varphi]dS = \frac{cr^2}{2}\sin^2\theta_1 H_\varphi^2(\theta_1)\ln\left[\frac{\tan(\theta_2/2)}{\tan(\theta_1/2)}\right], \quad (6)$$

$$\alpha = \frac{1}{N}\frac{dN}{dr} = \frac{\epsilon''}{2|\epsilon'|^{3/2}} \times\left(\frac{1}{\sin\theta_1} + \frac{1}{\sin\theta_2}\right)\left[\frac{1}{\ln(\tan(\theta_2/2)/\tan(\theta_1/2))}\right]\frac{1}{r}. \quad (7)$$

Integrating Eq. (7), one finds a change in the total energy flux for a TEM wave propagating from the section at a distance r_0 from the vertex to the section at a distance $r < r_0$:

$$N = N_0 e^{\beta\ln(r/r_0)},$$
$$\beta = \frac{\epsilon''}{2|\epsilon'|^{3/2}}\frac{\sin^{-1}\theta_1 + \sin^{-1}\theta_2}{\ln(\tan(\theta_2/2)/\tan(\theta_1/2))}. \quad (8)$$

For a silver bicone with apex angles $\theta_1 = \pi/4$ and $\theta_2 = 3\pi/4$, one obtains $\beta = 8.2 \times 10^{-3}$. From Eq. (7) it follows that the radiation power of a converging wave propagating from $r_0 = 1$ μm to $r = 50$ nm decreases by 2.5%. As the section narrows, Eq. (1) becomes inapplicable because of the increased surface curvature [4].

Let us carry out calculations for a bicone made from semiconductor material with energy gap of about 1 eV (Si, Ge, and GaAs). For $\lambda = 10^{-4}$ cm and coefficient of absorption $\alpha = 10^5$ cm^{-1}, one has $\epsilon' = 10$ and $\epsilon'' = \alpha\lambda/2\pi = 1.5$. For a bicone of the same geometry as the silver bicone and for the same sections at $r_0 = 1$ μm and $r = 50$ nm, one finds that the attenuation is equal to 12%.

Let us now determine the portion of radiation power the wave incident on a bicone converts into the converging biconical wave. We will use the results of the Mie theory of light scattering from a sphere [6].

The incident linearly polarized wave $\mathbf{E} = \mathbf{a}_x E_0 \exp(-i\omega t + ik_z z)$ induces a current in a conducting sphere. If one makes a cut on the sphere across its equator perpendicular to the current (figure, panel e), then, on the one hand, a volume will arise where the bicone can be placed and, on the other hand, the pattern of light scattering from the sphere will not alter appreciably (an additional eigenmode will only arise in the sphere vibrations). A narrow gap in the cut will be closed by the displacement current. The cut-bounding surfaces should be conical, and the cone vertices should be close to each other, although not in contact. If the cone vertices contact each other, then the magnetic field will be too strong (which is beneficial to the magnetic interactions).

The current normal to the cut can be determined from the circulation $\oint_C \mathbf{H} \cdot d\mathbf{l} = 4\pi J/c$. The magnetic field of the scattered wave has the form (only the induced electric dipole is taken into account)

$$\mathbf{H}^{(s)} = -E_0 e^{-i\omega t} i\frac{3}{2} b_1^{(s)} \mathbf{m}_{o11}^{(3)},$$

$$m_{e11}^{(3)} = \mathbf{i}_\theta \frac{1}{\sin\theta} h_1^{(1)}(kR) P_1^1(\cos\theta)\sin\varphi \qquad (9)$$

$$- \mathbf{i}_\varphi h_1^{(1)}(kR) \frac{\partial P_1^1}{\partial\theta}\cos\varphi.$$

Here, $h_1^{(1)}(x)$ is the Bessel spherical function of the third order and $P_1^1(\cos\theta) = \sin\theta$ is the associated Legendre polynomial. The coordinate system chosen is noteworthy (figure, panel e). The z axis is directed along the wave vector $\mathbf{k} = \mathbf{a}_z k_z$ of the incident plane wave; the x axis is directed along $\mathbf{a}_x E_0$; the polar angle θ is reckoned from the z axis; and the azimuthal angle φ corresponds to the rotation about the z axis and is reckoned from the x axis.

We calculate the magnetic field circulation along the contour on the sphere in the $\theta = \pi/2$ plane. This corresponds to H_θ. We assume that $kR_a \approx 2\pi$. In this case, one has that approximately $h_1^{(1)}(x) \cong x^{-1}e^{ix}$ and

$$b_1^{(s)} \cong -e^{-i\varphi}\cos\rho\frac{\tan N\rho - N\tan\rho}{\tan N\rho + iN}, \qquad (10)$$

$$\rho = kR_a, \quad N = i|\epsilon'|^{1/2}.$$

For a metal, one has $\epsilon = -|\epsilon'| + i\epsilon''$ and $|\epsilon'| \gg |\epsilon''|$ for the optical frequencies; i.e., $\epsilon \cong -|\epsilon'|$. As a result, one obtains for $\rho = R_a\omega/c$

$$J_0 = \frac{3}{2} i\frac{c}{k} E_0 \frac{1 - i|\epsilon'|^{1/2}}{1 + |\epsilon'|}\cos\rho(1 - |\epsilon'|^{1/2}\tan\rho). \qquad (11)$$

At $|\epsilon'|^{1/2} \gg 1$, the function $\cos\rho(1 - |\epsilon'|^{1/2}\tan\rho)$ is maximum at $\rho_n = 2\pi n + (3\pi/2) + \Delta\rho$, where $\Delta\rho = |\epsilon'|^{-1/2}$. Expanding $\cos\rho_n$ and $\tan\rho_n$ in powers of $\Delta\rho$ near $\rho = \rho_n$, one has to an accuracy of $\Delta\rho$

$$|J_0| = \frac{3}{4}\frac{c}{k} E_0 \frac{|\epsilon'|^{1/2}}{(|\epsilon'| + 1)^{1/2}}. \qquad (12)$$

The charge amplitude $q_0 = \int J dt = (3c/4k\omega)E_0$. The field strength in the gap is

$$E = \frac{q_0}{s} = \frac{3}{4}\frac{c}{k\omega} E_0 \frac{1}{a^2} = \frac{3}{4}\frac{E_0}{(2\pi)^2}\left(\frac{\lambda}{a}\right)^2. \qquad (13)$$

In this expression, a is the size of the bicone vertex and $s = a^2$. For $\lambda = 1$ μm and $a = 50$ nm, the bicone field increases eightfold compared to the incident wave and the energy flux density increases 64-fold.

The numerical factor in Eq. (13) for E is rather small: 2×10^{-2}. The radiation incident on the bicone can be enhanced, without increasing the source power, by using a Fabry–Perot-type interferometer tuned to resonance, as is customary (although without referring to this device as the interferometer) in microwave experiments.

To check the effect of lossless optical wave concentration in the areas of dimensions $\ll\lambda$, we carried out experiments with a tungsten conical tip and a conducting plane, i.e., for the geometry shown in panel b of the figure. The radius of curvature of the tip vertex was 10–12 nm. The converging wave was excited by illuminating the tip vertex by a helium–neon laser at a wavelength of 633 nm in such a way that the radiation was polarized in the plane passing through the tip axis, while the laser beam was directed along the bisectrix of an angle between the generatrix of the conical tip surface and the plane, with the focus at the tip vertex. The converging wave was not detected, while the corresponding reflected diverging wave was clearly seen by the naked eye. A bright spot appeared at the tip vertex as the tip approached the plane at a distance of about tens of nanometers. The intensity of the diverging wave monotonically increased as the tip approached the plane at a distance of 7–3 nm, up to the contact with the plane.

Instrumental monitoring was accomplished by focusing the diverging wave with a lens onto a photodiode. The intensity of the diverging wave proved to be proportional to $\sin^{-2}\vartheta$, i.e., in accordance with Eq. (2), where k_z should be replaced by $-k_z$. In every point with different φ, the diverging wave was linearly polarized along the radius of the bicone cross section. This also corresponds to the wave configuration in Eq. (2). The preliminary results are published in our work [7].

In summary, the approximate Leontovich boundary conditions have been used to estimate losses for the zero mode of optical bicone at a 400-fold concentration of energy flux density in the cross section much smaller

than the wavelength. The losses are equal to 2.5% for a silver bicone at a wavelength of 550 nm and to 12% for a bicone made from a semiconductor with energy gap of 1 eV slightly smaller than the photon energy. The efficiency of bicone excitation has been estimated. It proved to be not very high. The methods for its sizable increase are suggested. The results obtained are helpful for near-field scanning optical microscopy and in the experiments on radiation concentration in the form of short high-power laser pulses. In these experiments, the bicone, of course, will be destroyed, but it will enhance the field intensity for several femtoseconds for practically any of the presently existing lasers with proper mode composition and radiation contrast.

This work was supported by the Russian Foundation for Basic Research.

REFERENCES

1. L. A. Vaĭnshteĭn, *Electromagnetic Waves* (Radio i Svyaz', Moscow, 1988).
2. S. A. Schelkunoff, *Electromagnetic Waves* (D. van Nostrand, New York, 1947).
3. M. A. Leontovich, in *Selected Works* (Nauka, Moscow, 1985), p. 352.
4. L. D. Landau and E. M. Lifshitz, *Course of Theoretical Physics*, Vol. 8: *Electrodynamics of Continuous Media* (Nauka, Moscow, 1982; Pergamon, New York, 1984).
5. H. Raether, *Surface Plasmons* (Springer-Verlag, Berlin, 1988).
6. J. A. Stratton, *Electromagnetic Theory* (McGraw-Hill, New York, 1941).
7. V. S. Zuev and A. V. Frantsesson, J. Russ. Laser Res. **19**, 465 (1998).

Translated by V. Sakun

JETP Letters, Vol. 72, No. 3, 2000, pp. 119–122. Translated from Pis'ma v Zhurnal Éksperimental'noĭ i Teoreticheskoĭ Fiziki, Vol. 72, No. 3, 2000, pp. 173–177.

Influence of Atomic Motion on the Shape of Two-Photon Resonance in Gas

A. V. Taĭchenachev*, A. M. Tumaĭkin, and V. I. Yudin

Novosibirsk State University, ul. Pirogova 2, Novosibirsk, 630090 Russia

** e-mail: llf@admin.nsu.ru*

Received June 19, 2000

A gas of three-level atoms with Λ configuration of energy levels was taken as an example to demonstrate that the influence of particle motion on the two-photon resonances extends further than the residual Doppler shift $(k_1 - k_2)v$. In particular, a narrow dip in the absorption spectrum ("dark" resonance) undergoes substantial narrowing, as compared to the atoms at rest. The width of this resonance is studied nonperturbatively as a function of the intensities of probe and strong fields. © *2000 MAIK "Nauka/Interperiodica"*.

PACS numbers: 42.50.Gy; 42.62.Fi

1. Two-photon resonance is one of the fundamental methods of nonlinear laser spectroscopy of gases [1]. It provides a way of obtaining Doppler-free resonances [2]. In some cases, e.g., when the system is excited via a real intermediate level, the width of resonance structures may be equal to the width of forbidden transition [3]. Two-photon resonances play an important role in some nonlinear quantum optics phenomena, such as coherent population trapping [4], electromagnetically induced transparency (EIT) [5], electromagnetically induced absorption (EIA) [6], inversionless amplification and lasing [7], light deceleration [8], and in some methods of laser cooling of atoms and ions [9].

It is well known that the two-quantum resonances are subject to Doppler broadening. This effect is ordinarily explained by the fact that the atomic velocity $\mathbf{v}$ appears in the two-photon resonance condition

$$\omega_{12} = (\omega_1 - \mathbf{k}_1\mathbf{v}) \pm (\omega_2 - \mathbf{k}_2\mathbf{v}), \qquad (1)$$

where ω_{12} is the frequency of atomic transition and ω_1, $\mathbf{k}_1$ and ω_2, $\mathbf{k}_2$ are, respectively, the laser frequencies and the corresponding wave vectors. The ± sign depends on the scheme chosen for the excitation of the resonance levels: it is "+" for the cascade scheme and "–" for the Λ- and V-schemes. As a result, the resonances for different velocities generally occur at different frequencies, leading to the broadening or even full disappearance of the resonance after averaging [10]. However, for the closely spaced frequencies ω_1 and ω_2 and collinear waves (counterpropagating in the cascade scheme and copropagating in the Λ- and V-schemes), this effect may become negligibly weak because of the smallness of the residual Doppler shift $(\omega_1 - \omega_2)v/c$. It is customarily thought that, under these conditions, the effect of atomic motion on the shape of nonlinear resonance in gases is insignificant.

It is the purpose of this work to demonstrate that the effect of particle motion on the two-photon resonances extends further than the above-mentioned residual Doppler shift. The point is that the detuning of laser fields from the appropriate one-photon transitions depends on the atomic velocity, which, as is known (cf. e.g., [10]), results in different shapes (because of the power broadening and nonlinear interference effects) and positions (because of the light-induced shift) of the two-photon resonance for atoms belonging to the different velocity groups. For this reason, the velocity-averaged resonance shape in gas may be sizably different from that in the case of homogeneous broadening, even if the residual Doppler shift is absent. For instance, in a gas of three-level Λ-atoms, the width of a two-photon resonance in the absorption spectrum of a probe field is $\sim V^2/k\bar{v}$ (V is the Rabi frequency and $\bar{v} = \sqrt{2k_BT/M}$ is the most probable velocity) instead of homogeneous $\sim V^2/\gamma$ (γ is the excited-state spontaneous decay rate). Thus, an appreciable "Doppler narrowing" of the two-photon resonance takes place. This result follows, in particular, from the analytical expression obtained in [11] for the susceptibility in a linear approximation in a probe field. Unfortunately, this important fact was not discussed in that paper.

In this work, three-level Λ-atoms are taken as an example to examine in detail the effect (different from the effect of residual Doppler shift) of atomic motion on the shape of two-photon resonance in gas. In doing so, we do not restrict ourselves to the linear approximation, as was done in [11], and analyze the resonance width as a function of field intensities. This will allow us to determine the limits of applicability of linear approximation.

2. Let us consider the resonance interaction of a gas of three-level atoms, whose energy levels form a closed

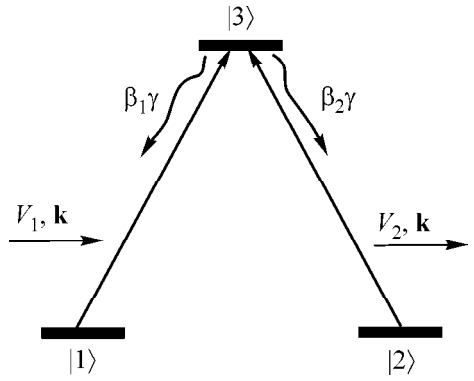

Fig. 1. Scheme of energy levels and radiative transitions of a three-level Λ-atom. The light-induced transitions are indicated by the solid lines. The wavy lines indicate the two possible spontaneous decay channels ($\beta_{1,2}\gamma$ are the corresponding rates).

Λ-system, with a bichromatic field of two copropagating traveling waves with amplitudes and frequencies E_1, ω_1 and E_2, ω_2 (Fig. 1). The two lower atomic states $|1\rangle$ and $|2\rangle$ belong to the ground nonrelaxing level, while the excited state $|3\rangle$ spontaneously decays with the rate γ. The branching ratios β_j (j = 1 and 2) determine the probabilities of the $3 \longrightarrow j$ transitions. For the closed Λ-system, $\beta_1 + \beta_2 = 1$. Let each of the fields excite only one arm of the Λ-system: E_1 excites the $1 \longrightarrow 3$ transition, and E_2 excites the $2 \longrightarrow 3$ transition. In the calculations, we will ignore the residual Doppler shift and assume that the wave vectors of both fields coincide: $\mathbf{k}_1 = \mathbf{k}_2 = \mathbf{k}$. In this case, the condition for two-photon resonance (1) is, clearly, fulfilled for all atomic velocities. Let, further, the time of interaction of atoms and field be long enough, so that the populations of atomic levels reach their steady-state values. For a spectroscopic signal, we choose the total absorption, which in an optically thin medium is proportional to the population n_3 of the excited state. The steady-state solution for the density matrix of a three-level atom moving with velocity $\mathbf{v}$ is well known (see, e.g., [12]). Applying the results of work [12] to the Λ-configuration of resonance levels and making allowance for the Doppler shift, the population of the excited level can be written as

$$n_3 = \frac{D}{A(kv)^2 + Bkv + C}, \tag{2}$$

where the denominator is a second-order polynomial in kv with real coefficients A, B, and C and complex conjugate roots. One can thus represent Eq. (2) as the sum of two Lorentzians

$$n_3 = \frac{iR}{X - kv} + \frac{-iR}{X^* - kv} \tag{3}$$

with real coefficient R. After this transformation, averaging with the Maxwell velocity distribution function is straightforward. The result can be expressed through the complementary error function of complex argument. Omitting tedious mathematics, we write the final result

$$\langle n_3 \rangle_v = \frac{\sqrt{\pi} V_1^2 V_2^2}{k\bar{v}(\beta_2 V_1^2 + \beta_1 V_2^2)} \frac{1}{\mathrm{Im}\{X\}} \times \mathrm{Re}\{\exp[-(X/k\bar{v})^2]\mathrm{Erfc}(-iX/k\bar{v})\}, \tag{4}$$

where

$$X = \frac{\delta_1 + \delta_2}{2} - \frac{\delta_1 - \delta_2}{2} \frac{\beta_2 V_1^2 - \beta_1 V_2^2}{\beta_2 V_1^2 + \beta_1 V_2^2} + \frac{\beta_2 V_1^4 - \beta_1 V_2^4}{(\delta_1 - \delta_2)(\beta_2 V_1^2 + \beta_1 V_2^2)} + i\frac{\gamma}{2}\left(1 + \frac{4V_1^2 V_2^2[2\beta_2^2 V_1^2 + 2\beta_1^2 V_2^2 + \beta_1\beta_2(\delta_1 - \delta_2)^2]}{\gamma^2(\beta_2 V_1^2 + \beta_1 V_2^2)^2} + \frac{4V_1^2 V_2^2[2\beta_2 V_1^4 + 2\beta_1 V_2^4 + (1 + 4\beta_1\beta_2)V_1^2 V_2^2]}{\gamma^2(\delta_1 - \delta_2)^2(\beta_2 V_1^2 + \beta_1 V_2^2)^2}\right)^{1/2}. \tag{5}$$

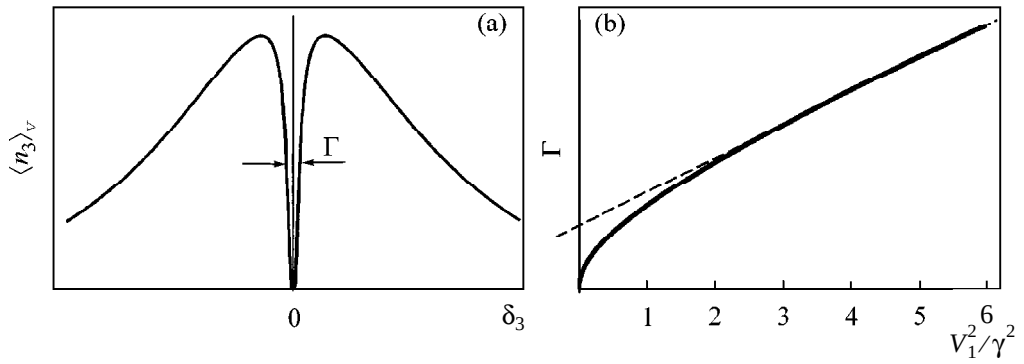

Fig. 2. (a) Typical dependence of the velocity-averaged excited-state population on the detuning of the probe field at the exact resonance with the strong field ($\delta_1 = 0$). (b) The width Γ of the dark resonance as a function of the intensity $\propto V_1^2$ of the strong field under the conditions of strong Doppler broadening $k\bar{v} = 60\gamma$ for the intensity of the probe wave $V_2^2/\gamma^2 = 0.001$.

In this expression, δ_j is the detuning of the jth wave from the one-photon $j \longrightarrow 3$ resonance ($j = 1$ and 2) and V_j are the corresponding Rabi frequencies, which, in general, can be taken to be real. Equation (4) describes the resonance structure (with respect to the $\delta_1 - \delta_2$ variable) with zero dip at $(\delta_1 - \delta_2) = 0$ corresponding to the dark or EIT resonance in gas.

Equation (4) can be used to analyze the behavior of dark resonance in different regimes, as regards the field detuning and intensity, and at an arbitrary ratio between the Doppler and homogeneous widths. Let us consider in more detail a typical situation where the Rabi frequency of the probe wave V_2 is much lower than both the Rabi frequency of the strong wave V_1 and the spontaneous decay rate γ. Our interest is in the shape of the resonance under the conditions of strong Doppler broadening $kv \gg \gamma$. Setting, for definiteness, $\beta_1 = \beta_2 = 1/2$, one obtains

$$X \approx \delta_2 + \frac{V_1^2}{\delta_1 - \delta_2} + i\frac{\gamma}{2}\sqrt{1 + \frac{16V_1^2V_2^2}{\gamma^2(\delta_1 - \delta_2)^2}}. \qquad (6)$$

If the frequency of the strong field is close to the frequency of the $1 \longrightarrow 3$ transition, then $\langle n_3 \rangle_v$ as a function of δ_2 appears as a broad absorption contour with the Doppler width $\sim 2k\overline{v}$ and a narrow dip in the center (Fig. 2). Let us now examine the dip width Γ as a function of intensity of the strong field, i.e., the power broadening effect. Equation (4) contains two frequency-dependent multipliers. The first one, $1/\mathrm{Im}\{X\}$, describes the resonance structure with width $\sim 2V_1V_2/\gamma$. The second one, $\sim \mathrm{Re}(\ldots)$, describes the structure with width $\sim 2V_1^2/k\overline{v}$. Therefore, there are two domains with different dependences of the width Γ of dark resonance (Fig. 2b) on the intensity $\propto V_1^2$ of the strong field. As V_1^2 increases, the root dependence $\sim\sqrt{V_1^2}$ transforms into the linear dependence $\sim 2V_1^2/k\overline{v} + Q$, as is clearly seen in Fig. 2b. The Q constant can be estimated by matching the root and the linear dependences. From the condition for the continuity of the function and its first derivative, one finds the matching point

$$V_1^2 = \frac{(k\overline{v})^2}{4\gamma^2}V_2^2$$

and the constant

$$Q \sim k\overline{v}V_2^2/2\gamma^2.$$

This gives the following estimate for the width of dark resonance at $V_1 \gg V_2$:

$$\Gamma \sim \begin{cases} 2V_1V_2/\gamma, & V_1 < (k\overline{v}/\gamma)V_2; \\ 2V_1^2/k\overline{v} + k\overline{v}V_2^2/(2\gamma^2), & V_1 > (k\overline{v}/\gamma)V_2. \end{cases} \qquad (7)$$

Note that for $V_1 < k\overline{v}$ one has $\Gamma \ll V_1^2/\gamma$, i.e., the Doppler narrowing of the nonlinear resonance.

Let us now discuss the applicability of the frequently used linear approximation for the probe field. It follows from [11] that this approximation provides the width $\sim 2V_1^2/k\overline{v}$ for the dark resonance. It is seen from Eq. (7) that this regime can only be realized for a very weak probe field:

$$V_2 \ll \frac{\gamma}{k\overline{v}}V_1. \qquad (8)$$

For instance, in rubidium vapor, $\gamma \sim 5$ MHz and $k\overline{v} \sim$ 300 MHz (room temperature). It then follows that the linear approximation is only valid if the intensity of the probe field is tens of thousands times lower than the intensity of the strong field.

It should be noted in conclusion that the influence of atomic motion on the shape of two-photon resonance is due to the fast atoms that are detuned far from the one-photon resonances. For a gas of Λ-atoms, this influence amounts to an appreciable Doppler narrowing of the nonlinear resonance. However, in the other excitation schemes, this effect may manifest itself as a new resonance structure. For example, for the four-level atom [13], a narrow dip of width $\sim V_1^2/k\overline{v}$ appears on the background of the resonant absorption with width $\sim V_1^2/\gamma$. These results will be discussed in our future publications.

REFERENCES

1. V. S. Letokhov and V. P. Chebotaev, in *Nonlinear Laser Spectroscopy of Ultrahigh Resolution* (Nauka, Moscow, 1990), Chaps. 4, 5.
2. L. S. Vasilenko, V. P. Chebotaev, and A. V. Shishaev, Pis'ma Zh. Éksp. Teor. Fiz. **12**, 161 (1970) [JETP Lett. **12**, 113 (1970)].
3. A. Akulshin, A. Celikov, and V. Velichansky, Opt. Commun. **84**, 139 (1991).
4. E. Arimondo, in *Progress in Optics*, Vol. 35: *Coherent Population Trapping*, Ed. by E. Wolf (North-Holland, Amsterdam, 1996), p. 259.
5. S. E. Harris, Phys. Today **50** (7), 36 (1997).
6. A. M. Akulshin, S. Barreiro, and A. Lezama, Phys. Rev. A **57**, 2996 (1998).

7. T. Ya. Popova and A. K. Popov, Zh. Prikl. Spektrosk. **12**, 734 (1970); O. Kocharovskaya, Phys. Rep. **219**, 175 (1992); M. O. Scully, Phys. Rep. **219**, 191 (1992).
8. L. V. Hau, S. E. Harris, Z. Dutton, and C. H. Behroozi, Nature **397**, 594 (1999); M. M. Kash, V. A. Sautenkov, A. S. Zibrov, *et al.*, Phys. Rev. Lett. **82**, 5229 (1999).
9. A. Aspect, E. Arimondo, *et al.*, Phys. Rev. Lett. **61**, 826 (1988); M. Kasevich and S. Chu, Phys. Rev. Lett. **69**, 1741 (1992); F. Deidrich, J. C. Bergquist, *et al.*, Phys. Rev. Lett. **62**, 403 (1989); C. Monroe, D. M. Meekhof, *et al.*, Phys. Rev. Lett. **75**, 4011 (1995); S. E. Hamann, D. L. Haycock, *et al.*, Phys. Rev. Lett. **80**, 4149 (1998).
10. S. G. Rautian, G. I. Smirnov, and A. M. Shalagin, *Nonlinear Resonances in the Spectra of Atoms and Molecules* (Nauka, Novosibirsk, 1979).
11. J. Gea-Banacloche, Y. Li, S. Jin, and M. Xiao, Phys. Rev. A **51**, 576 (1995).
12. P. L. Kelley, P. J. Harshman, *et al.*, J. Opt. Soc. Am. B **11**, 2298 (1994).
13. A. V. Taĭchenachev, A. M. Tumaĭkin, and V. I. Yudin, Pis'ma Zh. Éksp. Teor. Fiz. **69**, 776 (1999) [JETP Lett. **69**, 819 (1999)].

Translated by V. Sakun

JETP Letters, Vol. 72, No. 3, 2000, pp. 123–125. Translated from Pis'ma v Zhurnal Éksperimental'noĭ i Teoreticheskoĭ Fiziki, Vol. 72, No. 3, 2000, pp. 178–182.

Model of DX-like Impurity Centers in PbTe(Ga)

A. I. Belogorokhov*, B. A. Volkov, I. I. Ivanchik***, and D. R. Khokhlov*****

** State Research Institute for the Rare-Metals Industry, Moscow, 109017 Russia*

*** Lebedev Physical Institute, Russian Academy of Sciences, Leninskiĭ pr. 53, Moscow, 117924 Russia*

**** Physics Faculty, Moscow State University, Vorob'evy gory, Moscow, 119899 Russia,*
e-mail: khokhlov@mig.phys.msu.su

Received June 2, 2000; in final form, June 22, 2000

A new model is proposed for DX-like impurity centers, which are responsible for the Fermi-level stabilization and long-term relaxation effects in IV–VI semiconductors doped with group III elements. The model is based on the idea of a variable valence of the impurity, whereas the nature of the long-term effects at low temperatures is associated with the formation of an effective barrier caused by a change of two units in the impurity valence upon photoexcitation. The model is applied to an analysis of the photoconductivity spectra in PbTe(Ga). The model can also be applied to the classical DX centers in III–V semiconductors. © *2000 MAIK "Nauka/Interperiodica".*

PACS numbers: 71.23.An; 71.55.-i; 72.40.+w

1. Alloys based on lead chalcogenides are among the most promising materials for modern infrared optoelectronics because of the unusual effects arising in these semiconductors upon doping with group III elements (indium and gallium). Among these effects are, first of all, the stabilization of the Fermi level and the occurrence of long-term relaxation processes on disturbing the system from the equilibrium state at low temperatures. In PbTe(Ga) and also in some PbTe(Ga)-based alloys like $Pb_{1-x}Mn_xTe$(Ga) and $Pb_{1-x}Ge_xTe$(Ga), the Fermi level is stabilized in the upper half of the band gap, whereas the long-term effects (in particular, persistent photoconductivity) arise at temperatures below 80 K [1]. The photoconductivity relaxation kinetics in PbTe(Ga)-based alloys is rather nontrivial [2]. The photoresponse decay after switching off the background illumination consists of two stages corresponding to fast (~ 1–10 ms) and slow (10 ms–10^4 s, depending on the temperature) photoconductivity relaxation.

2. This work is devoted to an analysis of photoconductivity spectra in the fast region over the temperature range 45–150 K. At lower temperatures, the lifetime of nonequilibrium charge carriers strongly increases, and the fast part of the photoresponse becomes unobservable against the background of a high concentration of long-lived nonequilibrium electrons.

Photoconductivity spectra of PbTe(Ga) in the intrinsic absorption region measured at various temperatures are presented in Fig. 1. The spectra consist of a sharp peak at a frequency corresponding to the gap width of the material superimposed on the fundamental absorption band. The peak position shifts in frequency with temperature at a rate of $\partial E_p/\partial T \approx 0.4$ meV/K corresponding to the temperature coefficient of the PbTe forbidden band. The maximum of the peak amplitude is observed at a temperature of 75 K. The ratio between the peak amplitude and the amplitude of the fundamental absorption band varies from sample to sample but is virtually independent of the temperature. It should be particularly emphasized that impurity photoconductivity of any appreciable magnitude is not observed at a frequency corresponding to the thermal activation energy (~70 meV) of impurities.

A sharp dip is observed in the wave number range 3000–3500 cm^{-1} of the photoconductivity spectra. Its position depends neither on the sample nor on the temperature (Fig. 1). Most likely, the dip is due to the fact that the extent of evacuation of the cryostat chamber was insufficiently high so that the gas (supposedly, carbon dioxide) was frozen out at the sample surface.

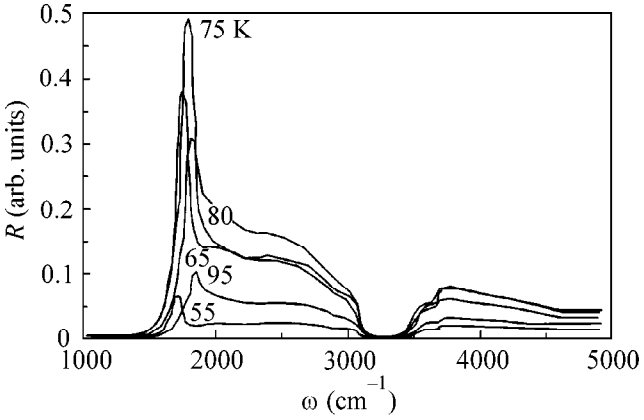

Fig. 1. PbTe(Ga) photoconductivity spectra in the intrinsic absorption region. Numbers on the curves indicate the sample temperatures in K.

0021-3640/00/7203-0123$20.00

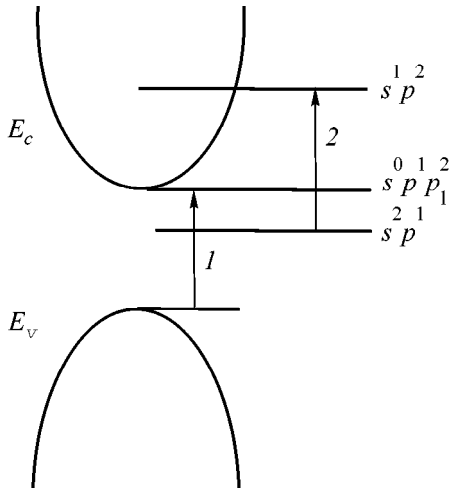

Fig. 2. Model of an impurity center in PbTe(Ga): (*1*) transitions responsible for photoresponse and (*2*) photoexcitation of the impurity ground state. The $s^0p^1p_l^2$ state corresponds to the localization of two *p* electrons with opposite spins in the potential of the empty *s* shell.

3. According to the current concepts, the effect of Fermi-level stabilization in lead telluride–based alloys doped with group III elements is due to the negative correlation energy of electrons localized on the impurity. This means that the ground state of an impurity center corresponds to either the empty center or the center occupied by two electrons, whereas the one-electron impurity state lies higher in energy [3, 4].

Until recently, the reason for the occurrence of long-term relaxation processes was associated with the rearrangement of the mutual positions of the impurity atom and its crystal environment upon ionization of each electron and with the formation of barriers in the configuration space between states of the system differing in the number of localized electrons. A similar model is also used for describing DX centers in III–V and II–VI semiconductors. At the same time, this conventional model runs into a number of fundamental difficulties in interpreting experimental data. In particular, both for classical DX centers in III–V semiconductors and for the DX-like centers in IV–VI semiconductors, thermal activation of nonequilibrium charge carriers is observed in the region of temperatures $T \ll W/k$, where k is the Boltzmann constant and W is the barrier height in the configuration space separating the localized and the band electron states, that is, in the quantum region. At the same time, a quasi-classical approach is commonly used in the calculation of configuration diagrams for the DX centers, which does not take into account energy quantization in the potential wells of the configuration diagrams. Simple estimates show that, because the characteristic barrier heights are comparable to the energy of an LO phonon, only a few quantum vibronic states can form in such a well and the quasi-classical approach becomes inapplicable. In such a situation, the overlap of wave functions of the states in neighboring quantum wells becomes significant; therefore, the effects of tunneling between these states must considerably decrease the characteristic lifetime of nonequilibrium carriers at low temperatures. Consequently, the long-term relaxation effects can hardly be observed.

In this work, a model is considered in which it is assumed that the barrier between the localized and band states, which leads to the occurrence of persistent photoconductivity and long-term relaxation processes, primarily forms through the electronic mechanism. The model is based on the fact that the relevant bands in lead chalcogenides are almost completely built from the atomic *p* orbitals. A gallium dopant atom substitutes for a lead atom in these materials. As indicated above, the effect of Fermi-level stabilization is caused by the negative electron correlation energy on the center. Consequently, the gallium atom charge state Ga^{2+}, which is neutral relative to the crystal lattice, is unstable and decomposes according to the reaction $2Ga^{2+} \longrightarrow Ga^{+} + Ga^{3+}$. Then the Fermi-level stabilization, e.g., relative to doping with other impurities, is provided by the redistribution of gallium atoms between the donor Ga^{3+} and acceptor Ga^{+} charge states.

In terms of atomic orbitals, the Ga^{2+}, Ga^{+}, and Ga^{3+} states correspond to the s^1p^2, s^2p^1, and s^0p^3 electronic configurations. The lead atom, which substitutes for gallium, has the s^2p^2 configuration. The relevant bands in lead chalcogenides are almost completely built from atomic *p* orbitals; therefore, for various charge states of the Ga atom, electrons occupying the deep *s* shell are localized and *p* electrons are delocalized.

The principal idea of our model is that the one-electron impurity state with only one electron in the *s* shell lies, within the one-electron approximation, energetically much higher than the two-electron ground state and higher than the bottom of the conduction band (Fig. 2). Then, for photoionization of the first electron from the impurity center, the necessary energy must be imparted to this electron, first, for its excitation to the conduction band and, second, for the transition of the impurity center to the state corresponding to one *s* electron localized on the impurity. This energy can significantly exceed the energy gap (transitions *2* in Fig. 2), which may cause the absence of impurity photoconductivity in the spectra. One *s* electron remaining on the impurity center rapidly passes to the conduction band, whose bottom is located energetically lower than the impurity center. Thus, two nonequilibrium electrons appear in the conduction band. The recombination processes are one-electron; however, in order for the electron to be captured by the impurity center, it must acquire energy equal to the distance between the quasi-Fermi level and the one-electron impurity state. Actually, it is this energy gap that determines the barrier preventing rapid recombination of electrons on the center.

However, the reasons for the occurrence of two stages of photoconductivity relaxation cannot be fully understood within the model outlined above. This contradiction can be resolved in the following way. The Fermi-level stabilization suggests that the *s* shell is empty in an appreciable number of gallium atoms. Two *p* electrons with opposite spins can be localized in the short-range attractive potential of this shell [5]. However, because of the high dielectric constant and the small effective mass of electrons in PbTe, a single impurity center with the empty *s* shell may not create a bound state. At the same time, the number of such centers is rather large, and one bound state of *p* electrons can form per large (up to 10^3–10^4) number of impurity centers with the empty *s* shell [6]. Then, fast photoconductivity relaxation in PbTe(Ga) can be caused by the localization of part of the photoexcited electrons in these bound states, which are energetically close to the bottom of the conduction band and are shallow in this sense. This model explains some features of photoconductivity kinetics in PbTe(Ga), e.g., the fact that the amplitude in the fast relaxation region is independent of the position of the quasi-Fermi level [7]. It should be noted that, in the case of classical DX centers in III–V semiconductors, an individual impurity always has a bound local hydrogen-like state. This feature represents one of the principal distinctions of classical DX and DX-like impurity centers.

In our opinion, the peak in the photoconductivity spectra is associated with electron transitions from the valence band to the shallow local states, whose density can significantly exceed the density of band states at the bottom of the conduction band (transitions *1* in Fig. 2). The shallow local states are genetically associated with the bottom of the conduction band; consequently, the spectrum of the corresponding photoresponse should have a resonance character. This also explains the "locking" of the peak in photoconductivity spectra to variations of the gap width upon varying the alloy temperature and composition [8].

Thus, the model under discussion provides an explanation for the basic features of the PbTe(Ga) photoconductivity spectra in the mid-IR range. Moreover, it allows one to interpret the occurrence of strong paramagnetism in PbTe(Ga) at temperatures of ~60 K under conditions of infrared background illumination [9] and some other effects that were not understood previously.

The difficulties of the model stem from the fact that Fermi-level stabilization and light-doping conditions cannot be accomplished simultaneously in IV–VI semiconductors when individual impurity centers may be considered as isolated ones. Because the number of growth defects, which are electroactive in the materials under consideration, comprises, as a rule, no less than 10^{18} cm^{-3}, the doping level should be at least no lower to provide Fermi-level stabilization. The impurity concentration indicated above corresponds to heavy doping; therefore, the interaction of impurity centers can be important in this case. In particular, there is some evidence that the centers providing Fermi-level stabilization in PbTe(Ga) are not isolated gallium atoms but complexes occupying certain crystallographic positions [10].

This work was partly supported by the Russian Foundation for Basic Research, project nos. 98-02-17317, 99-02-17531, and 99-02-16449.

REFERENCES

1. B. A. Akimov, A. V. Dmitriev, D. R. Khokhlov, *et al.*, Phys. Status Solidi A **137**, 9 (1993).
2. B. A. Akimov, A. V. Albul, and L. I. Ryabova, Fiz. Tekh. Poluprovodn. (St. Petersburg) **29**, 2158 (1995) [Semiconductors **29**, 1125 (1995)].
3. I. A. Drabkin and B. Ya. Moĭzhes, Fiz. Tekh. Poluprovodn. (Leningrad) **17**, 969 (1983) [Sov. Phys. Semicond. **17**, 611 (1983)].
4. D. R. Khokhlov and B. A. Volkov, in *Proceedings of the 23rd International Conference on Physics of Semiconductors, Berlin, 1996* (World Scientific, Singapore, 1996), Vol. 4, p. 2941.
5. B. A. Volkov and O. M. Ruchaĭskiĭ, Pis'ma Zh. Éksp. Teor. Fiz. **62**, 205 (1995) [JETP Lett. **62**, 217 (1995)].
6. A. I. Baz', Ya. B. Zel'dovich, and A. M. Perelomov, *Scattering, Reactions and Decays in Nonrelativistic Quantum Mechanics* (Nauka, Moscow, 1971, 2nd ed.; Israel Program for Scientific Translations, Jerusalem, 1966).
7. B. A. Akimov, N. B. Brandt, A. M. Gas'kov, *et al.*, Fiz. Tekh. Poluprovodn. (Leningrad) **17**, 87 (1983) [Sov. Phys. Semicond. **17**, 53 (1983)].
8. A. I. Belogorokhov, E. I. Slyn'ko, and D. R. Khokhlov, Pis'ma Zh. Tekh. Fiz. **18** (8), 30 (1992) [Sov. Tech. Phys. Lett. **18**, 252 (1992)].
9. A. N. Vasil'ev, T. N. Voloshok, B. A. Volkov, *et al.*, Pis'ma Zh. Éksp. Teor. Fiz. **61**, 768 (1995) [JETP Lett. **61**, 786 (1995)].
10. D. E. Dolzhenko, V. N. Demin, I. I. Ivanchik, *et al.*, Fiz. Tekh. Poluprovodn. (St. Petersburg) **34** (10), (2000) (in press) [Semiconductors **34** (10), (2000) (in press)].

Translated by A. Bagatur'yants

JETP Letters, Vol. 72, No. 3, 2000, pp. 126–130. Translated from Pis'ma v Zhurnal Éksperimental'noĭ i Teoreticheskoĭ Fiziki, Vol. 72, No. 3, 2000, pp. 183–189.

Phase Diagram of Strongly Correlated Fermi Systems

M. V. Zverev, V. A. Khodel, and M. Baldo*

Russian Research Centre Kurchatov Institute, pl. Kurchatova 1, Moscow, 123182 Russia

** Instituto Nazionale di Fisica Nucleare, 95129 Catania, Italy*

Received June 19, 2000

Phase transitions caused by the redistribution of quasiparticle occupation numbers $n(p)$ in homogeneous Fermi systems with particle repulsion are analyzed. The phase diagram of a strongly correlated Fermi system, when drawn in the coordinates "density ρ–dimensionless coupling constant η," resembles a Washington pie for a rather broad class of interactions. Its upper part is "filled" with Fermi condensate, and the bottom part is filled with normal Fermi liquid. Both parts are separated by a narrow interlayer of Lifshitz phase with a multiply connected Fermi surface. © *2000 MAIK "Nauka/Interperiodica".*

PACS numbers: 71.27.+a

The transformation of one-particle degrees of freedom at temperature $T = 0$ in strongly correlated Fermi systems has been studied over many years using the Landau approach, for which the energy E of a system is treated as a functional of the quasiparticle distribution function $n(\mathbf{p})$ [1–3]. It now becomes clear that the habitual Landau ground state of a homogeneous Fermi liquid with quasiparticle filling $n_F(p) = \theta(p_F - p)$ persists until the coupling constant g (only repulsive forces are considered in this work) exceeds the threshold value g_c, after which the necessary condition for its stability

$$\delta E(n(p)) = \int \xi(p)\delta n(p)\frac{d^3p}{(2\pi)^3} > 0, \qquad (1)$$

which requires that the increment in the total energy E be positive for any possible variation of the n_F distribution, breaks down. In Eq. (1), $\xi(p)$ is the quasiparticle energy measured from the chemical potential μ.

At first, one spoke about the Fermi sphere transformation with the appearance of the so-called Lifshitz bubbles ["icebergs," i.e., the domains in momentum space with quasiparticle filling $n(p) = 1$] separated from the "continent" with $n(p) = 1$ and from one another by narrow "straits" with $n(p) = 0$. And only several years ago, the nontrivial and smooth solutions of the variational equation

$$\delta F(n(p))/\delta n(p) = 0, \quad p_i < p < p_f, \qquad (2)$$

with $F = E - \mu N$, were found in the vicinity of the Fermi surface [4–6]. Inasmuch as $\delta F/\delta n(p)$ is nothing but $\xi(p)$, this equation implies that the dispersion in the spectrum of one-particle excitations is absent in the $[p_i, p_f]$ interval near the Fermi surface. A collection of quasiparticles with momenta from this interval is called the Fermi condensate (FC). The p_i and p_f values specify the boundaries of this interval and are also determined from variational condition (2). Something resembling FC is indeed observed in the spectra of strongly correlated electronic systems of exotic superconductors [7], thus stimulating interest in the phase diagram of strongly correlated systems. In this work, we analyze the general features of this diagram in the variables "density ρ–dimensionless coupling constant $\eta = g/g_c$." These variables are suitable because the normal Fermi liquid then fills the $0 < \eta < 1$ band. It is the purpose of this work to find out what part of the ($\rho > 0$, $\eta > 1$) quadrant is occupied by the Lifshitz phase with a multiply connected Fermi surface and where the FC "leads the dance."

To begin with, the realistic energy functional $E(n(\mathbf{p}))$ of the strongly correlated systems has a rather complicated form and can hardly be exactly constructed. Because of this, in many approaches, i.e., in the Ginzburg–Landau method, its properties are analyzed with the use of effective functionals. Such an approach prevails in the Fermi condensation problem. As a rule, one examines the functionals of the form

$$E(n(\mathbf{p})) = \sum_{\mathbf{p}} \varepsilon^0_{\mathbf{p}} n(\mathbf{p}) + \frac{g}{2}\sum_{\mathbf{p}_1,\mathbf{p}_2} V(\mathbf{p}_1 - \mathbf{p}_2)n(\mathbf{p}_1)n(\mathbf{p}_2), \qquad (3)$$

where the first term is, as usual, the kinetic energy of noninteracting particles; $\varepsilon^0_{\mathbf{p}} = p^2/2M$, where M is the particle mass; and the second term with the positive effective coupling constant g, in fact, simulates the sum of Fock's and correlation contributions to the total energy of the system. The variational equation (2) then takes the form

$$\phi(p) = g\int V(\mathbf{p} - \mathbf{p}_1)n(p_1)\frac{d^3p_1}{(2\pi)^3}, \quad p_i < p < p_f, \qquad (4)$$

where $\phi(p) = \mu - \varepsilon_p^0$. Note that, if p is taken as the coordinate and $n(p)$ as the density ρ, then Eq. (4) becomes the equilibrium equation for a system of particles with interaction potential $V(r)$ in the external electric (or gravitational) field.

Equation (4) is the Fredholm integral equation of the first kind and is an example of an inverse problem met with in various areas of physics. An important feature of many inverse problems is the presence of additional constraints. For example, in the problem of equilibrium, the solutions of Eq. (4) are constrained to be nonnegative in the domain of their definition. In the Fermi condensation problem, an additional requirement, $n(p) \le 1$, arises. Under these conditions, the boundary "points" n_B (in our case, bubble-type solutions) should be added to the solution of Eq. (4) to provide the local minimum for $E(n)$ at the boundaries of the functional space.

On the way to the solution of an inverse problem there is a "hidden" obstacle which is discussed in tens of review articles and books (see, e.g., [8–10]). The point is that the solution of Eq. (4) becomes unstable against small perturbations if one imposes the natural requirement that the kernel V and its partial derivative $\partial V/\partial p$ be continuous functions (only this type of potentials will be considered below) (see [9], p. 12). This instability, on account of which the inverse problems have come to be known as ill-posed, manifests itself even in attempting to solve Eq. (4) approximately by constructing inverse matrix V^{-1} on a grid. As the grid point spacing decreases, "noises" rapidly increase in the solution, so that it eventually oscillates chaotically and changes cardinally even upon small variation of the grid point spacing or any of the input parameters. The problems of this kind also emerge when the solution is sought on a certain class of polynomials. As their number increases, the oscillation amplitude also grows.

However, such an instability (note, parenthetically, that it is in no way related to the Pauli principle) gives no grounds to "bury" Eq. (4), and the Fermi condensation along with it, and claim, as was done in [11], that the analytical function V can give only the bubble phase at $\eta > 1$. First, if one ignores the Pauli principle, then no bubble solutions to the problem of minimizing Eq. (3) appear, while the smooth solutions (i.e., FC) do exist. Second, we, in fact, are seeking for the minimum of energy functional (3), so that, even if Eq. (4) has no solution in the strict classical meaning, one can often find smooth functions $0 < n_0(p) < 1$ such that, when inserted into the right-hand side of Eq. (4), approximately reproduce its left-hand side, but the energy $E(n_0)$ calculated for these functions proves to be lower than the energy $E(n_B)$ of any bubble-type solution. The situation is the same as with the positive $f(x) = x^2(2 + \sin(1/x^2))$ function that is continuous in the interval $[-1, 1]$ and everywhere except the point $x = 0$. Although there is no solution to the equation for minimum $f'(x) = 0$ at the point $x = 0$, the minimum of $f(x)$ occurs, nevertheless, in the origin of coordinates. Hence, one should not "make a fetish" of the minimization equation even for a simple single-variable problem, because a direct analysis of the values of the function of interest in the "suspect" points may be sufficient for achieving this objective.

As for the functional minimum, the necessity of comparing the energies of different phases is even more topical. In particular, such a comparison shows that for small $(g - g_c)$ values (i.e., in the domain adjacent to the instability point of a normal Fermi liquid) the minimum of Eq. (3) is most often achieved for the bubble solutions, with the number of bubbles increasing with $\eta = g/g_c$. A system with model interaction $V(q) = g/(q^2 + \kappa^2)$ is a typical example. The critical constant g_B corresponding to the appearance of the first bubble is calculated from the condition that the group velocity v_F turns to zero or, what is the same, the effective mass M^* turns to infinity. The standard formula for M^* [12] gives $\alpha_B = g_c M/(4\pi^2 p_F) = 1/\ln(p_F/\kappa)$. As η increases, every new bubble appears upon achieving the critical value $\eta_c^{(n)}$, where the necessary condition for the stability of the solution with a given number n of bubbles breaks down. For instance, it was found in [13] that $\eta^{(1)} \simeq 1.09$, $\eta^{(2)} \simeq 1.16$, and $\eta^{(3)} \simeq 1.2$ for the dimensionless parameter $a = \kappa/p_F = 0.07$.

A different situation occurs for the system with interaction potential $V(q) = g/\sqrt{q^2 + \kappa^2}$. A single-bubble solution obtained by minimizing Eq. (3) with allowance made for conservation of the number of particles (as was done in [11]) does not assure the energy minimum even if η is in a very small excess of unity. Indeed, let us use, as the starting point, the known Fermi-condensate solution existing at $\eta > 1$ for $\kappa = 0$ [6]:

$$n_{FC}(p) = \nu_0 \theta(p_f - p), \tag{5}$$

where $p_F = \xi^{1/3} p_F$, $\nu_0 = 1/\xi$, and $\xi = Mg/(6\pi^2)$. The FC energy

$$\frac{E_{FC}}{N} = \frac{9}{10}\frac{p_F^2}{M}\xi^{2/3} \tag{6}$$

is lower than both the energy of the normal Fermi liquid

$$\frac{E_n}{N} = \frac{3}{10}\frac{p_F^2}{M}(1 + 2\xi) \tag{7}$$

and the energy for the solution with a bubble

$$\begin{aligned}\frac{E_B}{N} &= \frac{3}{10Mp_F^3}(1 + 2\xi)(p_1^5 - p_2^5 + p_3^5) \\ &\quad - \frac{3\xi}{2Mp_F^3}(p_2^3 - p_1^3)(p_3^2 - p_2^2),\end{aligned} \tag{8}$$

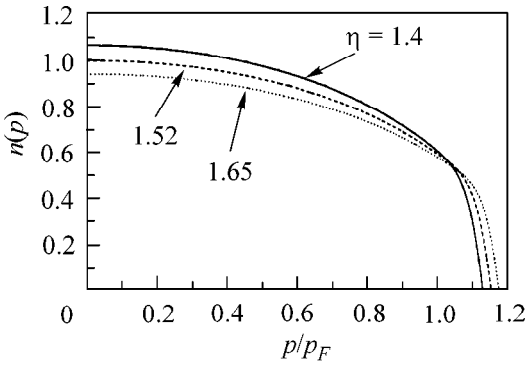

Fig. 1. Quasiparticle filling $n(p)$ calculated for $\kappa/p_F = 0.07$ and different values of the dimensionless constant $\eta = g/g_c$ in the model with interaction $V(q) = g/(q^2 + \kappa^2)$.

where p_1, p_2, and p_3 are the boundaries of the bubble solution. The absolute energy gain is on the order of $10^{-4}E_n$ and, hence, is small. However, the relative splitting $r_0 = |(E_B - E_{FC})/(E_n - E_{FC})|$ is much more important for the problem. It has quite a different order of magnitude. For instance, calculation gives for $\eta = 1.05$

$$p_1/p_F = 0.636, \quad p_2/p_F = 0.657, \quad p_3/p_F = 1.009, \quad r_0 = 0.22. \tag{9}$$

This 22% gap does not vanish even if the $\kappa < \kappa_c$ parameter is nonzero, when all derivatives $\partial^n V/\partial p^n$ are finite. Indeed,

$$\frac{\partial E}{\partial \kappa} \simeq -\frac{g\kappa}{2}\iint \frac{d^3p\,d^3p_1}{(2\pi)^6}\frac{n(p)n(p_1)}{((\mathbf{p}-\mathbf{p}_1)^2+\kappa^2)^{3/2}}. \tag{10}$$

When deriving this formula, we did not differentiate the positions $p_i(\alpha)$ of the bubble or the FC boundaries, because the corresponding contribution is proportional to the difference $(\varepsilon(p_i) - \mu)$ and, hence, turns to zero.

At small κ, the major term in Eq. (10) can be found by integration by parts, first over the angle between $\mathbf{p}$ and $\mathbf{p}'$, to yield

$$\frac{\partial E}{\partial \kappa} \sim -g\kappa\iint \frac{p\,dp\,p_1\,dp_1 n(p)n(p_1)}{\sqrt{(p-p_1)^2+\kappa^2}},$$

and then over the difference $(p - p_1)$. As a result, one gets $r(\kappa) = r_0 - \lambda\kappa^2\ln(1/\kappa)$, where

$$\lambda \sim \int (n_B^2(p) - n_{FC}^2(p))p^2dp. \tag{11}$$

Since $\lambda \sim (1 - \nu_0) \sim (\eta - 1)$, there is a broad range of κ values where the solution with $n(p) \neq 0$ or 1 lies energetically lower than a single-bubble solution. This qualitative conclusion is consistent with the results of a direct analytic calculation for both $\kappa = 0$ and nonzero κ values. We do not present here the corresponding cumbersome formulas and only note that for the dimensionless constant $\eta = 1.05$ the single-bubble solution is unstable up to $\kappa \sim 0.3p_F$. Moreover, up to $\kappa \sim 0.03p_F$, none of the admissible $n(p)$ variations satisfies the necessary condition for stability (1) of a single-bubble solution if p lies in the interval from zero to $p_{\max} > p_3$. In our forthcoming paper, we will clarify whether this implies that the single-bubble solution is completely modified for such κ values to form a Fermi condensate or the modification amounts to the appearance of a multiply connected solution with a κ-dependent number of bubbles. We merely note that, even a short distance from the straight line $\eta = 1$, single-bubble solutions are not the only ones that minimize functional (3) with analytical potential V.

Let us now turn to large η values, where a smooth solution to Eq. (4) satisfies the physical restraint $0 < n(p) < 1$, and first discuss an important technical issue: how should such solutions be sought for? For this purpose, various methods have been developed, which, in one way or another, are associated with the introduction of additional stabilizing functionals suppressing the "noises" and, hence, smoothing out the solution. For the detailed justification of these methods, see books [9, 10]. The following conclusion is essential to us: one can construct an approximate smooth solution $n_0(p)$ (it is sometimes called the quasi-solution) that reproduces the left-hand side of Eq. (4) with a prescribed accuracy, and this quasi-solution is unique ([9], ch. II).

One of the stabilizing functionals that is often used in equilibrium problems is constructed in the following way. Let us write $n = |\Psi|^2$ and, replacing $\mathbf{p}$ by $\mathbf{r}$ for clearness, add the "kinetic term" $|\nabla\Psi(\mathbf{r})|^2/2B$ to energy density (3). As a result, variational Eq. (4) transforms into the Schrödinger equation for the wave function of a system of interacting bosons moving in an external electric field between two spheres with as yet unknown radii. The solution of the Schrödinger equation is unique and continuous. Hence, the corresponding density distribution $\rho(r)$ is also unique and continuous and is practically independent of B at sufficiently large B values [9].

Another method of regularization, often even more suitable in applications, consists of the introduction of an additional local interaction of the form $Un^2(p)/2$ between the particles in Eq. (3), similar to the interparticle interaction in the Noziéres model [5]. The variational Eq. (4) then takes the form

$$\phi(p) = Un(p) + g\int V(\mathbf{p}-\mathbf{p}_1)n(p_1)\frac{d^3p_1}{(2\pi)^3}, \quad p_i < p < p_f. \tag{12}$$

This equation can be solved by the grid method ([9], p. 152). This is illustrated in Fig. 1 by several smooth solutions for a model system with interaction $V(q) = g/(q^2 + \kappa^2)$ and the same $\kappa = 0.07p_F$ as in calculations

[13]. The calculation is carried out for the smooth potential with $U/\varepsilon_F^0 = 10^{-3}$. One can see from Fig. 1 that the smooth solution of Eq. (12) exists for every η value. However, it satisfies the Pauli principle starting only at $\eta_{FC} \simeq 1.52$. Therefore, for all particles to find themselves in the FC, it would suffice to increase the coupling constant by a factor of one and a half compared to the value corresponding to the creation of the first Lifshitz bubble.

The fact that the Pauli principle becomes immaterial with an increase in η can be justified by a simple variational calculation. Let the distribution $n(p)$ be characterized by two parameters: the amplitude ν and the width p_f. For the potential $V(q) = g/(q^2 + \kappa^2)$ with $\kappa/p_F \ll 1$, the estimates of the kinetic τ and potential w energies per particle give $\tau \sim \nu p_f^5/M\rho \sim p_f^2/M$ and $w \sim g\rho/p_f^2$. In these estimates, it is taken into account that ν and p_F are related to each other by the normalization condition $\nu p_f^3 \sim \rho$ and the terms proportional to κ/p_F are ignored. Therefore, one must minimize the function

$$E(p_f)/N \sim p_f^2/M + g\rho/p_f^2, \qquad (13)$$

to obtain $p_f \sim (g\rho)^{1/4}$ and $\nu \sim g^{-3/4}\rho^{1/4}$. It then follows that (a) the occupation numbers for the quasiparticles in the strong coupling limit $g \longrightarrow \infty$ are small, so that the strongly correlated Fermi system behaves as a classical system, despite the fact that its excitation spectrum is completely degenerate and far from habitual, and (b) the dimensionless critical constant α_{FC} corresponding to the transition of all particles into the FC changes as $\rho^{1/3}$, allowing the density dependence of $\eta_{FC} = \alpha_{FC}/\alpha_B$ to be roughly estimated for this model: $\eta_{FC}(\rho) \sim |\ln\rho|$. The quality of this conclusion is illustrated in Fig. 2, where the phase diagram is drawn in the ln ρ, η variables.

Note that high density corresponds to a small κ/p_F ratio. In this limit, the slope of potential V (decreasing following the power or exponential law) is operative in the integral in Eq. (3). One can readily verify after calculating the kinetic and potential energies by the method similar to that used in deriving Eq. (13) that in both cases the amplitude ν of quasiparticle distribution decreases with increasing g and, starting at the critical value η_{FC}, the Pauli principle becomes immaterial, because all quasiparticles prove to be in the FC. Therefore, at high densities, the upper part of the (ρ, η) quadrant belongs to the FC for a rather broad class of interactions.

It should be stressed once again that the relationship $\xi(p) = 0$ is exactly fulfilled for neither of the smooth numerical solutions of Eq. (4) at any η value in this domain of the (ρ, η) plane. Therefore, in accordance with Eq. (1), one may reduce the total energy by increasing or decreasing the solution amplitude at every point, i.e., by adding the noises. However, for another numerical solution that is obtained, say, with the use of a different regularization procedure or by the same procedure but in a somewhat different computational scheme, the smooth components will be close to one another, whereas the system of energy-lowering noises will be cardinally different. It is then clear that the solutions with a finite number of bubbles are inadequate for the problem at $\eta > \eta_{FC}$. Under these conditions, only the smooth solutions have physical meaning, while the noises, in the realistic statement of the problem, are reduced either by introducing a finite temperature and fluctuations of the input parameters or as a result of the pairing or any other phase transition necessarily accompanying the Fermi condensation.

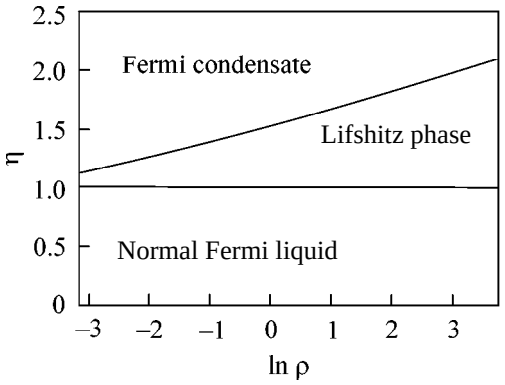

Fig. 2. Phase diagram in the ln ρ, η coordinates for the model with interaction $V(q) = g/(q^2 + \kappa^2)$.

This work was supported in part by the Russian Foundation for Basic Research (project no. 00-15-96590), the NSF (grant no. 9900713), and the McDonnel Center for Space Sciences. We are grateful to N.E. Zeĭn, S.V. Tolokonnikov, V.N. Éfros, and V.R. Shaginyan for discussions. V.A.Kh. thanks Washington University (Saint Louis, USA) and Prof. J.W. Clark for a warm reception. M.V.Z. acknowledges the INFN (Sezione di Catania, Italia) for hospitality.

REFERENCES

1. I. M. Lifshitz, Zh. Éksp. Teor. Fiz. **38**, 1569 (1960) [Sov. Phys. JETP **11**, 1130 (1960)].
2. M. de Llano and J. P. Vary, Phys. Rev. C **19**, 1083 (1979).
3. M. de Llano, A. Plastino, and J. G. Zabolitsky, Phys. Rev. C **20**, 2418 (1979).
4. V. A. Khodel and V. R. Shaginyan, Pis'ma Zh. Éksp. Teor. Fiz. **51**, 488 (1990) [JETP Lett. **51**, 553 (1990)].
5. P. Noziéres, J. Phys. I **2**, 443 (1992).
6. V. A. Khodel, V. R. Shaginyan, and V. V. Khodel, Phys. Rep. **249**, 1 (1994).
7. Z.-X. Shen and D. S. Dessau, Phys. Rep. **253**, 1 (1995).

8. S. G. Mikhlin, *Variational Methods in Mathematical Physics* (Gostekhizdat, Moscow, 1957; Pergamon, Oxford, 1964).

9. A. N. Tikhonov and V. Ya. Arsenin, *Methods for Solving Ill-Posed Problems* (Nauka, Moscow, 1974; Halsted, New York, 1977).

10. W. H. Press, S. A. Teukolsky, W. T. Vettering, and B. P. Flannery, *Numerical Recipes in C* (Cambridge Univ. Press, Cambridge, 1988).

11. S. A. Artamonov, Yu. G. Pogorelov, and V. R. Shaginyan, Pis'ma Zh. Éksp. Teor. Fiz. **68**, 897 (1998) [JETP Lett. **68**, 942 (1998)].

12. A. A. Abrikosov, L. P. Gor'kov, and I. E. Dzyaloshinskiĭ, *Methods of Quantum Field Theory in Statistical Physics* (Fizmatgiz, Moscow, 1962; Prentice-Hall, Englewood Cliffs, 1963).

13. M. V. Zverev and M. Baldo, Zh. Éksp. Teor. Fiz. **120**, 1200 (1998) [JETP **87**, 1129 (1998)].

Translated by V. Sakun

JETP Letters, Vol. 72, No. 3, 2000, pp. 131–133. Translated from Pis'ma v Zhurnal Éksperimental'noĭ i Teoreticheskoĭ Fiziki, Vol. 72, No. 3, 2000, pp. 190–194.

Effects of Low-Energy Ion Beam Action on Ge/Si Heteroepitaxy from Molecular Beam

A. V. Dvurechenskiĭ, V. A. Zinovyev, V. A. Kudryavtsev, and Zh. V. Smagina

Institute of Semiconductor Physics, Siberian Division, Russian Academy of Sciences, pr. akademika Lavrent'eva 13, Novosibirsk, 630090 Russia, dvurech@isp.nsc.ru

Received June 26, 2000

The evolution of the surface morphology of a pseudomorphic Ge film on Si upon irradiation with its own low-energy (230 eV) ions during heteroepitaxy from molecular beam has been studied experimentally by reflection high-energy electron diffraction. It has been found that irradiation with a continuous ion beam leads to a decrease in the critical Ge film thickness at which a transition from two-dimensional layer-by-layer to three-dimensional growth takes place. Exposure to pulsed ion irradiation (0.5 s) at instants of time that correspond to a fractional surface coverage more than 0.5 enhances the reflection intensity, which corresponds to a decrease in the roughness of the growth surface. © *2000 MAIK "Nauka/Interperiodica".*

PACS numbers: 61.80.Jh; 68.55.Jk; 61.14.Hg

The idea of using morphological evolution of the surface during the growth of mismatched heteroepitaxial systems proves to be very fruitful in developing a new approach to manufacturing nanostructures with quantum dots [1–3]. The morphological evolution is controlled by mechanical stresses in the growing film. As a result, the flat front of epitaxial growth is retained up to a certain critical film thickness, after which the front becomes similar to the relief of a plane with pyramids arranged on it. The relaxation of elastic deformations occurs at the vertices of the pyramids. Control of the formation of pyramids (size, shape, and density) is primarily based on numerous results of studying heteroepitaxy as a function of the substrate temperature and the molecular flux. Exposure to particles whose energy is sufficiently high compared to the energy of particles in the molecular beam but is insufficient for the generation of defects in the bulk of the epitaxial film (and the substrate) may provide an independent possibility of controlling the epitaxy process. The energy of particles in the molecular beam is determined by the characteristic temperature of the source of the particles. Its value does not exceed 0.1 eV. The use of hyperthermal particles (energy 100 eV) in film deposition led to strong changes in the growth kinetics and resulting physical properties of films of various materials, including elemental semiconductors (see, e.g., [4, 5]), compound semiconductors (see, e.g., [6]), and metals (see, e.g., [7]). In this case, some physical effects are observed, such as lowering of the epitaxy temperature and a decrease in the depth of the growing surface relief.

The aim of this work is to study the morphological evolution of the surface of a pseudomorphic Ge film on Si upon irradiation with low-energy ions during heteroepitaxy from molecular beam.

The experiments were carried out in an ultrahigh-vacuum chamber with a residual gas pressure of $<10^{-8}$ Pa. Germanium films were deposited from a crucible (boron nitride) on a silicon substrate. The Si wafers were of (111) orientation within 0.15° according to X-ray diffraction data. The germanium flux density was varied in the range 10^{12}–10^{15} cm^{-2} s^{-1} by varying the crucible temperature. A system for ionizing germanium and accelerating germanium ions was positioned above the crucible. The molecular beam of Ge was ionized by a transversal electron beam. The degree of ionization of the molecular beam of Ge in the system depended on the source design and was 0.1 and 0.5%. A pulsed accelerating voltage supply unit generated ion current pulses with a duration of 0.1–1 s. The energy of the Ge^+ ions was varied over the range 50–270 eV. The angle of incidence of the molecular and ion beams on the substrate was 54.5°.

The reflection high-energy electron diffraction technique was used, and reflection intensity oscillations were measured during layer-by-layer film growth. Irradiation was carried out by both pulsed and continuous low-energy ion beams. The growing germanium surface was exposed to a pulsed ion beam at various stages of growth (film thickness and the degree of surface layer filling). The experiments were carried out in the temperature range from 250 to 550°C.

Reflection high-energy electron diffraction intensity oscillations were observed during germanium deposition on the Si(111) surface by molecular-beam epitaxy (see Figs. 1, 2, curves *1*). The period of the oscillations equals the deposition time of one diatomic layer (bilayer; 1 bl = 1.56×10^{15} atom/cm^2). After the deposition of several diatomic layers, quenching of the oscillations was observed, which was due to the transi-

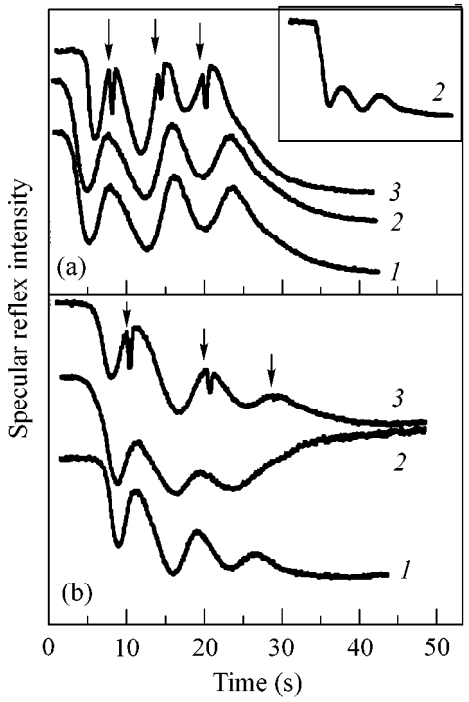

Fig. 1. Variation of the reflection high-energy electron diffraction intensity during (*1*) Ge/Si(111) heteroepitaxy from molecular beam and under simultaneous exposure to a (*2*) continuous or (*3*) pulsed beam of low-energy ions for substrate temperatures of (a) 350°C and (b) 250°C. The deposition rate $F \simeq 0.15$ bl/s; the degree of ionization, 0.1%; the energy of Ge^+ ions in the beam, 230 eV; and the duration of ion current pulses, 0.5 s. The instants of ion pulses are marked with arrows. Inset: the degree of ionization, 0.5%.

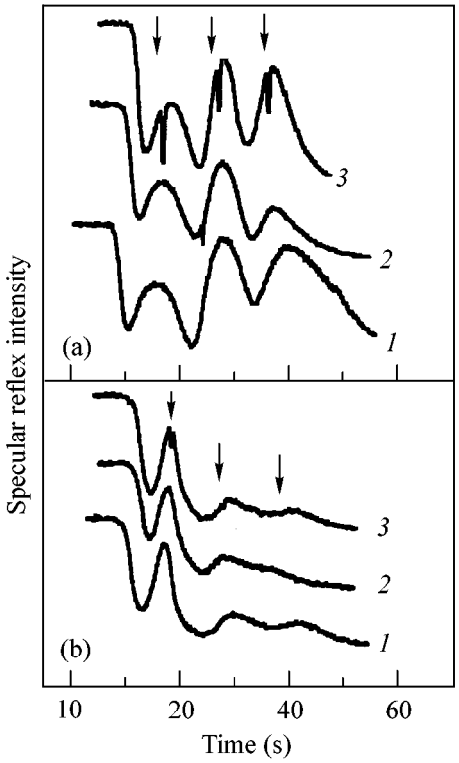

Fig. 2. The same as in Fig. 1 for a smaller Ge flux $F \simeq 0.1$ bl/s. The substrate temperature was (a) 350°C and (b) 250°C.

tion from a two-dimensional layer-by-layer to three-dimensional (2D–3D) growth mechanism for Ge islands as the film attained a critical thickness. Three oscillations were observed in the temperature range 250–400°C, and two oscillations of the reflection high-energy electron diffraction signal were observed in the range 450–550°C. The 2D–3D transition observed under our experimental conditions corresponds to the data reported in the literature on Ge/Si(111) heteroepitaxy from molecular beam [8–10].

On switching on the ionization system and applying the accelerating voltage, we obtained the following results for a flux of 0.15 bl/s and a degree of ionization of 0.1%.

Irradiation with a continuous ion beam at a temperature of 250°C led to a decrease in the number of reflection high-energy electron diffraction oscillations (Fig. 1b, curve *2*) compared to the number of oscillations for conventional epitaxy and also for epitaxy under conditions of exposure to a pulsed ion beam.

Irradiation with a continuous ion beam in the temperature range 300–350°C, compared to molecular-beam epitaxy, did not lead to appreciable changes in the process of heteroepitaxial growth. Exposure to a pulsed beam before each oscillation maximum caused an increase in the reflection high-energy electron diffraction intensity. It is natural to associate this behavior with smoothing of the growing-surface relief (Fig. 1a, curve *3*).

The effect of a decrease in the number of oscillations upon irradiation by a continuous beam of low-energy ions was also observed at a temperature of 350°C (see Fig. 1a, inset) under experimental conditions corresponding to a higher ion current density (degree of ionization 0.5%). In this case, two oscillations were observed, whereas three oscillations were observed for molecular-beam epitaxy.

We performed experiments at lower deposition rates (<0.15 bl/s), which corresponded to a smaller deviation from equilibrium in the growth process. Here, the effect of an increase in the reflection high-energy electron diffraction intensity upon exposure to a pulsed ion beam (Fig. 2a, curve *3*) and the effect of an increase in the number of growth oscillations upon exposure to a continuous ion beam (Fig. 2b, curve *2*) were also observed.

The interaction of accelerated particles with a solid surface gives rise to some phenomena which should be analyzed in order to understand the mechanisms that can make a contribution to the effects of a change in the number of oscillations and their intensity upon exposure to a beam of low-energy ions in various tempera-

ture ranges of Ge heteroepitaxy on Si. Among these are the following phenomena:

(1) sputtering of the material, which corresponds to an effective decrease in the flux of atoms incident on the surface during molecular-beam deposition;

(2) heating of the surface layer due to the released energy of the accelerated particles;

(3) change in the kinetics of island nucleation and decay on the Ge surface due to generation of adatoms and surface vacancy clusters;

(4) ion-stimulated superstructure phase transition caused by the release of energy by the accelerated particles.

The role of the first two factors was analyzed in our works [11–13] on Si homoepitaxy, where the conclusion was drawn that the processes associated with these factors make no significant contribution to the evolution of surface morphology during the growth process. This conclusion retains its validity for Ge heteroepitaxy grown from ion-molecular beams, because close energies and integral ion fluxes were used under our conditions.

The change in the number of reflection high-energy electron diffraction intensity oscillations upon exposure to a continuous ion beam, compared to conditions of conventional growth from molecular beams, can be interpreted as a change in the critical film thickness (h_c) for the 2D–3D transition. The reduction in the number of oscillations corresponds to a decrease in h_c during heteroepitaxy with simultaneous irradiation by a continuous ion beam. Here, the ion-stimulated nucleation of three-dimensional Ge islands on the growing layer surface is apparently the predominant mechanism of surface morphology evolution. This nucleation provides relaxation of elastic deformations in the Ge/Si system [14]. This mechanism can lead to the observed decrease in h_c.

Carrying out heteroepitaxy at higher substrate temperatures while retaining the flux parameters is favorable to annealing of the nucleation centers of three-dimensional Ge islands generated by irradiation and, hence, to a decrease in their contribution to the change in the growth kinetics. This apparently explains the virtually identical behavior of the reflection high-energy electron diffraction intensity during molecular-beam epitaxy and epitaxy from a continuous ion-molecular beam with a degree of ionization of 0.1% (Fig. 1a). An increase in the ion current density (for a degree of ionization of 0.5%) leads to an increase in the generation rate of nucleation centers. Therefore, it is natural to expect that a change in the growth kinetics will occur at substrate temperatures for which the effects of ion action were not manifested at a degree of ionization of 0.1%. It is this result which is demonstrated in the inset in Fig. 1.

Under conditions of pulsed irradiation, the integral ion flux over the time of pseudomorphic film growth is ~20 times smaller than for irradiation with a continuous beam. The observed effect of an increase in the reflection high-energy electron diffraction intensity upon exposure to a pulsed ion beam (Fig. 1a, curve *3*) during Ge heteroepitaxy on Si indicates that the surface density of electron scattering sites (island boundaries and vacancy clusters) decreases.

A reduction in the growing layer roughness upon exposure to a pulsed beam of Ge^+ ions with an energy of about 200 eV before the maximum of a growth oscillation is likely associated with an increase in the diffusion coefficient of adatoms due to an ion-stimulated reconstruction of the Ge(111) surface, namely, a transition from the (7×7) to the (5×5) superstructure. We observed a superstructure phase transition induced by exposure to a pulsed ion beam during Si(111) homoepitaxy. The observed $(5 \times 5) \longrightarrow (7 \times 7)$ transition led to a decrease in the activation energy of the surface diffusion of atoms and to a reduction in the roughness of the growing surface upon exposure to a pulsed beam of low-energy ions [12, 13]. This effect was maximum when the exposure to a pulsed beam was carried out at the degree of layer filling 0.8.

This work was supported by the Russian Foundation for Basic Research, project no. 99-02-17196 and the program “Surface Atomic Structures,” project no. 4.2.99.

REFERENCES

1. N. N. Ledentsov, V. M. Ustinov, V. A. Shchukin, *et al.*, Fiz. Tekh. Poluprovodn. (St. Petersburg) **32**, 385 (1998) [Semiconductors **32**, 343 (1998)].
2. A. V. Dvurechenskiĭ and A. I. Yakimov, Izv. Vyssh. Uchebn. Zaved., Mater. Élektron. Tekh. **4**, 4 (1999).
3. O. P. Pchelyakov, Yu. B. Bolkhovityanov, A. V. Dvurechenskiĭ, *et al.*, Thin Solid Films **367**, 75 (2000).
4. J. W. Rabalais, A. H. Al-Bayati, K. J. Boyd, *et al.*, Phys. Rev. B **53**, 10781 (1996).
5. N. E. Lee, G. A. Tomash, and J. E. Greene, Appl. Phys. Lett. **65**, 3236 (1994).
6. S. W. Park, J. Y. Shim, and H. K. Baik, J. Appl. Phys. **78**, 5993 (1995).
7. G. Rosenfeld, R. Servaty, C. Teichert, *et al.*, Phys. Rev. Lett. **71**, 895 (1993).
8. O. P. Pchelyakov, V. A. Markov, A. I. Nikiforov, *et al.*, Thin Solid Films **306**, 299 (1997).
9. B. Voigtlander and A. Zinner, Appl. Phys. Lett. **63**, 3055 (1993).
10. U. Kohler, O. Jusko, G. Pietsch, *et al.*, Surf. Sci. **248**, 321 (1991).
11. A. V. Dvurechenskiĭ, V. A. Zinov’ev, V. A. Markov, *et al.*, Pis’ma Zh. Éksp. Teor. Fiz. **64**, 689 (1996) [JETP Lett. **64**, 742 (1996)].
12. A. V. Dvurechenskiĭ, V. A. Zinovyev, V. A. Markov, and V. A. Kudryavtsev, Surf. Sci. **425**, 185 (1999).
13. A. V. Dvurechenskiĭ, V. A. Zinov’ev, and V. A. Markov, Zh. Éksp. Teor. Fiz. **114**, 2055 (1998) [JETP **87**, 1116 (1998)].
14. A. A. Shklyev, M. Shibata, and M. Ichikawa, Thin Solid Films **343**/**344**, 532 (1999).

Translated by A. Bagatur’yants

JETP Letters, Vol. 72, No. 3, 2000, pp. 134–137. Translated from Pis'ma v Zhurnal Éksperimental'noĭ i Teoreticheskoĭ Fiziki, Vol. 72, No. 3, 2000, pp. 195–200.

Spin Orientation of Two-Dimensional Electrons in Electric Field

L. I. Magarill and M. V. Entin

Institute of Semiconductor Physics, Siberian Division, Russian Academy of Sciences, pr. akademika Lavrent'eva 13, Novosibirsk, 630090 Russia

Received June 20, 2000

The Rashba Hamiltonian is used to analyze the spin orientation of two-dimensional electrons in electric field. The mean electron spin is found to be oriented in the sample plane perpendicularly to the electric field. In the limit of weak spin–orbit interaction, the spin orientation factor may increase. © *2000 MAIK "Nauka/Interperiodica".*

PACS numbers: 73.50.-h

In recent years, considerable attention has been given to the spin effects in low-dimensional systems. This is primarily caused by the potential use of spin degrees of freedom in qubit design. When using spin degrees of freedom in semiconductor devices, it is desirable to control electron spins electrically, because other methods (magnetic or optical) do not provide local action and, hence, are incapable of selectively acting on relatively small-sized modern semiconductor devices. Moreover, the magnetic field should be high enough to induce considerable electron redistribution over the spin states, but it is impossible to rapidly vary such a field. As a result, the device becomes sluggish.

In this work, the rise of a mean spin density **S** in a 2D system under the action of in-plane electric field **E** is considered. The system is described by the following phenomenological equation:

$$\mathbf{S} = \gamma[\mathbf{n}\times\mathbf{E}]. \tag{1}$$

where **n** is the normal to the surface and γ is the spin orientation factor. For the effect to exist, the **n** and –**n** directions should be nonequivalent (the so-called oriented surface). This may be caused by both asymmetry of the quantum well and nonequivalence of the **n** and –**n** directions in the original crystal.

We will operate within the framework of the Rashba Hamiltonian [1], which includes the spin–orbit interaction of 2D electrons at the oriented surface:

$$\hat{\mathcal{H}}_0 = \mathbf{p}^2/2m + \mathcal{H}_{so}, \quad \mathcal{H}_{so} = \alpha(\boldsymbol{\sigma}[\mathbf{p}\times\mathbf{n}]). \tag{2}$$

In Eq. (2), **p** is the electron 2D momentum, α is the spin–orbit coupling constant, and σ_i are the Pauli spin matrices. From here on, $\hbar = 1$.

The energy spectrum of Hamiltonian (2) is

$$E_\mu(p) = p^2/2m + \mu|\alpha|p, \tag{3}$$

where $\mu = \pm 1$ corresponds to two different spin components of the spectrum of 2D electron gas. The splitting is ordinarily small and is only ~10^{-3} of the Fermi energy.

By using Kubo formalism [2] for the response of mean spin density **S** to the lateral electric field, one can write

$$\begin{aligned} S_i &= \gamma_{ij}E_j, \\ \gamma_{ij} &= \frac{-e}{A}\int_0^\infty dt e^{-\delta t} \\ &\times \int_0^{1/T} d\lambda \langle \mathrm{Sp}\{ f(\hat{\mathcal{H}})\hat{v}_j(-i\lambda)(1-f(\hat{\mathcal{H}}))\hat{s}_i(t)\}\rangle. \end{aligned} \tag{4}$$

where A is the surface area; T is temperature; $-e$ is the electron charge; $\hat{\mathcal{H}}$ is the total Hamiltonian of the system; $f(\varepsilon)$ is the Fermi distribution function; $\delta \longrightarrow +0$; and $\hat{\mathbf{v}}(t)$ and $\hat{\mathbf{s}}(t)$ are the electron velocity and spin operators in the Heisenberg representation, respectively. The angular brackets stand for the averaging over impurities. The coefficient γ_{ij} is an axial tensor. In the particular case of Hamiltonian (2), $\gamma_{ij} = \gamma\epsilon_{ikj}n_k$, where ϵ_{ikj} is an absolutely antisymmetric tensor.

The averaging over scatterers in Eq. (4) results in the relaxation of the system. This formula can be untangled, e.g., by applying the Edwards diagrammatic technique [3]. Equation (4) can also be interpreted directly without averaging, provided that by δ is meant either the electric field increment growing as ~$\exp(\delta t)$ or the phenomenological inverse relaxation time. One more variant of using this formula amounts to the calculation of the spin density generation rate $\dot{\mathbf{S}} = \delta\mathbf{S}$ rather than its response. If the scattering is weak, this quantity does not contain relaxation at all.

0021-3640/00/7203-0134$20.00

In the absence of scattering, Eq. (4) can be written as

$$\gamma = -\frac{e}{A}\sum_{\mathbf{p};\,\mu\mu'}\frac{f(\varepsilon_\mu(p)) - f(\varepsilon_{\mu'}(p))}{\varepsilon_\mu(p) - \varepsilon_{\mu'}(p)} \times (\mathbf{n}[\mathbf{v}_{\mu\mu'}(\mathbf{p}) \times \mathbf{s}_{\mu'\mu}(\mathbf{p})])\frac{i}{\varepsilon_\mu(p) - \varepsilon_{\mu'}(p) + i\delta}. \quad (5)$$

In the basis of the eigenfunctions of the Rashba Hamiltonian, the matrix elements of the electron velocity and spin operators have the form

$$\mathbf{v}_{\mu\mu}(\mathbf{p}) = \frac{\mathbf{p}}{pm}(p + m|\alpha|\mu), \quad \mathbf{v}_{\mu,-\mu}(\mathbf{p}) = i|\alpha|\mu\frac{[\mathbf{p}\times\mathbf{n}]}{p}, \quad (6)$$

$$\mathbf{s}_{\mu\mu}(\mathbf{p}) = \mu\frac{\alpha[\mathbf{p}\times\mathbf{n}]}{2|\alpha|p}, \quad \mathbf{s}_{\mu,-\mu}(\mathbf{p}) = i\mu\frac{\alpha\mathbf{p}}{2|\alpha|p}. \quad (7)$$

Substitution of Eqs. (6) and (7) into Eq. (5) yields

$$\gamma = me\alpha/4\pi\delta. \quad (8)$$

The relaxation can be included when it is considered that the mean spin can be determined by equating the field-induced generation rate to the rate of spin relaxation with time constant τ_s: $\dot{\mathbf{S}} = \mathbf{S}/\tau_s$. This approach is justified if τ_s does not depend on the electron energy or if only the monoenergetic electrons are involved in the process (Fermi-surface electrons). This results in replacing δ by $1/\tau_s$ in Eq. (8).

An important feature of the spin degrees of freedom is that spin relaxation is slow compared to that of momentum. As a result of the slow relaxation, electrons, when they undergo transition from one spin subband to the other, are accumulated in the latter, thereby enhancing the responses which are sensitive to the electron distribution among the subbands. In particular, the inverse spin relaxation time given by the D'yakonov–Perel' mechanism [11] is proportional to the square of spin subband splitting. At the same time, it is seen from Eq. (8) that the spin generation rate in a lateral static electric field is proportional to the first degree of spin–orbit splitting. As a result, the field-induced mean spin increases instead of decreasing with an increase in the spin–orbit splitting.

To justify and generalize phenomenological result (8), we invoke the method of quantum kinetic equation (QKE). In the basis of Rashba eigenfunctions and in the approximation linear in electric field, the QKE is written as

$$\frac{\partial\rho_{\mu'\mu}(\mathbf{p})}{\partial t} + i(\varepsilon_{\mu'}(p) - \varepsilon_\mu(p))\rho_{\mu'\mu}(\mathbf{p}) - \frac{e\mathbf{E}\mathbf{v}_{\mu'\mu}(\mathbf{p})(f(\varepsilon_{\mu'}(p)) - f(\varepsilon_\mu(p)))}{\varepsilon_{\mu'}(p) - \varepsilon_\mu(p)} = \mathrm{St}(\rho)_{\mu'\mu}. \quad (9)$$

The collisional term responsible for the scattering by impurities has the form

$$\mathrm{St}(\rho)_{\mu'\mu} = \pi N_d\sum_{\mathbf{p}',\,\nu'\nu}\{M_{\mathbf{p}\mu';\,\mathbf{p}'\nu}M_{\mathbf{p}'\nu;\,\mathbf{p}\mu}\rho_{\nu'\nu}(\mathbf{p}') \times [\delta(\varepsilon_{\nu'}(p') - \varepsilon_\mu(p)) + \delta(\varepsilon_\nu(p') - \varepsilon_{\mu'}(p))] - M_{\mathbf{p}\mu';\,\mathbf{p}'\nu'}M_{\mathbf{p}'\nu';\,\mathbf{p}\nu}\rho_{\nu\mu}(\mathbf{p})\delta(\varepsilon_\mu(p) - \varepsilon_{\nu'}(p')) - M_{\mathbf{p}\nu';\,\mathbf{p}'\nu}M_{\mathbf{p}'\nu;\,\mathbf{p}\mu}\rho_{\mu'\nu'}(\mathbf{p})\delta(\varepsilon_{\mu'}(p) - \varepsilon_\nu(p'))\}. \quad (10)$$

In this expression, the matrix elements of interaction with impurities (the spin–orbit corrections to the scatterer potential are ignored) in the same basis are

$$M_{\mathbf{p}\mu';\,\mathbf{p}'\mu} = V(\mathbf{p}' - \mathbf{p})\frac{1}{2}(1 + \mu'\mu e^{i(\phi_\mathbf{p} - \phi_{\mathbf{p}'})}). \quad (11)$$

Here, $V(\mathbf{p})$ is the Fourier transform of the potential of an individual impurity center; N_d is the number of impurity centers; and $\phi_\mathbf{p}$ is the polar angle of the momentum vector.

After transition to a fixed basis set (independent of the $\mathbf{p}$ direction) and neglect of the spin subband splitting in the collisional term, the QKE transforms to

$$\dot{\rho} + i[\mathscr{H}_{so}, \rho] - 2\pi N_d\sum_{\mathbf{p}'}|V(\mathbf{p}' - \mathbf{p})|^2\delta(\varepsilon_p^{(0)} - \varepsilon_{p'}^{(0)}) \times (\rho(\mathbf{p}') - \rho(\mathbf{p})) = \mathscr{F}^{(0)} + \mathscr{F}^{(1)}, \quad (12)$$

where $\mathscr{F}^{(0)}$ and $\mathscr{F}^{(1)}$ are the field-dependent terms of zeroth and first order in spin–orbit coupling constant, respectively:

$$\mathscr{F}^{(0)} = -e\frac{\mathbf{E}\mathbf{p}}{m}f'(\varepsilon), \quad f'(\varepsilon) = \frac{\partial f}{\partial\varepsilon}, \quad \varepsilon = \frac{p^2}{2m}, \quad (13)$$

$$\mathscr{F}^{(1)} = -e\mathbf{E}\left\{\frac{\mathbf{p}}{p^2}(f'(\varepsilon) + 2\varepsilon f''(\varepsilon))\mathscr{H}_{so} - \alpha f'(\varepsilon)\frac{[\mathbf{p}\times\mathbf{n}]}{p^2}(\boldsymbol{\sigma}\mathbf{p})\right\}. \quad (14)$$

The solution of Eq. (12) can be written in the form $\rho = \mathscr{A}(\mathbf{p}) + \mathbf{B}(\mathbf{p})\boldsymbol{\sigma}$. The $\mathscr{A}$ quantity is expressed through $\mathscr{F}^{(0)}$:

$$\mathscr{A} = e\tau_1\frac{\mathbf{E}\mathbf{p}}{m}f'(\varepsilon) \quad (15)$$

where τ_1 is the conventional momentum transport relaxation time. In what follows, the relaxation times of the nth angular distribution function moments are used. They are defined as

$$\tau_n^{-1} = 2\pi N_d\int\frac{d\mathbf{p}'}{(2\pi)^2}|V(\mathbf{p} - \mathbf{p}')|^2 \times \delta(\varepsilon(p) - \varepsilon(p'))(1 - \cos(n(\phi - \phi'))). \quad (16)$$

The **B** quantity is the spin–orbit correction to the field term. It can be represented as the sum of three terms, according to the momentum harmonics:

$$\mathbf{B} = B_0(\varepsilon)[\mathbf{E}\times\mathbf{n}] + B_1(\varepsilon)[\mathbf{E}\times\mathbf{p}]/p + B_2(\varepsilon)([\mathbf{E}\times\mathbf{n}]\mathbf{p})\mathbf{p}/p^2 - \frac{1}{2p}[\mathbf{E}\times\mathbf{p}]. \quad (17)$$

The solution of QKE through the expansion in harmonics with the use of Eq. (17) gives

$$B_0(\varepsilon) = \frac{e}{2\alpha p} \times\left[\frac{1}{\tau_1 p}(f'(\varepsilon)+\varepsilon f''(\varepsilon)) + 2\alpha^2\tau_2 p(f'(\varepsilon)+2\varepsilon f''(\varepsilon))\right], \quad (18)$$

$$B_1(\varepsilon) = -\frac{e}{p}[f'+\varepsilon f''], \quad (19)$$

$$B_2(\varepsilon) = -2e\alpha\tau_2(f'(\varepsilon)+2\varepsilon f''(\varepsilon)). \quad (20)$$

The spin density is equal to the trace of a product of density matrix by spin operator. Only the coefficient $B_0(\varepsilon)$ contributes to this expression. After the appropriate substitution, one obtains

$$\gamma = -\frac{e}{8\pi\alpha}\int_0^\infty \frac{d\varepsilon}{\varepsilon\tau_1}[(f'(\varepsilon)+\varepsilon f''(\varepsilon)) + 4m\alpha^2\tau_1\tau_2\varepsilon(f'(\varepsilon)+2\varepsilon f''(\varepsilon))]. \quad (21)$$

The terms in the second row in Eq. (21) are small if $m\alpha^2\tau_1\tau_2\varepsilon \ll 1$.

In the low-temperature limit, the coefficient γ is determined by the contribution from electrons with energy close to the Fermi energy ε_F:

$$\gamma = \frac{e}{8\pi\alpha}\left[\frac{1}{\tau_1(\varepsilon_F)\varepsilon_F} - \frac{d}{d\varepsilon_F}\left(\frac{1}{\tau_1(\varepsilon_F)}\right)\right]. \quad (22)$$

In the absence of screening, the relaxation time caused by the scattering from charged impurities positioned in the plane of the system is proportional to the electron energy: $\tau_1 \propto \varepsilon$. In this case, one has from Eq. (22)

$$\gamma = e/4\pi\alpha\tau_1(\varepsilon_F)\varepsilon_F. \quad (23)$$

This corresponds to Eq. (8) with $\tau_s^{-1} = \pi\alpha^2 n_s\tau_1$ equal to the impurity-induced inverse spin relaxation time [5]. For the scattering by neutral impurities located in the plane of the system, τ_1 is independent of energy, so that the second term in Eq. (22) turns to zero. As is pointed out above, γ is inversely proportional to the spin subband splitting; i.e., the effect increases with the weakening of the spin–orbit interaction. Clearly, this increase may be suppressed by the inclusion of other spin relaxation mechanisms.

Note that, in addition to the contribution from the Fermi-surface electrons, Eq. (21) at low (though nonzero) temperatures contains the contribution caused by the low-energy divergence. The divergence arises because the band splitting $2\alpha p_F$ at the Fermi energy was assumed to be much smaller than the collisional broadening $1/\tau_{1,2}$. Hence, the energy $m\alpha^2$ determining the domain of applicability of the expansion in powers of α is also smaller than $1/\tau_{1,2}$. As the electron energy decreases, the role of scattering increases, so that the motion can no longer be described by the free-electron solutions. This occurs at energies corresponding to the mobility threshold $\varepsilon_t \sim 1/\tau_1(\varepsilon_t)$. For the scattering by charged impurities, $\varepsilon_t \sim \sqrt{\varepsilon_F/\tau_1(\varepsilon_F)}$. At lower energies, electrons are immobile and the mechanism considered in this work becomes inoperative. For this reason, the ε_t energy can be taken as the upper limit of the integral in Eq. (21). The resulting low-energy contribution to the spin orientation is

$$\gamma \sim \frac{e}{8\pi\alpha T}\exp\left(-\frac{\varepsilon_F}{T}\right)\sqrt{\frac{\varepsilon_F}{\tau_1(\varepsilon_F)}}. \quad (24)$$

The exponential smallness (with respect to temperature) of this contribution can be compensated by a large preexponential factor at a moderate temperature.

According to Eq. (21), a relatively low electron mobility is most appropriate for the observation of the effect. In this case, not only is the coefficient γ large enough, but a strong electric field can also be applied without heating of the electrons and the sample.

In conclusion, let us make estimates for a typical GaAs/GaAlAs heterostructure with an electron concentration of 5×10^{11} cm^{-2}, mobility of 10^4 cm^2/(V s), and $\alpha = 4\times10^5$ cm/s [1]. Substitution in Eq. (23) yields $\gamma = 3\times10^7$ (cm V)$^{-1}$; i.e., 3×10^8 spins are oriented in 1 cm^2 upon applying a field of 10 V/cm.

Let us now briefly discuss the possibility of observing this effect. The spin polarization of 2D electrons could be directly observed by measuring the magnetic moment of the 2D system in an electric field. The infinite plane with in-plane magnetic moment does not produce magnetic field.

Let us consider a 2D strip $-L < y < L$ in the direction of the electric field and the current (x axis). The spins in this strip are oriented along the y axis. Their magnetic moments produce in-plane magnetic field $B_y^{(S)}$ ($z = 0$) outside the system. This field is described by the interpolation formula $B_y^{(S)} = 2g\mu_B SL((y^2 - L^2)^2 + 4d^2L^2)^{-1/2}$ allowing for the finite thickness of the 2D layer $d \sim 4\times10^{-7}$ cm (g is the Lande factor and μ_B is the Bohr magneton). This field is added to the magnetic field of electric current **j** flowing along the strip. At $|y| < L$, this field is equal to $B_y^{(j)} = 2\pi j/c$ above and below the plane. At $|y| > L$ and $z = 0$, the field has only the z component,

which is of the same order of magnitude. For these parameters, the estimates for the maximum values give $B_y^S \sim 3 \times 10^{-3}$ G and $B_z^j \sim 10^{-3}$ G.

The magnetic field may be precisely measured by a SQUID formed in the plane of the sample. Its typical size comprises several micrometers. Because of this, the maximum magnetization field in the SQUID area proves to be lower by three orders of magnitude. At the same time, SQUID is mainly sensitive to the horizontal component of the magnetic field. According to [6], the SQUID sensitivity may be as high as 10^{-14} J/T, which is sufficient for the observation of the effect.

Note that the effect of spin orientation in electric field is, in a sense, the reverse of the effect of current generation under the action of spin-polarized electrons [5]. The authors of [5] considered the primary spin polarization induced by the optical transitions in a circularly polarized light, which eventually gave rise to the steady-state current. In our case, the current arising under the action of a stationary electric field gives rise to the electron spin orientation.

This work was supported in part by the Russian Foundation for Basic Research (project nos. 99-02-17127 and 00-02-17658), the State program "Physics of Solid-State Nanostructures" of the Russian Federation, and the grant of NWO.

REFERENCES

1. Yu. A. Bychkov and E. I. Rashba, Pis'ma Zh. Éksp. Teor. Fiz. **39**, 66 (1984) [JETP Lett. **39**, 78 (1984)]; E. I. Rashba and V. I. Sheka, in *Landau Level Spectroscopy*, Ed. by G. Landwehr and E. I. Rashba (Elsevier, Amsterdam, 1991), p. 178.
2. R. Kubo, J. Phys. Soc. Jpn. **12**, 570 (1957).
3. S. F. Edwards, Philos. Mag. **3**, 1020 (1958).
4. M. I. D'yakonov and V. I. Perel', Zh. Éksp. Teor. Fiz. **60**, 1954 (1971) [Sov. Phys. JETP **33**, 1053 (1971)].
5. E. L. Ivchenko, Yu. B. Lyanda-Geller, and G. E. Pikus, Zh. Éksp. Teor. Fiz. **98**, 989 (1990) [Sov. Phys. JETP **71**, 550 (1990)].
6. I. Meinel, D. Grundler, S. Bargstadt-Franke, *et al.*, Appl. Phys. Lett. **70**, 3305 (1997).

Translated by V. Sakun

JETP Letters, Vol. 72, No. 3, 2000, pp. 138–140. Translated from Pis'ma v Zhurnal Éksperimental'noĭ i Teoreticheskoĭ Fiziki, Vol. 72, No. 3, 2000, pp. 201–204.

Intermediate Asymptotic Expressions for High-Order Spin Correlation Functions in a Two-Dimensional Classical Ferromagnet

I. V. Kolokolov

Budker Institute of Nuclear Physics, Siberian Division, Russian Academy of Sciences, pr. akademika Lavrent'eva 11, Novosibirsk, 630090 Russia

e-mail: kolokolov@inp.nsk.su

Received June 29, 2000; in final form, July 11, 2000

Different-point spin correlation functions are calculated for a two-dimensional classical ferromagnet in a perturbative range of distances r: $a < r \ll m^{-1}$, where a is the lattice parameter and m^{-1} is the correlation length. The expressions for the four- and higher-order correlation functions are presented. © *2000 MAIK "Nauka/Interperiodica".*

PACS numbers: 75.10.Hk; 75.70.Ak

The long-wave static statistical characteristics of a two-dimensional classical Heisenberg ferromagnet are specified by Gibbs measure

$$\prod_{\mathbf{x}} \mathcal{D}\mathbf{n}(\mathbf{x})\delta(\mathbf{n}^2(\mathbf{x}) - 1)\exp\left(-\frac{1}{2g_0}\int d^2\mathbf{x}(\partial_\mu \mathbf{n})^2\right), \quad (1)$$

where $\mathbf{n}$ is a three-component vector and the coupling constant g_0 is proportional to temperature. The lattice with parameter a is assumed to exist at small distances. The limit $g_0 \ll 1$ is considered.

Although expression (1) has long been examined (see references in [1]) under the name of the two-dimensional nonlinear O(3)–σ model, actual progress was made only in Polyakov work [2], where it was demonstrated that the theory (1) is renormalizable and that the effective interaction between the fluctuations of the $\mathbf{n}$ field increases with distance. This result was extended in [3] to the equilibrium dynamics of two-dimensional ferromagnets. There is the exact statement (the Mermin–Wagner theorem) that Eq. (1) does not allow for the spontaneous breaking of symmetry about the global rotations of spins $\mathbf{n}$. It follows from this statement that the pair spin–spin correlation function should decrease with increasing distance. The effective interaction ceases to be weak starting at the scale $r \geq m^{-1} \simeq a\exp(2\pi/g_0)$. The hypothesis that m^{-1} is the correlation length in the system (see [4]) was later confirmed by rigorous results [5–8]. At small distances $a \leq r \ll m^{-1}$, the spin correlation functions can be obtained by summation of leading logarithmic terms of the perturbation series. In this case, $g_0\ln(r/a)$ may be ~1 and the spin correlation functions may vary as strongly as is desired: from the one-site values of order 1 to the asymptotically small (proportional to the positive powers of g_0) values. The two-spin result has long been known [4, 9] and was proved by both rigorous calculations and numerical simulations [10].

In this work, the anomalous dimensionalities of arbitrary tensor operators constructed from the products of vector $\mathbf{n}$ components are calculated in the leading logarithmic approximation. The result proves to be rather simple: a tensor $T^{(l)}$ belonging to the irreducible representation of group O(3) with angular momentum l transforms as

$$T^{(l)} \longrightarrow \left(\frac{g_0}{g(s)}\right)^{l(l+1)/2} T^{(l)}, \quad (2)$$

upon passing from the scale a to the scale $\exp(2\pi s/g_0)$. In Eq. (2), $g(s) = g_0(1 - s)^{-1}$ is the running value of the coupling constant on the scale $a\exp(2\pi s/g_0)$. Although this statement can also be proved within the framework of the Polyakov approach [2], a different formalism, which is more suitable for the perturbative treatment, is used in this work.

Let us begin with the exact statement: for a single spin $\mathbf{n}$ the averaging in measure $d\mathbf{n}\delta(\mathbf{n}^2 - 1)$ is equivalent to the averaging in measure $d\psi^+ d\psi^-$ defined on the $\psi^+\psi^- \leq 4$ disk in the complex plane of variable $\psi^+ = (\psi^-)^*$. When averaging, the components n_z and $n^\pm \equiv n_x \pm in_y$ are expressed through $\psi^\pm$ as follows:

$$n^+ = \psi^+, \quad n^- = \psi^- - \frac{1}{4}(\psi^-)^2\psi^+, \qquad n_z = 1 - \frac{1}{2}\psi^+\psi^-. \quad (3)$$

To prove this theorem, it is sufficient to evaluate the generating function $\mathcal{Z}(\mathbf{h}) = \langle \exp(\mathbf{hn}) \rangle$ by two methods and make sure that the results coincide. Representation (3) can be considered as a formal classical limit of the Dyson–Maleev representation [11, 12] for a quantum spin. However, it should be emphasized that Eq. (3) is not the parametrization of the sphere points in the strict sense; the equality sign in Eq. (3) merely implies that the corresponding means coincide with each other. One can also state that Eq. (3) is the change of variables followed by the deformation of the integration surface (cf. an analogous construction for quantum spins and its use in [13– 15]).

By passing from the $\mathbf{n}$ components to the $\psi^{\pm}$ variables for each spin on the lattice sites, one obtains that the spin fluctuation statistics in a two-dimensional classical ferromagnet is specified by the measure

$$\prod_{\mathbf{x}} \mathcal{D}\psi^{\pm}(\mathbf{x}) \times \exp\left\{-\frac{1}{2g_0}\int d^2\mathbf{x}\left[\partial_\mu\psi^+\partial_\mu\psi^- + \frac{1}{4}(\psi^+)^2(\partial_\mu\psi^-)^2\right]\right\}, \quad (4)$$

with the constraint $\psi^+\psi^- \le 4$ in each point of the space. Note that this constraint (as distinct, say, from $\mathbf{n}^2 = 1$) does not explicitly manifest itself in the perturbation theory.

The fact that the nonlinearity in ψ^+ and ψ^- is asymmetric in Eq. (4) provides the renormalizability of the action and the massless fluctuations in the perturbation theory. After integration in the one-loop approximation for the Fourier components of the $\psi^{\pm}$ field with wave vectors from a^{-1} to $a^{-1}\exp(-2\pi s/g_0)$, the effective measure takes the form

$$\prod_{\mathbf{x}} \mathcal{D}\psi^{\pm}(\mathbf{x}) \times \exp\left\{-\frac{1}{2g_0}\int d^2\mathbf{x}\left[\partial_\mu\psi^+\partial_\mu\psi^- + \frac{g(s)}{4g_0}(\psi^+)^2(\partial_\mu\psi^-)^2\right]\right\}, \quad (5)$$

where $g(s) = g_0(1 - s)^{-1}$. By redetermining the field $\psi^{\pm} \longrightarrow (g_0/g(s))^{1/2}\psi^{\pm}$, the Lagrangian in Eq. (5) is reduced to the initial form, in which g_0 should be replaced by $g(s)$.

The $\psi^+\psi^- < 4$ constraint provides the infrared regularization of the theory because it eliminates infinitely large contributions from the large-scale fluctuations to the means. However, an appropriate detailed analysis is essentially nonperturbative and is beyond the scope of this work. It is merely assumed here that the m^{-1} value (or $s = 1$) can be used as the infrared cutoff parameter of theory (4). In other words, it is assumed, in line with the exact solution [5, 7], that the $\psi^+\psi^- \le 4$ constraint is "processed" into the mass m for the fluctuations with wavelengths $\ge m^{-1}$, so that no logarithmic contributions of such scales arise to the local means. The correlation functions depend logarithmically on m at distances $r \ll m^{-1}$, while the contributions from the fluctuations with $s \longrightarrow 1$ do not contain singularities and have a negligible integral effect at $g_0 \longrightarrow 0$ [see below Eq. (7)]. All this allows the perturbation theory for the nonlinearity in Eq. (4) to be considered local, so that the strong interaction on the confinement scale $\ge m^{-1}$ does not impede the calculations for the intermediate distances with an accuracy indicated above.

The value of $m = a^{-1}\exp(-2\pi/g_0)$ taken as the smallest momentum in the loop integrations corresponds to the recovery of the O(3) symmetry in the leading logarithmic approximation: $\langle n_z \rangle = 1 - \langle \psi^+\psi^- \rangle/2 = 0$. This relationship provides the invariance of means with respect to the infinitesimal rotations about the z axis

$$\delta\psi^+ = \alpha\left(1 - \frac{1}{2}\psi^+\psi^-\right), \quad \delta\psi^- = \frac{\alpha}{4}(\psi^-)^2, \quad \alpha \longrightarrow 0, \quad (6)$$

for the infrared-regularized theory as well. It follows from this that $\langle(\psi^+\psi^-)^m\rangle = 4^m(m + 1)^{-1}$, which is equivalent to the moments of the isotropically distributed vector $\langle n_z^{2m} \rangle = (2m + 1)^{-1}$.

The main property of theory (4) in the calculation of the different-point spin correlation functions is that the operator $(\psi^+)^m$ is covariant with respect to the transformation of the renormalization group: on averaging over the fluctuations in the momentum layer $a^{-1}\exp(-2\pi s/g_0) < k < a^{-1}$, the $(\psi^+)^l$ operator transforms as

$$(\psi^+)^l \longrightarrow \left(\frac{g_0}{g(s)}\right)^{l(l+1)/2}(\psi^+)^l. \quad (7)$$

The $l(l + 1)/2$ exponent is equal to the number of ways of pairing $(\psi^+)^l$ with vertex $(\psi^+)^2(\partial_\mu\psi^-)^2$ plus the $l/2$ term due to the rescaling of the $\psi^{\pm}$ fields. From the viewpoint of the O(3) group elements acting on $\mathbf{n}$, the operator $(\psi^+)^l$ is a vector of highest weight in the irreducible representation with angular momentum l. Because of the invariance about transformation (6), the transformation properties associated with the operations of the renormalization group are uniform throughout the irreducible representation. Equation (2) follows precisely from this fact.

The spin correlation functions of an arbitrary order can be obtained by decomposing the products of $\mathbf{n}$ components into the irreducible tensors of the rotation group. In this case, the dependence on the distances can be determined by the standard summation over the parquet diagrams [16, 17]. Below, the explicit expressions

are given for the four-point correlation function $K_4 = \langle n_z(r_1)n_z(r_2)n_z(r_3)n_z(r_4)\rangle$; to the accuracy adopted in this work, only the following asymptotic geometries are relevant ($r_{jl} \equiv |r_j - r_l|$, $K_4 \equiv (g_0/2\pi)^4\mathcal{H}_4$):

$$r_{12}, r_{34} \ll r_{13} \simeq r_{24} \simeq R$$

$$\mathcal{H}_4 = \frac{4}{45}\frac{\ln^6(mR)}{\ln(mr_{12})\ln(mr_{34})} + \frac{1}{9}\ln^2(mr_{12})\ln^2(mr_{34}), \tag{8}$$

$$r_{12} \ll r_{13} \ll r_{34},$$

$$\mathcal{H}_4 = \frac{4}{45}\frac{\ln^2(mr_{34})\ln^3(mr_{13})}{\ln(mr_{12})} + \frac{1}{9}\ln^2(mr_{12})\ln^2(mr_{34}), \tag{9}$$

$$r_{12} \simeq r_{13} \simeq r_{34} \simeq R, \quad \mathcal{H}_4 = \frac{1}{5}\ln^4(mR). \tag{10}$$

Note in conclusion that $l(l+1)$ in the transformation (2) for the N-component field **n** should be replaced by the eigenvalues of the $O(N)$ group Casimir operator (angular part of the N-dimensional Laplacian) divided by $N-2$.

I gratefully acknowledge V.V. Lebedev for discussions and constructive criticism. I acknowledge A.I. Vaĭnshteĭn, A. Gamba, V.A. Kazakov, E.V. Podivilov, I.B. Khriplovich, and V.L. Chernyak for remarks and advice and M.V. Chertkov for interest in the work. This work was supported by the Russian Foundation for Basic Research, project no. 00-02-17652.

REFERENCES

1. J. Zinn-Justin, *Quantum Field Theory and Critical Phenomena* (Clarendon, Oxford, 1996).
2. A. M. Polyakov, Phys. Lett. B **59**, 79 (1975).
3. V. V. Lebedev, Zh. Éksp. Teor. Fiz. **87**, 1481 (1984) [Sov. Phys. JETP **60**, 851 (1984)].
4. A. M. Polyakov, *Gage Fields and Strings* (Inst. Teor. Fiz. im. L. D. Landau, 1995).
5. Al. B. Zamolodchikov and A. B. Zamolodchikov, Pis'ma Zh. Éksp. Teor. Fiz. **26**, 608 (1977) [JETP Lett. **26**, 457 (1977)].
6. A. M. Polyakov and P. B. Wiegmann, Phys. Lett. B **131**, 121 (1983).
7. P. B. Wiegmann, Pis'ma Zh. Éksp. Teor. Fiz. **41**, 79 (1985) [JETP Lett. **41**, 95 (1985)].
8. V. A. Fateev, V. A. Kazakov, and P. B. Wiegmann, Nucl. Phys. B **424**, 505 (1994).
9. A. Z. Patashinskiĭ and V. L. Pokrovskiĭ, *Fluctuation Theory of Phase Transitions* (Nauka, Moscow, 1982, 2nd ed.; Pergamon, Oxford, 1979).
10. J. Balog and M. Niedermaier, Nucl. Phys. B **500**, 421 (1997).
11. F. Dyson, Phys. Rev. **102**, 1217 (1956).
12. S. V. Maleev, Zh. Éksp. Teor. Fiz. **33**, 1010 (1957) [Sov. Phys. JETP **6**, 776 (1958)].
13. I. V. Kolokolov, Phys. Lett. A **114**, 99 (1986).
14. I. V. Kolokolov and E. V. Podivilov, Zh. Éksp. Teor. Fiz. **95**, 211 (1989) [Sov. Phys. JETP **68**, 119 (1989)].
15. M. Chertkov and I. Kolokolov, Zh. Éksp. Teor. Fiz. **106**, 1525 (1994) [JETP **79**, 824 (1994)].
16. V. V. Sudakov, Zh. Éksp. Teor. Fiz. **30**, 87 (1956) [Sov. Phys. JETP **3**, 65 (1956)].
17. A. I. Larkin and D. E. Khmel'nitskiĭ, Zh. Éksp. Teor. Fiz. **56**, 2087 (1969) [Sov. Phys. JETP **29**, 1123 (1969)].

Translated by V. Sakun

JETP Letters, Vol. 72, No. 3, 2000, pp. 141–143. From Pis'ma v Zhurnal Éksperimental'noĭ i Teoreticheskoĭ Fiziki, Vol. 72, No. 3, 2000, pp. 205–209.

Does the "Quantized Nesting Model" Properly Describe the Magnetic-Field-Induced Spin-Density-Wave Transitions?[1]

A. G. Lebed

Landau Institute for Theoretical Physics, Russian Academy of Sciences, Chernogolovka, Moscow region, 142432 Russia

Department of Physics, Okayama University, 700-8530 Okayama, Japan

Received July 5, 2000

Theoretical reinvestigation of a so-called field-induced spin-density-wave (FISDW) phase diagram in a magnetic field in quasi-one-dimensional compounds $(TMTSF)_2X$ (X = PF_6, ClO_4, AsF_6, etc.) has revealed some novel qualitative features. Among them are (1) the FISDW wave vector is never strictly quantized; and (2) the FISDW phase diagram consists of two regions: (a) "Quantum FISDW," where there exist jumps of the FISDW wave vectors between different FISDW subphases and (b) "Quasiclassical FISDW," where the jumps disappear above some critical points and only one FISDW phase (characterized by a wave vector oscillating with a magnetic field) exists. Both these features are due to taking account of the breaking of an electron–hole symmetry. They contradict the previous textbook theoretical results (including the calculations of the "Three Dimensional Quantum Hall Effect") performed by means of the "Quantized Nesting Model" which explicitly assumes the existence of the electron–hole symmetry. We stress that some effects related to the phenomena described above were experimentally observed but not properly interpreted. *© 2000 MAIK "Nauka/Interperiodica".*

PACS numbers: 75.30.Fv

Quasi-one-dimensional (Q1D) organic compounds $(TMTSF)_2X$ (X = PF_6, ClO_4, AsF_6, etc.) demonstrate a unique and complicated phase diagram in a magnetic field. The primary distinct feature of the phase diagram is a cascade of transitions between different field-induced spin-density-wave (FISDW) subphases [1, 2] (for the reviews, see [3–6]). There is a related "three dimensional quantum Hall effect" (3D QHE) [3–5, 7, 8]. According to [9, 10], the explanation of the metal–SDW phase transition [1–8] lies in a "one-dimensionalization" of a Q1D electron spectrum in a magnetic field and the appearance of an instability in the "Peierls channels." So far, the different FISDW subphases (which appear in a magnetic field) have been described within a so-called "quantized nesting (QN) model" [11–14] (for recent developments of the QN model, see, e.g., [3, 4, 15, 16]). The QN model describes the FISDW subphases by the "quantized SDW order parameter" $\Delta(\mathbf{r})$, which has the form of a plane wave with a quantized value of a longitudinal wave vector:

$$\Delta(\mathbf{r}) = \Delta_N \exp(2ip_F x)\exp(ip_x x) \times \exp\left(i\frac{\pi}{b^*}y\right)\exp\left(i\frac{\pi}{c^*}z\right), \quad (1)$$

$$p_x = 2N(\omega_c/v_F), \quad (2)$$

where N is an integer and $\omega_c = eHv_F b^*/c$ is a cyclotron frequency of the electron motion along open orbits of a Q1D electron spectrum,

$$\epsilon^{\pm}(\mathbf{p}) = \pm v_F(p_x \mp p_F) - 2t_b\cos(p_y b^*) + 2t_b'\cos(2p_y b^*) - 2t_c\cos(p_z c^*), \quad (3)$$

in a transverse magnetic field $\mathbf{H} \parallel \mathbf{z} \parallel \mathbf{c}^*$. Here, +(–) stands for the right (left) sheet of the FS; $v_F \simeq 10^7$ cm/s and p_F are the Fermi velocity and Fermi momentum, respectively; $t_b \simeq 200$ K, $t_b' \simeq 10$ K, and $t_c \simeq 5$ K are the tunneling integrals of the wave functions across the chains [3–6]; and c is the velocity of light, $\hbar \equiv 1$.

According to the QN model [3–5, 11–16], each "quantized FISDW phase" [see Eqs. (1), (2)] at a given magnetic field H is characterized by its metal–SDW transition temperature $T_N(H)$ [3, 4, 11, 15, 16] and its free energy $F_N(H, T)$ [3–5, 12–14], which is lower than the energy of a metallic phase. Thus, to determine the FISDW phase diagram in the framework of the QN model, it is necessary to find the largest value of $T_N(H)$ and the smallest value of $F_N(H, T)$ with respect to an integer parameter N. As a result, one finds a cascade of first-order phase transitions between the different FISDW subphases [3–5, 11–16], with wave vectors being quantized in accordance with Eqs. (1) and (2). Note that the existing calculations of the 3D QHE in the FISDW subphases [3, 4, 17] of $(TMTSF)_2X$ conductors are based on Eqs. (1) and (2).

[1] This article was submitted by the author in English.

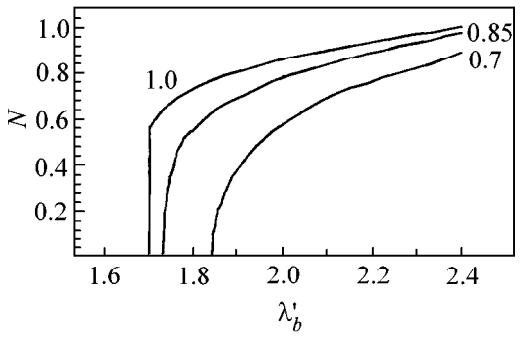

Fig. 1. Three calculated magnetic field dependencies of the parameter N [see Eqs. (1), (2)] ($\lambda_b' \sim 1/H$). At $h \equiv H/2\pi T = 1$, there is a jump of the FISDW wave vector which corresponds to the first-order phase transition (i.e., "quantum FISDW" region). At $h = 0.7$, the parameter N and, thus, the wave vector changes without a jump (i.e., "quasiclassical FISDW" region). The value $h = 0.85$ corresponds to an isolated point of the first-order transition (see Fig. 2 and the text).

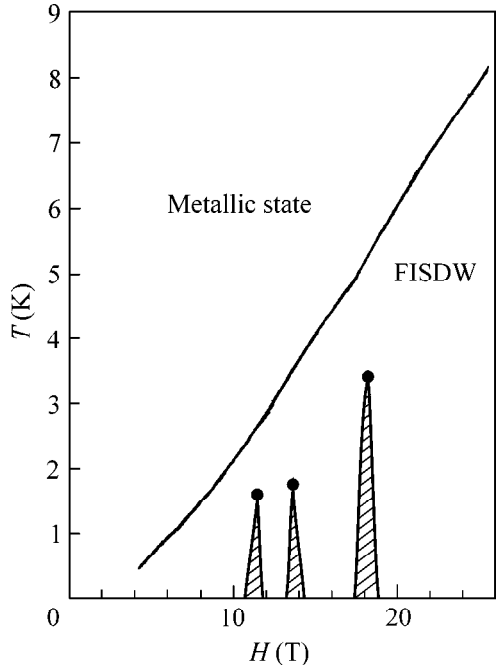

Fig. 2. The FISDW phase diagram suggested in this letter. The solid line stands for the metal–FISDW phase transition; the shaded areas correspond to the first-order transitions between different FISDW subphases; and the full circles correspond to the isolated points of the first-order transitions, above which only one FISDW phase is stable, with the wave vector being an oscillating function of the magnetic field (see Fig. 1 and the text).

The goals of our letter are

(1) To show that, due to the electron–hole asymmetry, the QN model is a limiting case [corresponding to $T_N(H)/\omega_c \longrightarrow 0$] of a more common approach. This means that the basic equations of the QN model [i.e., the quantization of the FISDW wave vector (1), (2)] are only approximately valid in the case $T_N(H)/\omega_c \ll 1$(see Fig. 1). They may be qualitatively used for the determination of the FISDW phase diagram of $(TMTSF)_2ClO_4$ compound, where $T_N(H)/\omega_c$ is a small value.

(2) To demonstrate that our calculations (which take into account the electron–hole asymmetry) lead to a theoretical FISDW diagram of $(TMTSF)_2PF_6$ conductor, which is not even in qualitative agreement with the results of the QN model calculations (see Figs. 1, 2). We recall that a $(TMTSF)_2PF_6$ conductor is the basic material for the observation of the FISDW phase diagram [3, 4] and the related 3D QHE [7, 8, 15, 16] and that experiments [7, 8] performed in $(TMTSF)_2PF_6$ are usually claimed [3, 4, 7, 8] as one of the most reliable confirmations of the applicability of the QN model [i.e., Eqs. (1), (2)] to the FISDW phase diagram. We argue that the real FISDW phase diagram consists of two regions: (a) the "quantum low-temperature region," where there exist jumps of the FISDW wave vectors (i.e., the first-order transitions) between different FISDW subphases. Unlike the results of the QN model [3–5, 11–16, 18], we show that each such subphase is characterized by a noninteger parameter N in Eqs. (1) and (2), and thus the jumps of the wave vectors (1), (2) between different FISDW subphases are also nonintegers; (b) the "quasiclassical moderate-temperature region," where the jumps and the first-order transitions disappear above some critical points and the FISDW phase is characterized by a wave vector oscillating with the magnetic field (see Fig. 2).

(3) To point out that the existing methods for calculating the 3D QHE [3, 4, 15–17] have to be reinvestigated, since they are based on the condition that the parameter N is an exact integer in Eqs. (1) and (2), which is not the case, as shown in this letter.

We recall that the Gor'kov-like equation for the transition temperatures $T_N(H)$ of the FISDW subphases (1) and (2) in a transverse magnetic field ($\mathbf{H} \parallel \mathbf{z} \parallel \mathbf{c}^*$) [9, 11, 15, 16, 18] contains the following matrix elements:

$$\exp\left[i\frac{(\epsilon_1 + \epsilon_2)x}{v_F}\right]\exp\left[i\lambda_b' \sin\left(p_b b^* - \frac{\omega_c x}{v_F}\right)\right] \times \exp\left[2iN\left(\frac{\omega_c}{v_F}\right)x\right]\Delta_N, \quad (4)$$

where ϵ_1 and ϵ_2 are energies of the pairing quasiparticles ($\epsilon_1 + \epsilon_2 \simeq T$), $\lambda_b' = 2t_b'/\omega_c$, and x is a coordinate which changes on the scale $l_T = v_F/2\pi T$. So far, the analytical and numerical calculations of $T_N(H)$ have been performed at $T = 0$ or at negligible ratios of the parameter $T_N(H)/\omega_c$. In this case, one can put $\epsilon_1 = \epsilon_2$ in Eq. (4), and the scale $l_T \longrightarrow \infty$. Since it is necessary to integrate Eq. (4) over the coordinate x, a conclusion was made that the parameter N in Eq. (4) is always an integer. Note that the integer N corresponds to a logarithmic

divergence of the Peierls-type diagram at $T \longrightarrow 0$ [3, 4, 11–14]. In the subsequent works (see, e.g., [3, 4, 16–18]), the parameter N was considered to be an integer even at finite temperatures $T_N(H)$, and the so-called QN model [11–14] [i.e., Eqs. (1) and (2)] was intensively applied to various phenomena [3, 4, 16–18]. Our current analysis shows that, due to the breaking of the electron–hole symmetry in phases with $N \neq 0$, the parameter N in Eqs. (1) and (2) is never integer at finite temperatures.

Below, we calculate the FISDW phase transitions from a metallic phase to the phases with $N \simeq 1$ and $N = 0$. For these purpose, it is convenient to use Eq. (13) from [19],

$$\ln\left(\frac{T_0}{T_N}\right) = \sum_{L=-\infty}^{+\infty} J_L^2\left(\frac{2t_b'}{\omega_c}\right) \times \sum_{M=0}^{+\infty}\left(\frac{1}{2M+1} - \frac{1}{2M+1+i\delta_N} + \text{c.c}\right), \quad (5)$$

$$\delta_N = \frac{\omega_c}{2\pi T_N(H)}(L-N), \quad (6)$$

where T_0 is the temperature of the phase transition to the last FISDW phase characterized by $N = 0$.

Numerical solutions of Eqs. (5) and (6) for the values of the band parameters of $(TMTSF)_2PF_6$ (see their values above) are summarized in Fig. 1 and in the caption to Fig. 1. It is shown that there are two regions of the FISDW phase diagram: (a) "quantum FISDW": a cascade of the first order transitions with noninteger jumps of the wave vectors; (b) "quasiclassical FISDW," which is characterized by the oscillation of a wave vector in a magnetic field and which exists above critical points of the first-order transitions (see Figs. 1, 2 and the figure captions).

Summarizing our results, we claim that the textbook QN model [3–5, 11–14, 16, 18] is a limiting case of a more general physical scheme and that the applicability of the QN model to the real FISDW transitions gives results which are qualitatively inconsistent with the exact numerical calculations. In particular, the existing calculations of the 3D QHE has to be completely reinvestigated. At the end of the paper, we would like to point out that a number of experimentally observed features of the FISDW phase diagram in $(TMTSF)_2PF_6$ could not be interpreted in terms of the QN model. Indeed, the authors of [7] were not able to find the phase boundaries between different FISDW subphases at $T \geq 2$ K, and the authors of [8] could not detect the hysteresis (which is evidence of the cascade of the first order FISDW transitions) above $T \simeq 3$ K. Note that in both cases the metal–FISDW transition temperatures were significantly higher than 3 K. From Fig. 2, it is seen that these features are in accordance with the FISDW phase diagram suggested in the Letter. To prove more firmly the FISDW phase diagram suggested by us, A. Kornilov *et al.* have recently studied the behavior of the hysteresis inside the FISDW diagram.[2] Their preliminary results are in qualitative agreement with our calculations.

I am thankful to N.N. Bagmet, E.V. Brusse, P.M. Chaikin, M.J. Naughton, A. Kornilov, V.M. Pudalov, K. Yamaji for fruitful and numerous discussions.

REFERENCES

1. P. M. Chaĭkin, Mu-Yong Choi, J. F. Kwak, *et al.*, Phys. Rev. Lett. **51**, 2333 (1983).
2. M. Ribault, D. Jerome, D. Tuchender, *et al.*, J. Phys. Lett. **44**, L953 (1983).
3. T. Ishiguro, K. Yamaji, and G. Saito, *Organic Superconductors* (Springer-Verlag, Heidelberg, 1998, 2nd ed.).
4. P. Lederer, J. Phys. I **6**, 1899 (1996); V. M. Yakovenko and H.-S. Goan, J. Phys. I **6**, 1917 (1996).
5. L. P. Gor'kov, Sov. Phys. Usp. **27**, 809 (1984).
6. D. Jerome and H. J. Schultz, Adv. Phys. **31**, 299 (1982).
7. S. T. Hannahs, J. S. Brooks, W. Kang, *et al.*, Phys. Rev. Lett. **63**, 1988 (1989).
8. J. R. Cooper, W. Kang, P. Auban, *et al.*, Phys. Rev. Lett. **63**, 1984 (1989).
9. L. P. Gor'kov and A. G. Lebed, J. Phys. Lett. **45**, L433 (1984).
10. P. M. Chaĭkin, Phys. Rev. B **31**, 4770 (1985).
11. M. Heritier, G. Montambaux, and P. Lederer, J. Phys. Lett. **45**, L943 (1984).
12. A. G. Lebed, Zh. Éksp. Teor. Fiz. **89**, 1034 (1985) [Sov. Phys. JETP **62**, 595 (1985)].
13. K. Yamaji, Synth. Met. **13**, 29 (1986).
14. K. Maki, Phys. Rev. B **33**, 4826 (1986).
15. N. Dupuis and V. M. Yakovenko, Phys. Rev. Lett. **80**, 3618 (1998).
16. D. Zanchi and G. Montambaux, Phys. Rev. Lett. **77**, 366 (1996).
17. D. Poilblanc, G. Montambaux, M. Heritier, *et al.*, Phys. Rev. Lett. **58**, 270 (1987).
18. G. Montambaux, M. Heritier, and P. Lederer, Phys. Rev. Lett. **55**, 2078 (1985).
19. L. P. Gor'kov and A. G. Lebed, Phys. Rev. B **51**, 3285 (1995).

[2] A. Kornilov, private communication.

JETP Letters, Vol. 72, No. 3, 2000, pp. 144–147. Translated from Pis'ma v Zhurnal Éksperimental'noĭ i Teoreticheskoĭ Fiziki, Vol. 72, No. 3, 2000, pp. 210–215.

Magnetic Properties of a Monocrystalline Quasicrystal in the Al–Pd–Mn System

A. A. Rempel'*, S. Z. Nazarova, and A. I. Gusev*

Institute of Solid-State Chemistry, Ural Division, Russian Academy of Sciences, ul. Pervomaĭskaya 91, Yekaterinburg, 620219 Russia

** e-mail: rempel@ihim.uran.ru, gusev@ihim.uran.ru*

Received July 6, 2000

Magnetic susceptibility of a monocrystalline icosahedral $Al_{70.2}Pd_{21.3}Mn_{8.5}$ quasicrystal was measured over the temperature range from 4 to 1100 K. The susceptibility was found to include the temperature-independent diamagnetic contribution, the temperature-dependent Curie's contribution, and the contribution from the Pauli paramagnetism of an electron system with energy gap. An analysis of the low-temperature susceptibility revealed the presence of about 0.008% of ions with magnetic moment $4\mu_B$ in the quasicrystal at 4 K. It is assumed that the ions with uncompensated magnetic moments appear near the structural vacancies in the quasicrystal lattice. The energy gap between the valence and conduction bands is estimated at $\Delta = 0.64$ eV, and the effective mass of charge carriers is equal to approximately 70 electron masses. © *2000 MAIK "Nauka/Interperiodica".*

PACS numbers: 75.50.Kj; 75.0.Ej; 61.44.Br

Since the experimental discovery of a quasicrystalline solid state [1], it has persistently attracted attention of researchers. Because of the lack of translational symmetry [2], the quasicrystals possess unusual mechanical, electrical [3, 4], and magnetic [4, 5] properties. The role of atomic defects (vacancies in different sublattices, free volumes, vacancy clusters) is the key to understanding the quasicrystal stability, structure [6], and properties. Impurity defects also have an appreciable influence on the properties of quasicrystals.

The magnetic properties and the electronic structure of this new class of materials are still not unambiguously elucidated. The questions as to what type of conductors (metals or semiconductors) and magnets the quasicrystals belong to and how the lack of translational symmetry and the presence of fivefold symmetry axes in their crystal structure and, as a result, the smeared Fermi surface reflect on their electronic structure are still open questions. The investigation into the magnetic properties of high-purity defectless monocrystalline quasicrystals is quite helpful in answering these questions. Stable icosahedral phases were found in several ternary systems of aluminum with some elements such as Cu, Fe, Ru, Pd, Re, Mn, and Si.

This work is devoted to studying the magnetic susceptibility χ of a high-purity single-crystal sample of the $Al_{70.2}Pd_{21.3}Mn_{8.5}$ quasicrystal with the icosahedral structure satisfactorily described by the Boudard model structure [7].

An $Al_{70.2}Pd_{21.3}Mn_{8.5}$ single crystal with a minimum impurity content (less than 1 at. %) and porosity of less than 5% was grown by the Czochralski method at the Institut für Festkörperforschung (Forschungszentrum Jülich GmbH, Germany).

Magnetic measurements over the temperature range 4–300 K were made on a Quantum Design MPMS-XL-5 vibrating-coil magnetometer. At temperatures from 300 to 1000 K, the susceptibility was measured by the Faraday method on a Domenicali pendulum balance. Low-temperature measurements were performed in magnetic fields of up to 50 kOe, with the twofold axis of the single crystal being aligned with or perpendicular to the field. At temperatures above 300 K, the susceptibility χ was measured in fields from 7.2 to 8.8 kOe for a powder of the same crystal.

The results of measuring the magnetization σ at different orientations of the $Al_{70.2}Pd_{21.3}Mn_{8.5}$ sample about the magnetic field are presented in Fig. 1 for a temperature of 300 K. The susceptibility changes slightly from -0.39×10^{-6} to -0.37×10^{-6} cm^3 g^{-1} as the twofold axis of the crystal changes its orientation about the field H from parallel to perpendicular. The magnetic anisotropy was observed earlier in [8] for a compositionally close monocrystalline $Al_{70.5}Pd_{21.1}Mn_{8.4}$ quasicrystal. At a temperature of 200 K, the susceptibility of a single crystal with parallel orientations of the twofold and fivefold axes was found to be -0.15×10^{-6} and -0.16×10^{-6} cm^3 g^{-1}, respectively. Thus, measurements showed a weak crystallographic anisotropy for the susceptibility of the monocrystalline $Al_{70.2}Pd_{21.3}Mn_{8.5}$ quasicrystal. In the subsequent figures, all experimental results relate to the situation where the twofold axis is aligned with the magnetic field.

The experimentally measured temperature dependence of the susceptibility $\chi(T)$ shows two distinct

regions with the opposite slopes of the $\chi(T)$ curve. A sharp decrease at low temperatures ($T < 300$ K) is typical of the Curie's law $\chi = C/T$.

Let us first consider the low-temperature portion of the $\chi(T)$ dependence in more detail. When interpreting the results of magnetic measurements, the presence of a low-temperature paramagnetic "tail" is often explained by the presence of ferromagnetic impurities. To reveal whether the sample contained ferromagnetic impurities or not, we measured the magnetization σ as a function of magnetic field H. No remanent magnetization was detected in the quasicrystal, as was evident from the fact that the $\sigma(H)$ curves constructed for different temperatures passed through the origin of coordinates (Fig. 2). This evidenced the absence of the ferromagnetic impurities in the sample studied, so that the observed paramagnetic Curie's component in the susceptibility was most likely caused by the structural features of the quasicrystal.

The nonlinear $\sigma(H)$ dependence measured at 4 K in the fields above 20 kOe is caused by the approach of magnetization saturation, i.e., by a cryomagnetic anomaly. Without regard for space quantization and interatomic interactions, the magnetization per unit volume is [9]

$$\sigma_V(H) = Nn\mu L(\mu H/k_BT), \qquad (1)$$

where N is the number of atoms in a unit volume; n is the relative concentration of atoms with nonzero magnetic moment; $\mu = p\mu_B$ is the magnetic moment; and $L(x) = (\coth x - 1/x)$ is the Langevin function. One can readily see that, at low temperatures and strong fields such that $\mu H \gg k_BT$, the Langevin function $L(x) \longrightarrow 1$ and, hence, the magnetization σ_V reaches saturation. Taking into account that $N = N_A\rho/M$ (N_A is the Avogadro's number, ρ is the density, and M is the molecular mass) and that the magnetization per unit mass is $\sigma = \sigma_V/\rho$, Eq. (1) can be rewritten in the form corresponding to the magnetization per unit mass:

$$\sigma(H) = (N_A/M)np\mu_BL(p\mu_BH/k_BT). \qquad (2)$$

To calculate the parameters of Eq. (2), the measured magnetization was corrected for the temperature-independent diamagnetic contribution, which was added to the right-hand side of Eq. (2) in the form of a χ_0H term. It was found that the experimental dependence $\sigma(H)$ at $T = 4$ K was satisfactorily fitted by Eq. (2) with the parameters $p = 3.99$ and $n = 8.1 \times 10^{-5}$. Therefore, at a temperature of 4 K, the magnetic moments of about 0.008% of the atoms in quasicrystal are uncompensated and equal to approximately $4\mu_B$. This value is most suited for the Mn^{4+}ions [9] and can be due to the uncompensated magnetic moments of the Mn atoms situated near structural defects or in the lattice sites belonging to the atoms of different sort. With allowance made for the Mn content in the quasicrystal, one of 1000 manganese atoms has a magnetic moment of $4\mu_B$

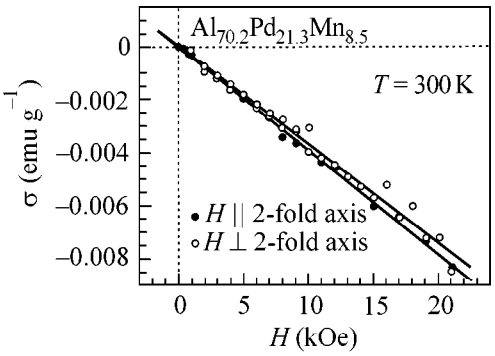

Fig. 1. Different slopes of the $\sigma(T)$ curves obtained for the orientations of the twofold axis parallel and perpendicular to the magnetic field H is evidence for a weak anisotropy of the quasicrystal magnetization.

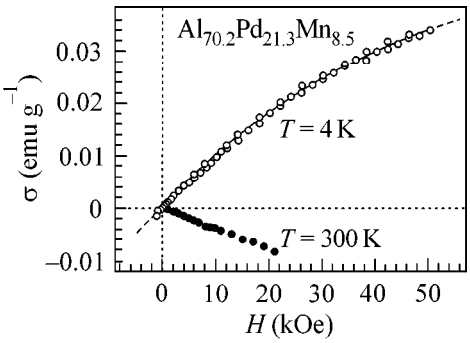

Fig. 2. Magnetization σ of the $Al_{70.2}Pd_{21.3}Mn_{8.5}$ quasicrystal vs. magnetic field H at 4 and 300 K. The nonlinear character of the $\sigma(H)$ dependence measured at a temperature of 4 K in fields $H > 20$ kOe is caused by the cryomagnetic anomaly. Solid line is the approximation of the $\sigma(H)$ dependence by Eq. (2). The relative concentration n of the ions with magnetic moments of $\sim 4\mu_B$ is 8.1×10^{-5}.

at 4 K. The presence of atomic defects in the lattice of the quasicrystal studied is confirmed by the positron annihilation data [6]. Indeed, the value of 214 ± 4 ps found for the positron lifetime is evidence for the presence of structural vacancies, i.e., unoccupied lattice sites in the quasicrystal.

A change in the susceptibility at temperatures below 300 K is shown in Fig. 3. The experimentally measured $\chi(T)$ dependence is described by the Curie's law with the temperature-independent diamagnetic contribution. At temperatures below 30 K, the susceptibility increases slower than follows from the Curie's law. This deviation is due to the above-mentioned cryomagnetic anomaly. In the range from 4 to 20 K, the C parameter is equal to 5.13×10^{-6} cm^3 K g^{-1}, while, in the broader high-temperature interval 20–300 K, $C = 8.53 \times 10^{-6}$ cm^3 K g^{-1}. For the temperature range 4–300 K, the C parameter is equal to 8.03×10^{-6} cm^3 K g^{-1}.

The general form of the $\chi(T)$ dependence at $H = 8.8$ kOe in the temperature range from 4 to 1000 K is

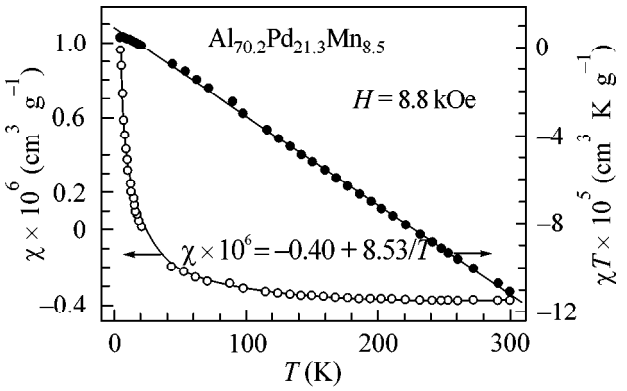

Fig. 3. Low-temperature susceptibility χ of the monocrystalline $Al_{70.2}Pd_{21.3}Mn_{8.5}$ quasicrystal. The nonlinearity in the $\chi(T)$ dependence at temperatures below 30 K is caused by the cryomagnetic anomaly. Measurements were made at $H = 8.8$ kOe.

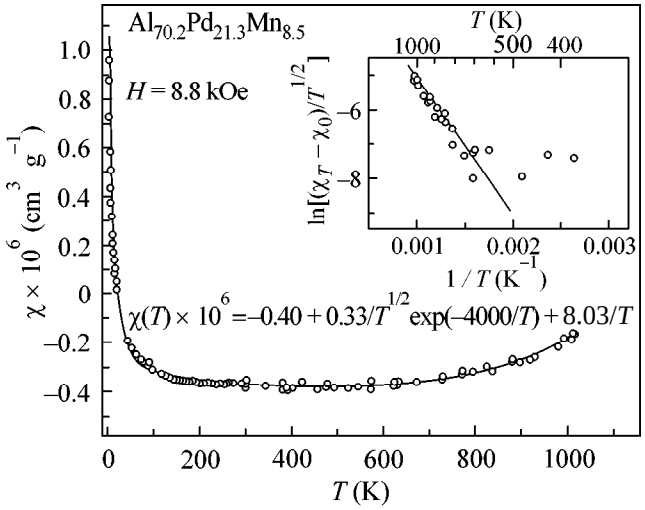

Fig. 4. Magnetic susceptibility of the $Al_{70.2}Pd_{21.3}Mn_{8.5}$ quasicrystal in the temperature range from 4 to 1000 K. In the inset, the high-temperature susceptibility is shown as a function of $1/T$. The approximation of the $\chi(T)$ dependence by Eq. (5) is shown by the solid line.

shown in Fig. 4. The second portion of the $\chi(T)$ dependence corresponds to temperatures above 300 K. This portion is characterized by a nonlinear increase in the susceptibility, suggesting that the paramagnetism is enhanced with temperature. A numerical analysis showed that in the temperature range 300–1000 K the susceptibility $\chi(T) \propto T^{1/2}\exp(-B/T)$. Such a dependence is typical of semiconductors, where the thermally activated charge carriers form a nondegenerate electron gas obeying the Boltzmann statistics. According to [9, 10], the electron concentration in the conduction band in this case is described by the function

$$n_e = 2(m^*)^{3/2}(k_BT/2\pi\hbar^2)^{3/2}\exp(-\Delta/2k_BT), \quad (3)$$

where m^* is the electron effective mass and Δ is the energy gap between the valence and conduction bands. Then, in accordance with the Curie's law $\chi_p(T) = n_e(\mu_B)^2/k_BT$, the temperature-dependent part of susceptibility has the paramagnetic component of the form

$$\chi_p(T) = 2(m^*/2\pi\hbar^2)^{3/2}(k_B)^{1/2}(\mu_B)^2T^{1/2} \times \exp(-\Delta/2k_BT) \equiv AT^{1/2}\exp(-B/T), \quad (4)$$

where $A = 2(m_0/2\pi\hbar^2)^{3/2}(k_B)^{1/2}(\mu_B)^2q^{3/2} = 3.008 \times 10^{-9}q^{3/2}$ [K$^{-1/2}$]; $q = m^*/m_0$; m_0 is the electron mass; and $B = \Delta/2k_B$. Note that Eq. (4) is written for the dimensionless susceptibility per unit volume. With allowance made for the above-mentioned features of the $\chi(T)$ dependence, the susceptibility per unit mass of the quasicrystal was approximated in the whole temperature range from 4 to 1000 K by formula

$$\chi(T) = \chi_0 + A_mT^{1/2}\exp(-B/T) + C/T, \quad (5)$$

where the temperature-independent contribution χ_0, the temperature-dependent Pauli paramagnetism of the electron system with energy gap, and the paramagnetic Curie's contribution were taken into account. The coefficient $A_m = A/\rho$, where $\rho = 5.37$ g cm^{-3} is the density of the $Al_{70.2}Pd_{21.3}Mn_{8.5}$ quasicrystal.

The temperature-independent contribution $\chi_0 = -0.40 \times 10^{-6}$ cm^3 g^{-1} in Eq. (5) is diamagnetic and caused by the diamagnetism of the Al, Pd, and Mn atomic cores.

The effective magnetic moment μ_{eff} corresponding to the parameter $C = 5.13$–8.53×10^{-6} cm^3 K g^{-1} and calculated with regard to the quasicrystal density is as small as ~0.04–0.06μ_B. This value is obtained by averaging over all atoms of the quasicrystal. Since the relative concentration of magnetic ions is $n = 8.1 \times 10^{-5}$, the magnetic moment derived at low temperatures from the corresponding parameter $C = 5.13 \times 10^{-6}$ cm^3 K g^{-1} is ~4.8μ_B. Therefore, the results of processing the field and temperature dependences of the susceptibility are in good agreement with each other.

The coefficient A_m in Eq. (5) is equal to 0.33×10^{-6} cm^3 g^{-1} K$^{-1/2}$. The absolute effective mass of carriers can be estimated either from the formula

$$m^* = (2A^2)^{1/3}\pi\hbar^2(k_B\mu_B^4)^{-1/3} \equiv [2(A_m\rho)^2]^{1/3}\pi\hbar^2(k_B\mu_B^4)^{-1/3} \quad (6)$$

or through the electron mass m_0,

$$m^* = 4.799 \times 10^5A^{2/3}m_0 \equiv 4.799 \times 10^5(A_m\rho)^{2/3}m_0, \quad (7)$$

if the coefficient $A = A_m\rho$ is known. The estimate showed that the effective mass is rather large and equal to ~70m_0. The large effective electron mass justifies the use of the classical Boltzmann statistics for the description of a nondegenerate electron gas. The energy gap between the valence and conduction bands is small and

equal to $\Delta = 2k_BB = 0.64$ eV. These data allow the $Al_{70.2}Pd_{21.3}Mn_{8.5}$ quasicrystal to be considered as a narrow-gap semiconductor.

In summary, it has been established in this work that the quasicrystal contains structural defects. As a result, the impurity levels may appear within the energy gap. In particular, an assumption about the fine structure of energy gap was made in [11] on the basis of the appreciable scatter of points in the $\ln[(\chi_T - \chi_0)/T^{1/2}]$ vs. $1/T$ plot obtained upon measuring the susceptibility of the $Al_{62.0}Cu_{25.5}Fe_{12.5}$ quasicrystal at $T < 50$ K. The authors of [11] assumed that the activation parameter for the carriers within a layer of 0.1 eV near the Fermi level takes a set of discrete values spaced by several tens of millielectronvolts. However, in this work, the $\ln[(\chi_T - \chi_0)/T^{1/2}]$ vs. $1/T$ curve is smooth (a certain scatter of the points is seen only at high temperature near 400 K), so that one cannot speak about the fine structure of the gap. To study the impurity levels or the fine structure of the gap, spectroscopic measurements are necessary.

We thank H.-E. Schaefer for discussing the results, B. Grushko for providing with the sample, and A.V. Korolev for assistance in the experiment.

REFERENCES

1. D. Shechtman, I. Blech, J. Cahn, and D. Gratias, Phys. Rev. Lett. **53**, 1951 (1984).
2. D. Shechtman and I. Blech, Metall. Trans. A **16**, 1005 (1985).
3. S. L. Poon, Adv. Phys. **41**, 303 (1992).
4. *Lectures on Quasicrystals*, Ed. by F. Hippart and D. Gratias (Les Editions de Physique, Les Ulis, 1994).
5. R. Bellissent, F. Hippert, P. Monod, and F. Vigneron, Phys. Rev. B **36**, 5540 (1987).
6. F. Baier, A. Rempel, R. Würschum, and H.-E. Schaefer, in *Quasicrystals at Strasbourg: Joint Colloquium of GDR-CINQ and SPQK* (Univ. L. Pasteur, Strasbourg, 1998), p.18.
7. M. Boudard, M. de Boissieu, C. Janot, *et al.*, J. Phys.: Condens. Matter **4**, 10149 (1992).
8. M. Rodmar, M. Ahlgren, C. Berger, *et al.*, Czech. J. Phys. 46 (S5), 2703 (1996).
9. S. V. Vonsovskiĭ, *Magnetism* (Nauka, Moscow, 1971; Wiley, New York, 1974).
10. J. S. Blakemore, *Solid State Physics* (Cambridge Univ. Press, Cambridge, 1985).
11. A. F. Prekul, N. Yu. Kuz'min, and N. I. Shchegolikhina, Pis'ma Zh. Éksp. Teor. Fiz. **69**, 206 (1999) [JETP Lett. **69**, 221 (1999)].

Translated by V. Sakun

JETP Letters, Vol. 72, No. 3, 2000, pp. 148–152. Translated from Pis'ma v Zhurnal Éksperimental'noĭ i Teoreticheskoĭ Fiziki, Vol. 72, No. 3, 2000, pp. 216–222.

Ordering in an Ensemble of Nanometer-Size Au Clusters on a NaCl(100) Surface at High Deposition Rates

V. D. Borman*, A. V. Zenkevich*, S. Ch. Laĭ*, V. N. Nevolin*, M. A. Pushkin*, V. N. Tronin*, V. I. Troyan* *, and J. Chevallier**

**Moscow Institute of Engineering Physics, Kashirskoe sh. 31, Moscow, 115409 Russia*
***e-mail: mal@park.mephi.ru*
***Institute of Physics and Astronomy, University of Århus, DK-8000 Arhus C, Denmark*
Received July 4, 2000; in final form, July 10, 2000

The results of experimental studies on pulsed laser deposition of the Au atoms on the NaCl(100) surface are reported. Under the conditions far from thermodynamic equilibrium, the spatial ordering was observed in an ensemble of gold clusters at the initial deposition stage. A mechanism based on the idea of fractal structure decomposition caused by the development of unstable concentration modes in the condensed substance is proposed. © *2000 MAIK "Nauka/Interperiodica".*

PACS numbers: 81.15.Fg; 68.55.Nq; 36.40.-c

Interest in the formation of ordered structures in an ensemble of nanometer-scale metal clusters on a surface is associated both with the problem of the formation of a system of quantum dots on superconductor surfaces [1] and with the fundamental problem of phase transition kinetics under strongly nonequilibrium conditions [2]. The ordering in an ensemble of Au clusters can occur under strongly nonequilibrium conditions at the initial stage of phase nucleation as a result of the development of unstable concentration modes corresponding to certain wave vectors in a deposited substance. Cluster ordering was recently observed only under weakly nonequilibrium conditions in the Lifshitz–Slezov coalescence regime [3] for an ensemble of micrometer-scale clusters [4–6].

In this work, the ordering in a system of nanometer-scale gold clusters is observed at the initial stage of phase growth upon pulsed laser deposition (PLD) on a NaCl (100) surface [7, 8] under the conditions far from thermodynamic equilibrium.

The phase nucleation is usually analyzed in terms of either the Zel'dovich–Volmer–Weber (ZVW) theory [9] or the atomistic theory [10], which do not apply to the systems far from thermodynamic equilibrium. When modeling the phase transition kinetics in such a situation, it would be more appropriate to invoke unstable states (spinodal decomposition) [11, 12] to allow for the appearance of modulated relaxational structures. However, we found that, upon a single-pulse laser deposition ($\tau_p \approx 10^{-6}$ s), no ordering occurred in an ensemble of 3D gold clusters (drops). At the same time, after 50 pulses the ordered structure was formed in a cluster ensemble consisting of the same amount of the deposited substance.

The formation of an ensemble of 3D clusters is suggested to be a result of the decomposition of 2D fractal structures that arise when the coverage degree reaches the percolation threshold $\theta \approx \theta_c$ during a single pulse. The resulting 2D fractal structures are unstable, because they form under thermodynamically highly nonequilibrium conditions. Owing to the development of the unstable density fluctuation modes in the deposited substance, the 2D fractal structures decompose to transform into the 3D clusters.

The experimental study of the nucleation and growth of gold clusters on the NaCl (100) surface was performed using transmission electron microscopy (TEM) with samples prepared by Au laser deposition onto freshly cleaved NaCl (100) crystals at room temperature under an ultrahigh vacuum ($P_{res} \approx 5 \times 10^{-10}$ Torr). The composition of the deposited metal was monitored *in situ* by X-ray photoelectron spectroscopy. The radiation of a Q-switched (τ = 15 ns) Nd^{3+}:YAG laser (λ = 1.06 μm) with an output of E = 80–200 mJ and a pulse repetition rate of 25 Hz was focused onto an Au target. By changing the mutual geometry of the target and substrate and the laser output, the number of Au atoms deposited per pulse was varied within 10^{13}–10^{15} at/cm^2 at a pulse duration of $\tau_p \sim 10^{-7}$–10^{-6} s. According to [8, 13], at a laser output of 10^8–10^9 W/cm^2 and in the presence of up to 5% ionized component in the atomic beam, the energy of the deposited atoms is 10–100 eV. Additional comparative experiments on Au deposition on the preliminarily irradiated or nonirradiated NaCl surface showed that, within the experimental accuracy, there was no difference in the distributions of Au clusters. The total number of Au atoms deposited on a unit surface was measured *ex situ* by Rutherford

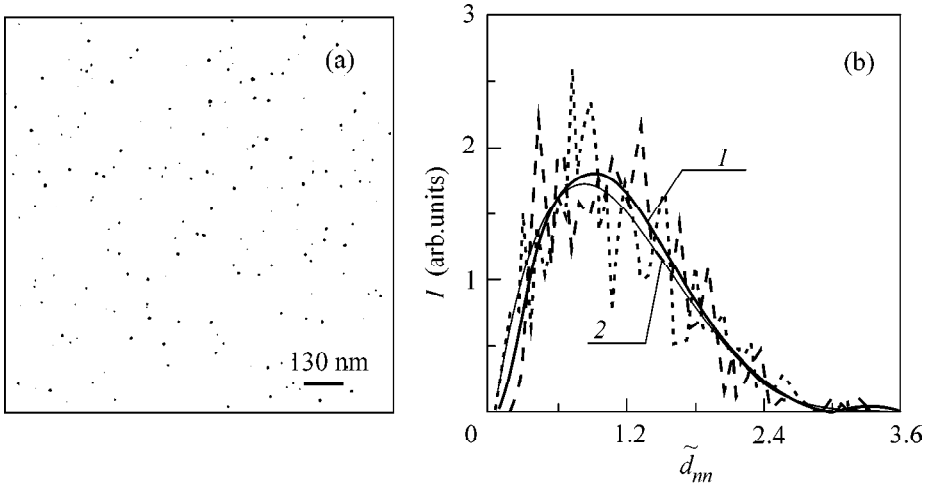

Fig. 1. (a) TEM image of the Au clusters deposited on the NaCl (100) surface after a single laser pulse. (b) Distribution functions for the distances $\tilde{d}_{nn} = d_{nn}/\langle d\rangle$ between the nearest neighbors: (*1*) after a single laser pulse ($\langle d\rangle$ = 415 Å) and (*2*) random distribution.

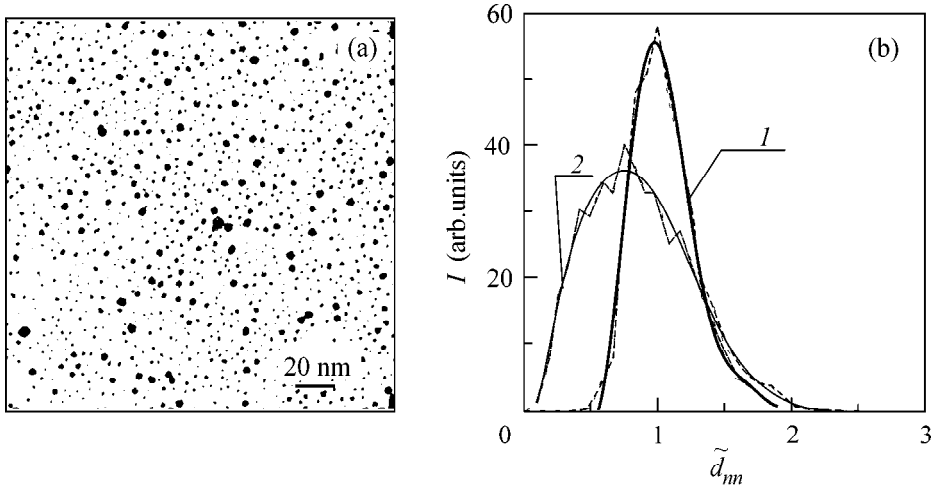

Fig. 2. (a) TEM image of the Au clusters deposited on the NaCl (100) surface after 50 laser pulses. (b) Distribution functions for the distances $\tilde{d}_{nn} = d_{nn}/\langle d\rangle$ between the nearest neighbors: (*1*) after 50 laser pulses ($\langle d\rangle$ = 35 Å) and (*2*) random distribution.

backscattering spectroscopy (RBS) of the He^+ ions. The RBS data suggested that the number of atoms deposited during $\tau_p \approx 10^{-6}$ (N = 1 pulse) was $n \approx 5 \times 10^{14}$ at/cm^2. The corresponding surface coverage degree was $\theta \simeq n/n_0 \simeq 0.77$ {$n_0 \approx 6.7 \times 10^{14}$ at/cm^2 is the surface concentration of active centers on NaCl (100) [14]}.

The TEM images can be used for reconstructing the cluster distribution function $f(\tilde{d}_{nn})$ over the distances between the nearest neighbors ($\tilde{d}_{nn} = d_{nn}/\langle d\rangle$) and for the Fourier analysis of these images.

A typical fragment of the TEM image of the Au clusters formed on the NaCl (100) surface after a single-pulse laser deposition is shown in Fig. 1a. Estimates show that the number of atoms in the visible clusters is ~20% of their total amount determined from RBS. The $f(\tilde{d}_{nn})$ distribution is shown in Fig. 1b. In this figure, $\langle d\rangle$ = 415 Å. The model distribution function constructed for a system of points randomly scattered across the surface with density equal to the mean cluster density is shown in the same figure. One can see that the distribution function $f(\tilde{d}_{nn})$ of the Au clusters at N = 1 coincides, within the experimental error, with the random distribution.

The TEM image of the Au clusters formed from the same number $n \approx 5 \times 10^{14}$ at/cm^2 of atoms deposited on the NaCl surface after 50 pulses is shown in Fig. 2a. The corresponding distribution $f(\tilde{d}_{nn})$ over the distances between the nearest neighbors is shown in Fig. 2b ($\langle d\rangle$ = 35 Å). One can see that the distribution

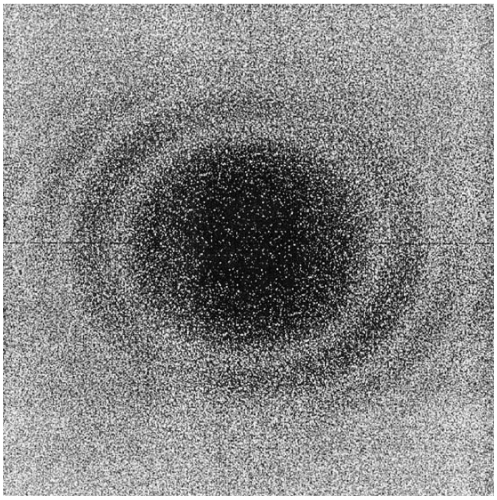

Fig. 3. Fourier transform of the TEM image of the Au clusters deposited on the NaCl (100) surface after 50 laser pulses.

of clusters over distances is narrower than in the $N = 1$ case. The results of Fourier analysis of the TEM images of the Au clusters on NaCl are presented in Fig. 3. The presence of characteristic diffuse rings is evidence for the ordering in the cluster system. These data correlate with the computational results obtained for the distribution over the d_{nn} distances. The observed diffraction pattern points to the presence of a characteristic scale of cluster ordering $L_k = 2\pi/k$, with $k \approx (1.9 \pm 0.2) \times 10^7$ cm^{-1}. The narrowing of this function, compared to the random distribution $f(\tilde{d}_{nn})$, and the position of its maximum (Fig. 2b) are also evidence for the possible ordering in the cluster ensemble. The absence of diffraction rings in the Fourier-processed TEM images of clusters formed after a single pulse and in a system of randomly distributed points corroborates the disordered (random) distribution $f(\tilde{d}_{nn})$ for $N = 1$.

Therefore, it was found from the experiments that the clusters are randomly distributed during the pulse duration time ($\tau_p \approx 10^{-6}$ s). For the same amount of a substance deposited in $t \approx 2$ s ($N = 50$ and $f = 25$ Hz), the cluster distribution over distances is different from random; namely, it becomes narrower and ordered.

The specific feature of PLD is that at times $\tau_p \approx 10^{-6}$ s of particle transportation the deposition rate is much higher than in the case of thermal evaporation ($j_{\text{PLD}}/j_{\text{therm}} \approx 10^7$); i.e., the clusters are formed under essentially nonequilibrium conditions. Inasmuch as the coverage degree becomes as high as $\theta \simeq 1$ in time τ_p and, hence, the distances between the adatoms $l_0 \sim n^{-1/2} \approx 5$ Å $\geq a$ [$n \approx 5 \times 10^{14}$ cm^{-2} and lattice parameter $a \approx 4$ Å (NaCl)], the Au atoms can be considered to be immobile. As the coverage degree increases, some atoms become adjacent to each other and form "geometrical" 2D fractal clusters involving different numbers of atoms. Indeed, the atomic rearrangement along the cluster perimeter l_p proceeds in time $\tau \approx (l_p)^2/D$. Estimates show that clusters of size $r > 10$ Å are fractal clusters ($D = 5 \times 10^{-6}$ cm^2 s^{-1} [10]) because the corresponding $\tau > \tau_p$. As soon as the atomic concentration reaches a certain critical value θ_c (correlation threshold), the cluster size becomes infinitely large. For the 2D systems, to which the surface clusters can likely be assigned, $\theta_c \approx 0.5$ [15]. The time it takes to reach the percolation threshold can be estimated as $\tau_x \approx \theta_c \tau_p/\theta \approx 6 \times 10^{-7}$ s ($\theta \approx 0.77$). At such θ values, the 2D fractal clusters involving $n_a \geq 2$ atoms are formed in the system. The isolated atoms are virtually absent under these conditions [15]. The deposited substance is not redistributed among the clusters, because the clusters with $n_a \geq 2$ are immobile [14] [$D_n/D_1 \sim \exp(-(n-1)E_d/T) \ll 1$, where D_n is the diffusion coefficient of the n-atomic cluster, $E_d \sim 0.22$ eV is the activation energy for diffusion [10], and $T = 300$ K]. The fractal clusters can decompose through the development of unstable concentration modes with wave vectors k in the deposited substance [16]. Since the initial system is inhomogeneous (there is a scatter in the sizes of fractal clusters), the spectrum of possible k values of the unstable modes may be bounded by the maximum ($L_{\max}$) and the minimum ($L_{\min}$) sizes of fractal clusters. In this situation, the degree of supersaturation $\eta = \theta/\theta_c$ is $\eta \geq 1$ [16]. The unstable modes with $k_{\min} = 2\pi/L_{\max}$ can only be observed for those k for which the time $\tau_{k_{\min}} \leq \tau_p$ and $k_{\min} \approx (\tau_p D)^{-1/2} \approx 6 \times 10^6$ cm^{-1}. These $k_{\min}$ values correspond to the length scale $L_{\max} \approx 1800$ Å. This value is precisely that which corresponds to the maximum separation between the visible 3D clusters in the TEM images and, hence, to the maximum size of the 2D fractal cluster. The time of development of the unstable modes with $k_{\max} = 2\pi/L_{\min}$ can be estimated if one assumes that the characteristic size of the smallest cluster (dimer) is $L_{\min} \approx 10$ Å:

$$\tau_{k_{\max}} \approx (Dk_{\min}^2)^{-1} \approx 10^{10} \text{ s} \ll \tau_p.$$

Consequently, the unstable modes in our system are developed over a wide range of wave vectors $k_{\min} < k < k_{\max}$, resulting in the random distribution of visible 3D clusters (Fig. 1b).

The ratio of the amounts of substance in the visible and invisible 3D clusters can be estimated from

$$W(y) = \left(\int_y^{n_a} F(n)dn\right) \Big/ \int_{n_a}^{\infty} F(n)dn. \quad (1)$$

Here,

$$F(n) = n^{-\beta}\exp(-\epsilon(N)n^z), \quad (2)$$

where $\epsilon(N) = N[\theta(N) - \theta_c]$, β, and z are the indices, is the distribution function for the number of atoms in the fractal clusters [17]. In Eq. (1), y is the number of atoms in the smallest cluster and n_a is the number of atoms in the smallest visible cluster. According to the experimental data, the visible clusters $R \approx 15$ Å [$n_a \approx (R/a)^3$] each contain $n_a \approx 150$ atoms, while their fraction, in the aggregate, comprises ~20% of the total amount of deposited substance. Hence, $W = 4$ and the minimum number of atoms in the cluster is $y \approx 3$, in accordance with the experimental data.

The mechanism suggested for the condensation of metallic clusters allows one to explain the formation of Au clusters on the NaCl surface at $N = 50$ and the possible ordering in the cluster system. For $N = 50$, $\tau_f = 4 \times 10^{-2}$ s. The coverage degree per pulse is equal to $\theta_{a/50} \approx 0.016 \ll \theta_c$ and, hence, the percolation threshold is not achieved; i.e., the substance is not clusterized completely, so that the individual mobile gold atoms are present on the surface. As a result, the substance is redistributed between the clusters, which, hence, grow during the time periods $\tau_f = 4 \times 10^{-2}$ s $\gg \tau_a$ ($f = 25$ Hz) between two successive pulses. Indeed, the diffusion length of $l_f \approx \sqrt{D\tau_f} \approx 3.5 \times 10^{-4}$ cm covered by the Au adatom in this time is comparable with the mean distance $\langle d \rangle \approx N_{\text{cl}}^{-1/2} \approx 10^{-5}$ cm between the clusters ($N_{\text{cl}} \approx 10^{10}$ cm^{-2} is the cluster number density). On further deposition, the $\langle d \rangle$ value decreases and, hence, $\langle d \rangle \ll l_f$. Such a picture will persist until the domains of diffusional atomic capture by two neighboring islands overlap (diffusional cluster interaction). This process can be juxtaposed with the percolation transition along the diffusion zones (infinite cluster of white balls). The transition occurs if the degree $\theta(N)$ of surface coverage by the islands (with allowance made for the sizes L_{diff} of their diffusion zones) reaches the two-dimensional percolation threshold $\theta_c \approx 0.5$ [15]:

$$\theta(L_{\text{diff}}/\langle R \rangle)^2 \approx \theta_c. \quad (3)$$

For $N = 50$, one has $\theta(N) \approx 0.11$ and $\langle R \rangle \approx 15$ Å, so that, according to Eq. (3), $L_{\text{diff}} \approx 33$ Å, in nice agreement with the mean distance $\langle d \rangle \approx 35$ Å found from the Fourier-processed TEM images. Therefore, the overlap of the diffusion zones gives rise to the experimentally observed ordering of the intercluster distances (Fig. 2b).

Making use of the relation $nR^\alpha = \text{const}$ (conservation of matter; $n \sim d^{-2}$ and R are the cluster number density and the cluster size, respectively, and $\alpha > 1$) and the fact that the density of condensed phase ρ in the cluster is invariant, $\rho = nR^{-\gamma} = \text{const}$ ($\gamma > 1$), one can readily deduce the distribution function for the intercluster distances after $N \gg 1$ pulses:

$$f_N(d) = A(N)\tilde{d}_{nn}^{\mu} \exp[-\epsilon(N)\tilde{d}_{nn}^{\nu}], \quad (4)$$

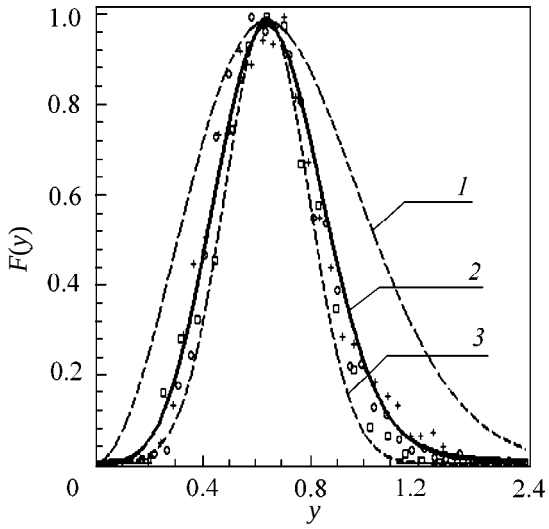

Fig. 4. Normalized distribution over the distances between the nearest neighboring Au clusters: (*1*) random distribution; (*2*) calculated by Eq. (4) for (crosses) 30, (squares) 50, and (rhombi) 100 pulses; and (*3*) Gaussian distribution.

where $A(N)$ is the normalization factor and $\mu > 1$ and $\nu > 1$ are indices. To compare this result with the experimentally observed cluster distributions over distances after 30, 50, and 100 pulses, it is convenient to substitute $y = \epsilon(N)^{1/\nu}\tilde{d}_{nn}$ in Eq. (4) and recast the distribution function as

$$F(y) = y^{\mu} \exp(-y^{\nu}). \quad (5)$$

The normalized distribution function $F(y)$ is independent of the number N of pulses and, in this sense, is a universal function of variable y.

The $F(y)$ functions with $\mu = 3.8$ and $\nu = 2.6$ are depicted in Fig. 4 for $N = 30$, 50 and 100. One can see that, over the whole range of y values, the experimental points satisfactorily fall on the curve described by distribution (5), thereby confirming the conclusion that the expression for the distribution over intercluster distances is universal. In the same figure, the random (curve *1*) and Gaussian (curve *3*) distributions are also shown for comparison. The fact that the $F(y)$ function does not depend on the number of pulses gives evidence for the self-similarity of the spatial ordering of gold clusters on the NaCl (100) surface.

We are grateful to S.É. Gulyaev and N.A. Filatova for assistance in processing the experimental results and to A.A. Timofeev for assistance in TEM measurements.

REFERENCES

1. M. Hildebrand *et al.*, Phys. Rev. Lett. **83**, 1475 (1999).
2. A. I. Olemskoĭ and N. V. Koplyk, Usp. Fiz. Nauk **165**, 10 (1995).
3. I. M. Lifshits and V. V. Slezov, Zh. Éksp. Teor. Fiz. **35**, 331 (1959) [Sov. Phys. JETP **8** (1959)].

4. G. R. Carlow and M. Zinke-Allemang, Phys. Rev. Lett. **78**, 4601 (1997).
5. G. R. Carlow, R. J. Barel, and M. Zinke-Allemang, Phys. Rev. B **56**, 12519 (1997).
6. M. Zinke-Allemang, Thin Solid Films **346**, 1 (1999).
7. J. C. S. Kools, in *Pulsed Laser Deposition Thin Films*, Ed. by D. B. Chirsley and G. K. Hubler (Wiley, New York, 1994).
8. A. Zenkevitch, J. Chevallier, and I. Khabelashvili, Thin Solid Films **311**, 119 (1997).
9. E. M. Lifshitz and L. P. Pitaevskiĭ, *Physical Kinetics* (Nauka, Moscow, 1979; Pergamon, Oxford, 1981).
10. J. A. Venables and G. D. T. Spiller, in *Surface Mobilities on Solid Materials: Fundamental Concepts and Applications*, Ed. by Vu. T. Binh, NATO ASI Ser. **86** (1981).
11. V. P. Skripov and A. V. Skripov, Usp. Fiz. Nauk **128**, 193 (1979) [Sov. Phys. Usp. **22**, 389 (1979)].
12. K. Binder, in *Materials Science and Technology: A Comprehensive Treatment*, Vol. 5: *Phase Transformations in Materials*, Ed. by R. W. Cahn, P. Haasen, and E. J. Kramer (VCH, New York, 1991), p. 71.
13. Yu. A. Bykovskiĭ, S. M. Sil'nov, E. A. Sotnichenko, and V. A. Shestakov, Zh. Éksp. Teor. Fiz. **93**, 500 (1987) [Sov. Phys. JETP **66**, 285 (1987)].
14. B. Lewis and M. R. Jordan, Thin Solid Films **6**, 1 (1970).
15. M. B. Isichenko, Rev. Mod. Phys. **64**, 961 (1992).
16. V. D. Borman, Yu. Yu. Lebedinskiĭ, and V. I. Troyan, Zh. Éksp. Teor. Fiz. **114** (7), 239 (1998) [JETP **87**, 133 (1998)].
17. A. A. Abrikosov, Pis'ma Zh. Éksp. Teor. Fiz. **29**, 1 (1979) [JETP Lett. **29**, 65 (1979)].

Translated by V. Sakun

JETP Letters, Vol. 72, No. 3, 2000, pp. 153–156. Translated from Pis'ma v Zhurnal Éksperimental'noĭ i Teoreticheskoĭ Fiziki, Vol. 72, No. 3, 2000, pp. 223–228.

Reflectionless Potentials for the Acoustic Spectral Problem

V. S. Novikov

Landau Institute for Theoretical Physics, Russian Academy of Sciences, Chernogolovka, Moscow region, 142432 Russia
e-mail: nvs@itp.ac.ru

Received July 5, 2000

The classical acoustic spectral problem is considered, and the class of reflectionless potentials for this problem is constructed. © *2000 MAIK "Nauka/Interperiodica".*

PACS numbers: 41.20.Jb; 42.25.Bs

This paper is devoted to studying the classical acoustic spectral problem on the line

$$\psi_{xx} = \lambda\varepsilon(x)\psi. \tag{1}$$

This equation has numerous physical applications, because it describes the propagation of waves in inhomogeneous media. For example, it corresponds to the problem of the propagation of electromagnetic waves in an inhomogeneous isotropic medium with the permittivity $\varepsilon(x)$:

$$\psi = E_z(x), \quad E_x = E_y = 0, \quad \lambda = -\omega^2/c^2.$$

Equation (1) was considered in many publications for different types of the function $\varepsilon(x)$ (see, e.g., [1, 2]). The purpose of this paper is to construct the class of potentials $\varepsilon(x)$ that possess the following important property: the quasiclassical solutions to Eq. (1), which have the form

$$\psi(x, p) = \exp(ip f(x) + g(x))\prod_{j=1}^{n}(ip - \xi_j(x)), \qquad \lambda = -p^2, \tag{2}$$

are exact. We will call such potentials the Bargman potentials (the *B*-potentials) [3]. These potentials may have singularities of the type

$$\varepsilon(x) \sim 1/(x - x_j)^{2\alpha} \tag{3}$$

at a finite number of points x_j, where $j = 1, \ldots, n$, with the exponent determined by the formula

$$\alpha = 2l/(2l + 1), \quad l \in \mathcal{N}. \tag{4}$$

The simplest example of the *B*-potential is $\varepsilon(x) = c/(x - x_0)^4$, where c = const and x_0 = const [1]. This occurs when the polynomial in quasiclassical Eq. (2) is equal to unity. From this class of potentials for problem (1), one can select a subclass of reflectionless potentials satisfying the condition

$$\varepsilon(x) \longrightarrow 1, \quad |x| \longrightarrow \infty. \tag{5}$$

In this case, one can consider the scattering problem

$$\psi(x, \lambda) \sim e^{-ipx} + R(p)e^{ipx}, \quad x \longrightarrow \infty, \tag{6}$$

$$\psi(x, \lambda) \sim T(p)e^{-ipx}, \quad x \longrightarrow -\infty. \tag{7}$$

These direct and inverse scattering problems can be completely analyzed, because they can be reduced to the classical scattering problem for the Schrödinger equation with a potential rapidly decreasing at infinity [4, 5] but having a finite number of singularities of the type $l(l + 1)/(y - y_j)^2$ [6]. We will consider only the Bargman and reflectionless potentials, which, by definition, correspond to $R(p) \equiv 0$.

To construct the class of *B*-potentials, we use the dressing method [7]. This procedure also provides the possibility of constructing the exact solution to Eq. (1).

Reflectionless potentials in the acoustic spectral problem. In this section, we describe the class of *B*-potentials for problem (1) and construct the reflectionless potentials. For this purpose, it is convenient to represent Eq. (1) in the form

$$\psi_{xx} = \frac{\lambda}{u^2(x)}\psi. \tag{8}$$

Conditions (5) and (3) imply that

$$u(x) \longrightarrow 1, \quad |x| \longrightarrow \infty, \quad u(x) \sim (x - x_j)^{\alpha}.$$

It is convenient to recast Eq. (8) in the form

$$\psi_{yy} = \mathcal{U}\psi_y + \lambda\psi \tag{9}$$

with the substitution [5]

$$u(x) = v_y(y), \quad x = v(y), \tag{10}$$

where

$$\mathcal{U} = v_{yy}/v_y$$

By virtue of Eqs. (5) and (3), one has

$$v_y(y) \longrightarrow 1, \quad \mathcal{U} \longrightarrow 0, \quad |y| \longrightarrow \infty, \tag{11}$$

$$v_y \sim (y-y_j)^{\alpha/(1-\alpha)}, \quad \mathcal{U} \sim \frac{\alpha}{(1-\alpha)}\frac{1}{y-y_j}, \tag{12}$$

where y_j is the solution to the equation $x_j = v(y_j)$.

Let $\varepsilon(x)$ be the *B*-potential for problem (1). This means that Eq. (8) allows the existence of solutions in the form of Eq. (2). Hence, Eq. (9) also has solutions of the type

$$\psi(y, p) = \exp(ip f(y) + g(y))P(p, y),$$
$$P(p, y) = \prod_{j=1}^{n}(ip - \xi_j(y)). \tag{13}$$

After describing the class of *B*-potentials for problem (9), we will use transformation (10) to describe the *B*-potentials for problem (1).

Substituting Eq. (13) in Eq. (9), one obtains

$$(ip f'' + g'')P + (ip f' + g')^2 P + 2(ip f' + g')P' + P'' = \mathcal{U}(ip f' + g')P + \mathcal{U}P' - p^2 P. \tag{14}$$

This equation should be satisfied for any value of p, and, hence, it represents a system of $n + 2$ equations for the functions f, g, ξ_j, and $\mathcal{U}$. The functions f and g can easily be eliminated from Eq. (14). Indeed, at $(ip)^{n+2}$ one has

$$f'^2 = 1 \longrightarrow f = \pm y.$$

We set $f = y$; then, from Eq. (14), it immediately follows that

$$\mathcal{U} = 2g'$$

[the coefficient of $(ip)^{n+1}$]. Finally, Eq. (14) takes the form

$$P'' + 2ipP' = FP,$$
$$F = \frac{1}{4}\mathcal{U}^2 - \frac{1}{2}\mathcal{U}'. \tag{15}$$

From Eq. (15), we obtain a closed system of equations for the functions $\xi_j(y)$:

$$\xi_j'' = 2\xi_j\xi_j' + \sum_{k\neq j}\frac{\xi_j'\xi_k'}{\xi_j - \xi_k}, \quad j = 1, \ldots, n. \tag{16}$$

Similarly, the case $f = -y$ yields

$$P'' - 2ipP' = FP,$$

$$\xi_j'' = -2\xi_j\xi_j' + \sum_{k\neq j}\frac{\xi_j'\xi_k'}{\xi_j - \xi_k}, \quad j = 1, \ldots, n,$$

which, evidently, corresponds to the substitutions $\xi_j \longrightarrow -\xi$ in Eq. (15) and $\psi \longrightarrow \bar{\psi}$ in Eqs. (9) and (13).

Thus, to determine all *B*-potentials for problems (9) and (1), it is sufficient to solve the system of Eqs. (15). Below, we describe the corresponding procedure.

First, we determine the possible degrees of the singularities $\varepsilon(x)$ for the class of *B*-potentials. Let $\varepsilon(x)$be the *B*-potential for problem (1), and let this potential have singularities of type (3). In view of relations (12), it is necessary to determine the residue of $\mathcal{U}$ at the point y_j: $\mathcal{U} \sim c/(y - y_j)$. In the vicinity of y_j, the function $F(y)$ can be represented in the form

$$F = \left(\frac{1}{4}c^2 + \frac{1}{2}c\right)\frac{1}{(y-y_j)^2} + F_0 + F_1(y - y_j) + \ldots$$

From Eq. (15) it follows that in the vicinity of y_j the functions ξ_j can be represented as

$$\xi_j = \frac{\xi_j^{-1}}{(y-y_j)} + \xi_j^0 + \xi_j^1(y - y_j) + \ldots,$$

where some of the residues ξ_j^{-1} may be equal to zero. Then, substituting $p = 0$ in Eq. (15), expanding ξ_j in the vicinity of y_j, and taking the principal part, one gets

$$\sum_{j=1}^{n}\xi_j^{-1}\prod_{k\neq j}\xi_k^{-1} + \sum_{j=1}^{n}\xi_j^{-1}\sum_{i\neq j}\xi_i^{-1}\prod_{k\neq i}\xi_k^{-1} = \left(\frac{1}{4}c^2 + \frac{1}{2}c\right)\prod_{j=1}^{n}\xi_j^{-1}.$$

It immediately follows from this that

$$\frac{1}{4}c^2 + \frac{1}{2}c = l(l+1), \quad l \leq n,$$
$$\alpha = 2l/(2l+1), \tag{17}$$

which proves the statement. In view of Eq. (13), one obtains for the function $\psi(y, p)$

$$\psi(y, p) = e^{ipy}\sqrt{v_y}\prod_{j=1}^{n}(ip - \xi_j),$$

One can easily see that this function is bounded in the vicinity of the singularity. Hence, the function $\psi(x, p)$ is also bounded in the vicinity of the singularity.

Let us now turn to the system of Eqs. (15). The solution to this system can be obtained in an explicit form [7, 8, 3]. Namely, let

$$\phi_1 = e^{k_1(y-y_{0,1})} \pm e^{-k_1(y-y_{0,1})},$$
$$\phi_2 = e^{k_2(y-y_{0,2})} \pm e^{-k_2(y-y_{0,2})}, \ldots,$$
$$\phi_n = e^{k_n(y-y_{0,n})} \pm e^{-k_n(y-y_{0,n})},$$

where, in the general case, k_j and $y_{0,j}$ are complex constants. Then, the function

$$\mathcal{U}_n = 2D\log\frac{\langle\phi_1, \ldots, \phi_n\rangle}{\langle\phi_1, \ldots, \phi_{n-1}\rangle} \tag{18}$$

is the *B*-potential for problem (9), and the solution to Eq. (9) is given by the formula

$$\psi_n = \sqrt{v_{n,y}}(c_1 A_n e^{ipy} + c_2 A_n e^{-ipy}), \tag{19}$$

where

$$A_n = \prod_{j=1}^{n}\left(\frac{1}{2}\mathcal{U}_j - D\right), \quad D = \frac{d}{dy},$$
$$\mathcal{U}_j = 2D\log\frac{\langle\phi_1, \ldots, \phi_n\rangle}{\langle\phi_1, \ldots, \phi_{n-1}\rangle} \tag{20}$$
$$v_{n,y} = \left(\frac{\langle\phi_1, \ldots, \phi_n\rangle}{\langle\phi_1, \ldots, \phi_{n-1}\rangle}\right)^2,$$

and c_j are constants. Evidently, such a *B*-potential is parametrized by the constants k_j, phases $y_{0,j}$, and the sign in the expressions for ϕ_j. Using Eqs. (10), we obtain the class of the *B*-potentials for problem (1):

$$u_n(y) = \text{const}\left(\frac{\langle\phi_1, \ldots, \phi_n\rangle}{\langle\phi_1, \ldots, \phi_{n-1}\rangle}\right)^2,$$
$$x = \text{const}\int\left(\frac{\langle\phi_1, \ldots, \phi_n\rangle}{\langle\phi_1, \ldots, \phi_{n-1}\rangle}\right)^2 dy. \tag{21}$$

The solution to problem (1) can be obtained from Eq. (19) by the substitution (10).

Now, we consider a subclass of reflectionless potentials for the problem under study. In this case, it is necessary that condition (5) be satisfied, which occurs if one sets $\phi_n = 1$ and const $= 1/\prod_{j=1}^{n} k_j^2$ in Eq. (21). Then, from Eq. (21) it follows that no reflectionless potentials without singularities exist for problem (1). The degree of such a singularity is specified by Eq. (17). Let $l = 1$, i.e., $\alpha = 2/3$. Assume that

$$0 < k_1 < k_2 < \ldots < k_n, \tag{22}$$

$$\phi_1 = \cosh(k_1(y - y_{0,1})), \quad \phi_2 = \sinh(k_2(y - y_{0,2})),$$
$$\phi_3 = \cosh(k_3(y - y_{0,3})), \ldots, \tag{23}$$
$$\phi_n = \cosh(\sinh)(k_n(y - y_{0,n})), \quad \phi_{n+1} = 1.$$

Then, it is easy to show that Eqs. (21) and (23) with condition (22) determine all reflectionless potentials corresponding to problem (1) and having *n* singularities of the type $u(x) \sim (x - x_j)^{2/3}$. At $n = 1$, one has

$$u_1 = \tanh^2(k_1(y - y_{0,1})),$$
$$x = y - \frac{1}{k_1}\tanh(k_1(y - y_{0,1})) + x_0.$$

For the case $n = 2$,

$$u_2 = \frac{(k_2\sinh(k_1(y - y_{0,1}))\sinh(k_2(y - y_{0,2})) - k_1\cosh(k_1(y - y_{0,1}))\cosh(k_2(y - y_{0,2})))^2}{(k_1\sinh(k_1(y - y_{0,1}))\sinh(k_2(y - y_{0,2})) - k_2\cosh(k_1(y - y_{0,1}))\cosh(k_2(y - y_{0,2})))^2}.$$

Thus, we described the reflectionless potentials for problem (1) with a finite number of singularities of degree $2\alpha = 4/3$ [see Eq. (3)]. In a similar way, one can consider the case of higher order singularities $\alpha = 2l/(2l + 1)$ with $l = 2, 3, \ldots$. For example, for $l = 2$ and $n = 2$

$$u = \frac{(k_2\sinh(k_1(y - y_{0,1}))\cosh(k_2(y - y_{0,1})) - k_1\sinh(k_2(y - y_{0,1}))\cosh(k_1(y - y_{0,1})))^2}{(k_1\sinh(k_1(y - y_{0,1}))\cosh(k_2(y - y_{0,1})) - k_2\sinh(k_2(y - y_{0,1}))\cosh(k_1(y - y_{0,1})))^2}.$$

In closing, let us discuss the spectral meaning of the reflectionless and *B*-potentials constructed in this work. It can be shown that the reflectionless potentials (21)–(23) have *n* discrete eigenvalues $\lambda = k_j^2$, which are determined by the standard condition [4]

$$\int_{-\infty}^{+\infty}\psi^2(x, \lambda_j)dx < \infty.$$

The coefficient of reflection in Eq. (6) is $R(p) \equiv 0$, and the coefficient of transmission is

$$|T(p)|^2 = \left|\prod_{j=1}^{n}\frac{k_j - ip}{k_j + ip}\right|^2 = 1, \quad \text{Im}(p) = 0.$$

Figure 1 shows the function $u_2(x)$ for $k_1 = 1$, $k_2 = 2$, $y_{0,1} = 0$, and $y_{0,2} = 5$. Figure 2 presents the function $u_3(x)$ for $k_1 = 1$, $k_2 = 2$, $k_3 = 3$, $y_{0,1} = 0$, $y_{0,2} = -2$, and $y_{0,3} = 5$.

Thus, we have described in this paper the so-called *B*-potentials and the reflectionless potentials for problem (1). It is demonstrated that each of the reflection-

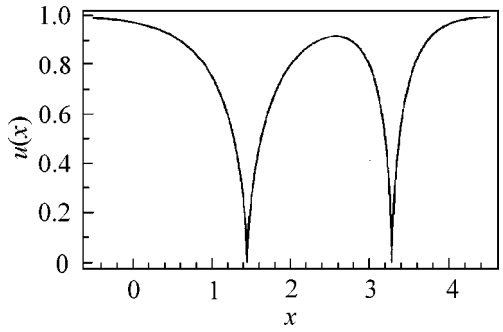

Fig. 1

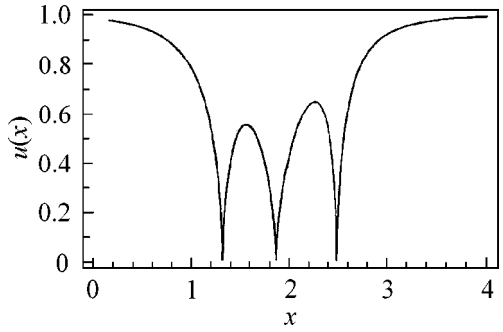

Fig. 2

less potentials has singularities of type (3). One of the possible regularization methods for these singularities consists in shifting the zeroes of the function $u(x)$ to the complex plane. Evidently, the quantity $\varepsilon(x)$ then ceases to be real and becomes complex, which corresponds to the occurrence of absorption. However, the general regularization problem is beyond the scope of this paper.

The other fact that also falls beyond the scope of this paper is the relation of problem (1) to the theory of nonlinear integrable partial differential equations. Problem (1) is a spectral problem for the Harres Dym equation [5]

$$u_t = u^3 u_{xxx} + \beta u_x, \quad \beta = \text{const}.$$

It can be shown that the *B*-potentials for problem (1) are the soliton solutions to the Harres Dym equation [9, 10] and its higher analogues.

I am grateful to my scientific supervisor Professor A.B. Shabat and also to V.G. Marikhin, P.G. Grinevich, and S.V. Bulanov for useful discussions.

REFERENCES

1. V. L. Ginzburg, *The Propagation of Electromagnetic Waves in Plasmas* (Nauka, Moscow, 1967; Pergamon, Oxford, 1970).
2. L. M. Brekhovskikh, *Waves in Layered Media* (Akad. Nauk SSSR, Moscow, 1957; Academic, New York, 1960).
3. A. B. Shabat, Din. Sploshnoĭ Sredy **5**, 130 (1970).
4. S. Novikov, S. V. Manakov, L. P. Pitaevskiĭ, and V. E. Zakharov, *Theory of Solitons: the Inverse Scattering Method* (Nauka, Moscow, 1980; Consultants Bureau, New York, 1984).
5. F. Calogero and A. Degasperis, *Spectral Transform and Solitons: Tools to Solve and Investigate Nonlinear Evolution Equations* (North-Holland, Amsterdam, 1982; Mir, Moscow, 1985).
6. V. A. Arkad'ev, A. K. Pogrebkov, and M. K. Polivanov, *Singular Solutions of KdV Equation and Inverse Scattering Method*, Note of Scientific Seminar of LOMI.
7. A. P. Veselov and A. B. Shabat, FAN **27**, 1 (1993).
8. A. B. Shabat, Inverse Probl. **8**, 303 (1992).
9. L. A. Dmitrieva, Phys. Lett. A **182**, 65 (1993).
10. L. A. Dmitrieva, J. Phys. A **26**, 6005 (1993).

Translated by E. Golyamina

JETP Letters, Vol. 72, No. 3, 2000, pp. 97–99. From Pis'ma v Zhurnal Éksperimental'noĭ i Teoreticheskoĭ Fiziki, Vol. 72, No. 3, 2000, pp. 145–149.

Possible Signature of Low-Scale Gravity in Ultrahigh-Energy Cosmic Rays[1]

R. V. Konoplich* and S. G. Rubin, *****

**New York University, NY 10003, USA*

e-mail: nvgrk4@netzero.net

*** Moscow Institute of Engineering Physics, Kashirskoe sh. 31, Moscow, 115409 Russia*

**** Cosmion Center for Cosmoparticle Physics, Moscow, 111123 Russia*

e-mail: serg.rubin@mtu-net.ru

Received June 6, 2000; in final form, June 29, 2000

We show that the existence of low-scale gravity at the TeV scale could lead to a direct production of photons with energy above 10^{22} eV due to annihilation of ultrahigh-energy neutrinos on relic massive neutrinos of the galactic halo. Air showers initialized in the terrestrial atmosphere by these ultraenergetic photons could be collected in near future by the new generation of cosmic ray experiments. © *2000 MAIK "Nauka/Interperiodica".*

PACS numbers: 04.80.Cc; 98.70.Sa

Recently it was proposed [1] that space is $4 + n$ dimensional, with the Standard Model particles living on a brane. While the weakly, electromagnetically, and strongly interacting particles are confined to the brane in 4 dimensions, gravity can also propagate in the extra n dimensions. This approach allows one to avoid the gauge hierarchy problem by introducing a single fundamental mass scale (string scale) M_s of the order of TeV. The usual Planck scale $M_{Pl} = 1/\sqrt{G_N} \simeq 1.22 \times 10^{19}$ GeV is related to the new mass scale M_s by Gauss's law:

$$M_{Pl}^2 \sim R^n M_s^{n+2} \tag{1}$$

where G_N is the Newton constant and R is the size of extra dimensions. It follows from Eq. (1) that

$$R \sim 2 \times 10^{-17} \left(\frac{\text{TeV}}{M_s}\right)\left(\frac{M_{Pl}}{M_s}\right)^{2/n} \text{ cm} \tag{2}$$

gives, at $n = 1$, too large a value, which is clearly excluded by present gravitation experiments. On the other hand $n \geq 2$ gives the value $R \lesssim 0.25$ cm, which is below the present experimental limit ~1 cm but can be tested for the case $n = 2$ in gravitational experiments in the near future.

It can be shown that the graviton, including its excitations in the extra dimensions, the so-called Kaluza–Klein (KK) graviton emission, interacts with the Standard Model particles on the brane with an effective amplitude $\sim M_s^{-1}$ instead of M_{Pl}^{-1}. Indeed, the graviton coupling to the Standard Model particle $\sim M_{Pl}^{-1}$, and the rate [2] of the graviton interaction $r \sim (M_{Pl}^{-1})^2 N$, where N is a multiplicity of KK states. Since this factor is $\sim(\sqrt{S}R)^n$, where $\sqrt{S}$ is the C.M. energy, then substituting R from Eq. (2) we get $r \sim M_s^{-2}$. Thus, the graviton interaction becomes comparable in strength with weak interaction at TeV scale.

This leads to the varieties of new signatures in particle physics, astrophysics and cosmology (see, e.g., [2–6]) which have already been tested in experiments or can be tested in the near future.

In this article we consider the possible signature of low-scale gravity in ultrahigh-energy cosmic rays.

The detection [7, 8] of cosmic rays with energy above the Greisen–Zatsepin–Kuzmin (GZK) cutoff of $\sim 5 \times 10^{19}$ eV presents a serious problem for interpretation. The origin of the GZK cutoff [9] is due to resonant photoproduction of pions by protons on cosmic microwave background radiation, which leads to a significant degradation of proton energy (about 20% for 6 Mpc) during its propagation in the Universe. Of course, proton energy does not change by many orders of magnitude if high energy protons come from the distances < 50–100 Mpc. However, no nearby sources like active galactic nuclei have been found up to now in the arrival direction.

It is also difficult to relate the observed ultrahigh-energy events with the other particles. For example, in the case of ultrahigh-energy photons due to interaction with cosmic background radiation ($\gamma + \gamma^* \longrightarrow e^+ + e^-$), the photon free mean path should be significantly less than 100 Mpc. A scenario based on direct cosmic neutrinos able to reach the Earth from cosmological dis-

[1] This article was submitted by the authors in English.

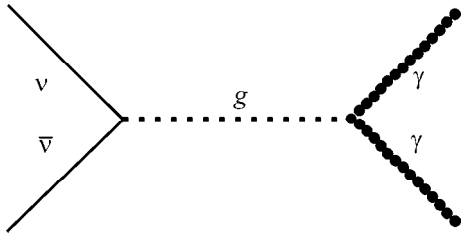

Fig. 1. Neutrino annihilation into two photons.

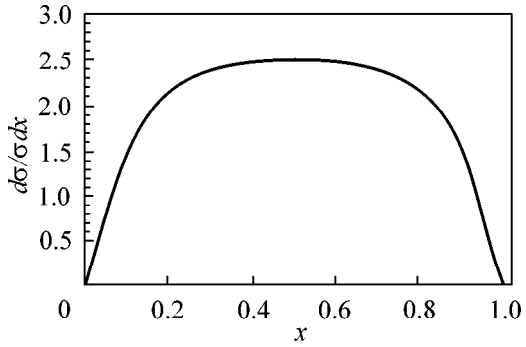

Fig. 2. Energy distribution of photons ($x = \omega/E$).

tances can not reproduce the observed signatures of ultrahigh-energy air showers occurring high in the atmosphere.

Different possibilities were considered (see, e.g., [10] and references therein) in order to solve this puzzle. In particular, it was proposed [11–13] that ultrahigh-energy neutrinos reaching the Earth from cosmological distances interact with a halo of relic light neutrinos in the Galaxy, producing $W^{\pm}$ boson exchange secondaries inside the galactic halo due to Z. Photons from π^0 decays and nucleons can easily propagate to the Earth and be the source of the observed ultrahigh-energy air showers. Crucial elements of models [11–13] are the existence of neutrino mass in the range 0.1–10 eV and significant clustering of relic neutrinos in the halo up to $10^5 n_\nu$, where n_ν is the cosmological neutrino number density ($n_\nu \sim 100$ cm^{-3}). Also, the existence of ultrahigh-energy ($>10^{21}$–10^{23} eV) neutrino flux is necessary in order to produce multiple secondaries with energies above the GZK cutoff.

However, if the graviton interaction comparable in strength with the weak interaction at the TeV scale exists, then photons can be produced directly in a reaction

$$\nu + \bar{\nu} \longrightarrow g \longrightarrow \gamma + \gamma \qquad (3)$$

due to virtual graviton exchange (Fig. 1). In the Standard Model, process (3) occurs via loop diagram and therefore is severely suppressed.

At high energies, the cross section for process (3) can be obtained immediately from that for the process $e^+e^- \longrightarrow \gamma\gamma$ including graviton exchange (see, e.g., [3]) by substituting $e = 0$. Then

$$\frac{d\sigma}{dz} = \frac{\pi}{16}\frac{S^3}{M_s^8}F^2(1-z^4) \qquad (4)$$

where $\sqrt{S}$ is the C.M. energy and $z = |\cos\theta|$ is the polar angle of the outgoing photon. The factor F depends on the number of extra dimensions:

$$F = \begin{cases} \log(M_s^2/S), & n = 2 \\ 2/(n-2), & n > 2, \end{cases}$$

at $\sqrt{S} \ll M_s$. In Eq. (4), it is also taken into account that the primary beam of neutrinos is polarized.

Integrating Eq. (4) over the polar angle and including a symmetry factor for two γ, we get

$$\sigma = \frac{\pi}{20}\frac{S^3}{M_s^8}F^2 \approx 7\times 10^{-35}F^2\left(\frac{\sqrt{S}}{\text{TeV}}\right)^6\left(\frac{\text{TeV}}{M_s}\right)^8 \text{cm}^2. \quad (5)$$

One can see from Eq. (5) that at TeV energies the rate of reaction (3) is comparable with the rate of weak processes [11].

Assuming $M_s \sim \sqrt{S} \sim$ TeV, we find, e.g., for $n = 3$, the following probability for the interaction of ultrahigh-energy neutrinos inside the galactic halo: $P \approx \sigma n_G L_G \sim 10^{-3}$, where $L_G \sim 100$ Kpc is the size of the galactic neutrino halo and $n_G \sim 10^5 n_\nu$ is the neutrino number density in the galactic halo. This probability is significantly greater than the probability of ultrahigh-energy neutrino interaction in the terrestrial atmosphere [14].

Let us note that nearby galaxies can also be sources of additional ultrahigh-energy photons due to neutrino interaction with relic neutrinos of galactic halos [12, 13].

TeV range in C.M. corresponds to the energy of the extragalactic neutrino flux $E \approx 10^{22}$–10^{23} eV, since

$$E \approx \frac{S}{2m} \approx 5\times 10^{22}\left(\frac{\sqrt{S}}{\text{TeV}}\right)^2\left(\frac{10\text{ eV}}{m}\right)\text{eV}, \qquad (6)$$

where m is the neutrino mass.

Photon distribution in reaction (3) in laboratory system is given by

$$\frac{d\sigma}{d(\omega/E)} = 8\pi F^2\frac{m^3E^3}{M_s^8}\frac{\omega}{E} \times\left(1-\frac{\omega}{E}\right)\left[\left(1-\frac{\omega}{E}\right)^2+\left(\frac{\omega}{E}\right)^2\right] \qquad (7)$$

where $\omega \gg m$ is the photon energy. This distribution is shown in Fig. 2. It follows from Eq. (7) that photons are produced in reaction (3) mainly within the energy range $0.2E \lesssim \omega \lesssim 0.8E$, with an average energy $\approx E/2$.

Therefore, the existence of low-scale gravity at the TeV scale or above could lead to the direct production of photons with energy $\omega > 10^{22}$ eV (at these energies the mean interaction length for pair production for photons in the radio background is ≈1–10 Mpc [15]). Such photons can hardly be produced in standard weak interaction processes, because in these last ones photons appear as a result of cascade processes, significantly reducing the photon energy in comparison with the initial neutrino energy. For example, as it was shown in [11], the final energy of photons produced due to cascade processes can be 10–100 times less than the energy of the initial neutrino flux.

Of course, photons with the energy $\sim 10^{23}$ eV could be produced in cascade processes induced by neutrinos with energy $> 10^{24}$–10^{25} eV, but from the observations of cosmic rays, we know that cosmic ray fluxes decrease with energy as E^{-3}, and therefore the probability of such events is significantly suppressed.

Fluxes of ultrahigh-energy cosmic rays at the Earth are very small: $\Phi \sim 0.03$ km^{-2} sr^{-1} yr^{-1}. Until now, only about 60 events were collected with energies above the GZK cutoff. However, in the near future, improved Fly's Eye (7000 km^2 sr) [8] will allow detection of about 20 events/yr. It seems possible that such a detector could collect rare ultraenergetic photons ($\omega > 10^{22}$ eV). The detection of such events could be an indication that these ultrahigh-energy photons were produced in $\nu\bar{\nu}$ annihilation in the galactic halo due to effects of low-scale gravity at the TeV scale. Neutrino–gamma interaction in low-scale gravity also was considered in [16].

The authors thank D. Fargion for interesting discussions on ultrahigh-energy cosmic rays. One of us (RVK) is grateful to the Physics Department of New York University for warm hospitality. The work of SGR was partially performed in the framework of the Section "Cosmoparticle Physics" of the Russian State Scientific Technological Program "Astronomy. Fundamental Space Research," with the support of Cosmion-ETHZ and Epcos-AMS collaborations.

REFERENCES

1. N. Arkani-Hamed, S. Dimopoulos, and G. Dvali, Phys. Lett. B **429**, 263 (1998); I. Antoniadis, N. Arkani-Hamed, S. Dimopoulos, and G. Dvali, Phys. Lett. B **436**, 257 (1998); N. Arkani-Hamed, S. Dimopoulos, and G. Dvali, hep-ph/9807344; N. Arkani-Hamed, S. Dimopoulos, and J. March-Russel, hep-th/9809124.
2. S. Nussinov and R. Shrock, Phys. Rev. D **59**, 105002 (1999).
3. K. Cheung, Phys. Rev. D **61**, 015005 (2000); K. Cheung and Wai-Yee Keung, Phys. Rev. D **60**, 112003 (1999).
4. G. F. Giudice, R. Rattazzi, and J. D. Wells, Nucl. Phys. B **554**, 3 (1999).
5. Tao Han, J. Lykken, and Ren-Jie Zhang, Phys. Rev. D **59**, 105006 (1999).
6. G. Dvali and A. Yu. Smirnov, hep-ph/9904211 (1999); L. J. Hall and D. Smith, hep-ph/9904267 (1999); V. Barger, T. Han, C. Kao, and R.-J. Hang, hep-ph/9905474; P. Jain *et al.*, hep-ph/0001031 (2000).
7. D. J. Bird *et al.*, Astrophys. J. **441**, 144 (1995); S. Yoshida *et al.*, Astropart. Phys. **3**, 105 (1995); B. N. Afanasiev *et al.*, in *Proceedings of the 24th International Cosmic Ray Conference, Rome, 1995*, Vol. 2, p. 756; M. A. Lawrence *et al.*, J. Phys. G **17**, 773 (1991); N. Hayashida *et al.*, Phys. Rev. Lett. **77**, 1000 (1996); M. Takeda *et al.*, Phys. Rev. Lett. **81**, 1163 (1998).
8. J. W. Cronin, Rev. Mod. Phys. **71**, S165 (1999).
9. K. Greisen, Phys. Rev. Lett. **16**, 748 (1966); G. T. Zatsepin and V. A. Kuzmin, Pis'ma Zh. Éksp. Teor. Fiz. **4**, 114 (1966) [JETP Lett. **4**, 78 (1966)].
10. J. W. Elbert and P. Sommers, Astrophys. J. **441**, 151 (1995); R. J. Protheroe and P. A. Johnston, Astropart. Phys. **4**, 253 (1996); N. Mohapatra and S. Nussinov, Phys. Rev. D **57**, 1940 (1998); C. Sigl, S. Lee, D. N. Schramm, and P. Coppi, Phys. Lett. B **392**, 129 (1997); V. Berezinsky, M. Kachelriess, and A. Vilenkin, Phys. Rev. Lett. **79**, 4302 (1997); G. Burdman, F. Halzen, and R. Gandhi, Phys. Lett. B **417**, 107 (1998); G. R. Farrar and T. Piran, astro-ph/9906431 (1999); V. Berezinsky, hep-ph/0001163 (2000); A. V. Olinto, astro-ph/0002006 (2000).
11. D. Fargion, B. Mele, and A. Salis, astro-ph/9710029 (1997).
12. T. J. Weiler, Astropart. Phys. **11**, 303 (1999).
13. T. J. Weiler, hep-ph/9910316 (1999).
14. R. Gandhi *et al.*, Astropart. Phys. **5**, 81 (1996).
15. R. J. Protheroe, astro-ph/9812055 (1998).
16. D. A. Dicus, K. Kovner, and W. W. Repko, hep-ph/0003152.